Determination of melting point trends of model salts by molecular dynamics simulations

by

Erin Lindenberg

A THESIS SUBMITTED IN PARTIAL FULFILLMENT OF
THE REQUIREMENTS FOR THE DEGREE OF

DOCTOR OF PHILOSOPHY

in

The Faculty of Graduate and Postdoctoral Studies

(Chemistry)

THE UNIVERSITY OF BRITISH COLUMBIA

(Vancouver)

December 2014

Abstract

We examine the melting point trends across sets of coarse grain model salts using NPT molecular dynamics simulations. The melting point trends are established relative to a charge-centered, size-symmetric salt that is closely akin to the restricted primitive model. Two of the common features of ionic liquids, namely size asymmetry and a distributed cation charge, are systematically varied in a set of model salts. We find that redistributing the cation charge in salts with size-symmetric, monovalent, spherical ions can reduce the melting temperature by up to 50% compared to the charge-centered case. Displacing the charge from the ion center reduces the enthalpy of the liquid more than that of the solid resulting in a lower melting point. We consider two sets of size-asymmetric salts with size ratios up to 3:1 using different length scales; the melting point trends are different in each set, but within each set we find salts that achieve a melting point reduction of over 60% from the charge-centered, size-symmetric case. The lowest melting point range we find is between 450 K and 500 K. We find diversity in the solid phase structures. For all size ratios with small cation charge displacements, the salts crystallize with orientationally disordered cations. For equal-sized ions, once the cation charge is moved far enough off-center, the salts become trapped in glassy states upon cooling and we find an underlying crystal structure (space group 111) that features orientationally ordered ion pairs. The salts with large size ratios and large cation charge displacements achieve the lowest melting points and also show premelting transi-

tions at lower temperatures (two as low as 300 K). We find two types of premelting behaviour; some salts exhibit a fast ion conductor phase, where the smaller anions move through a face-centered cubic (fcc) cation lattice, whereas other salts have a plastic crystal phase composed of ion pairs rotating on an fcc lattice.

Preface

The research presented in this thesis are or will be co-authored publications of E. K. Lindenberg and Dr. G. N. Patey. Parts of Chapters 1, 2, 3, and 6 have been published as a journal article [E. K. Lindenberg and G. N. Patey, "How distributed charge reduces the melting points of model ionic salts," J. Chem. Phys. **140**, 104504 (2014)]. Parts of Chapters 1, 2, 4, and 6 are in preparation for submission as a journal article. The research and data analysis was performed by E. K. Lindenberg with guidance and suggestions from Dr. G. N. Patey. The manuscripts were written by E. K. Lindenberg with revisions and additions by Dr. G. N. Patey.

The work in this thesis builds on earlier projects done by Dr. H. V. Spohr as a doctoral student and post-doctoral researcher in Dr. G. N. Patey's group. Dr. H. V. Spohr's doctoral work focused on the liquid phase dynamics of similar model salts. Part of Dr. H. V. Spohr's post-doctoral research was a preliminary study of the melting point trends of a set of charge- and size-symmetric salts.

The model salts considered in thesis include and expand upon the ion model geometries from Dr. H. V. Spohr's doctoral work. Some of the ion model parameters were set by Dr. H. V. Spohr and Dr. G. N. Patey. The methods used to determine melting point trends in this thesis differ from those used in Dr. H. V. Spohr's preliminary melting point work. The final research design, data collection and analysis, and manuscript composition was done by E. K. Lindenberg with guidance and suggestions from Dr. G. N. Patey, and was carried out independently from the initial work of Dr. H. V. Spohr.

Table of Contents

Appendices

List of Tables

List of Figures

List of Symbols

$\boldsymbol{\mu}_i(t)$	Unit Vector From CM to CC on 2L Cation i at Time t
$\boldsymbol{\omega}_i^l$	Angular Velocity of Particle i in the Local Particle Frame
$\boldsymbol{\tau}_i^l$	Torque on Particle i in the Local Particle Frame
$\boldsymbol{A}$	Rotation Matrix to Transform Coordinates Between Frames of Reference
$\boldsymbol{f}_i$	Force on Particle i
$\boldsymbol{g}$	Metric Tensor Defining the Simulation Cell
$\boldsymbol{h}$	Matrix that Defines the Conventional Simulation Cell
$\boldsymbol{Q}$	Quaternion Representation of a Particle's Orientation
$\boldsymbol{r}_i^F$	Fractional Coordinates of Particle i's Center Within the Simulation Cell
$\boldsymbol{r}_i$	Cartesian Coordinates of the Center (LJ Site) of Particle i
$\boldsymbol{r}_{i\alpha}$	Cartesian Coordinates of Interaction Site α on Particle i
$\boldsymbol{s}_\alpha$	Vector From the Particle Center to Interaction Site α in the Particle Coordinate Frame
ϵ	Permittivity of the Medium
κ	Ewald Summation Parameter
ρ^*	Reduced Number Density, $N\sigma^3/V$
σ	The LJ Length Parameter (Particle Diameter)
σ_+	The LJ Diameter of the Cation
σ_-	The LJ Diameter of the Anion
$\sigma_\pm$	The LJ Distance From the Cation Center to the Anion Center
θ	Angle Between Vectors Drawn From the Ion Center to the Two Off-Center Sites in a 3s Ion

ε_{ij}	Lennard-Jones Energy Parameter
ξ	Friction Coefficient that Adjusts Particle Motions to Maintain the Temperature
D	Diffusion Coefficient
d	The Distance Between the Ion Center (LJ Site) and Off-center Charge Site in Units of 0.01 nm
L_c	Normalized Charge Arm
m	Mass
N	Number of Particles
P	Pressure
Q	Parameter Determining the Thermostat Responsivity (Scalar)
q_{ion}	Total Ion Charge
R_{ion}	Ion Radius
R_{cut}	Cutoff Distance for Computing Short-range Interactions
$r_{i\alpha j\beta}$	The Distance Between Site α on Ion i and Site β on Ion j
r_{ij}	The Distance Between LJ Sites on Ions i and j
T_+	Highest Temperature of the Superheated Solid Before Melting
T_-	Lowest Temperature of the Supercooled Liquid Before Freezing
T_g	Glass Transition Temperature Defined as the Temperature Where the Diffusion Coefficient Falls Below 10^{-11} m^2/s on the Cooling Curve
T_l	Lowest Temperature that Evolved into a Liquid in the Two-phase Simulations
T_m	Melting Temperature Determined from the Hysteresis Method
T_s	Highest Temperature that Evolved into a Solid in the Two-phase Simulations
u_{ij}	Pair Potential Between Particles i and j
V	Volume of the Simulation Cell

W	Parameter Determining the Barostat Responsivity (Scalar)
1C	A Spherical Ion with One Interaction Site at its Center
2L	An Ion with Two Interaction Sites in a Linear Arrangement
2L100	A Two-site Ion with all of the Unit Charge on the Off-center Interaction Site
2L33	A Two-site Ion with 1/3 of the Unit Charge on the Off-center Interaction Site
2L50	A Two-site Ion with 1/2 of the Unit Charge on the Off-center Interaction Site
2L67	A Two-site Ion with 2/3 of the Unit Charge on the Off-center Interaction Site
3s	Represents a Set of Ions, Each with Three Interaction Sites
AC	Anion Off-center Charge Site
AM	Anion Center (LJ Site)
CC	Cation Off-center Charge Site
CM	Cation Center (LJ Site)
CsCl	Two Interpenetrating Simple Cubic Lattices of Cations and Anions
Ion Center	Location of the Lennard-Jones Interaction Site
msd	Mean Squared Displacement
MSDS	Material Safety Data Sheet
NaCl	Two Interpenetrating Face Centered Cubic Lattices of Cations and Anions
OD-CsCl	Orientationally Disordered Cesium Chloride Crystal Structure
RPM	Restricted Primitive Model

for my family

Chapter 1

Introduction *

> *"Because ionic liquids have complex molecular structure, the correlation of the properties displayed by these materials to their structure may be very complicated; there is then a need to rationalize the behaviour of this class of liquids in a general picture, which is able to keep track of their essential characteristics."*
>
> – Marco Malvaldi and Cinzia Chiappe
> *J. Phys.: Condens. Matter* **20** 035108 (2008)

1.1 Ionic Liquids

Ionic liquids (ILs) are salts usually composed of molecular ions that exist in the liquid phase under ambient, or near ambient, conditions. By convention, ILs are defined as salts with melting points or glass transition temperatures below 373 K,[1] which differentiates them from conventional molten salts that melt at much higher temperatures.[2] Sodium chloride and cesium chloride, for example, have normal melting points of 1074 K and 918 K, respectively.

Ammonium-based ionic liquids have been known for over a century, with 2-aminoethanol nitrate reported in 1888 by S. Gabriel and J. Weiner, and ethylamine nitrate reported in 1914 by P. Walden.[3,4] It was Walden who provided the initial distinction of ILs as water-free salts which melt at relatively low temperatures, up

*Parts of this chapter have been published. E. K. Lindenberg and G. N. Patey, "How distributed charge reduces the melting points of model ionic salts," *J. Chem. Phys.* **140**, 104504 (2014).

to about 373 K, which has become the accepted definition.[3,4]

It is estimated that there are up to 10^6 possible binary ionic liquids, which increases to about 10^{18} if ternary systems are included.[3,5] Over the last 50 years, research on ionic liquids has primarily focused on cation variations; tetraalkylammonium cations and organic heterocyclic cations such as imidazolium, pyridinium, and pyrrolidinium structures are common. Anions typically tend toward the inorganic side, such as halides, nitrate, tetrafluoroborate, and hexafluorophosphate, but are becoming more exotic. Some of the common IL ions are shown in Fig. 1.1.

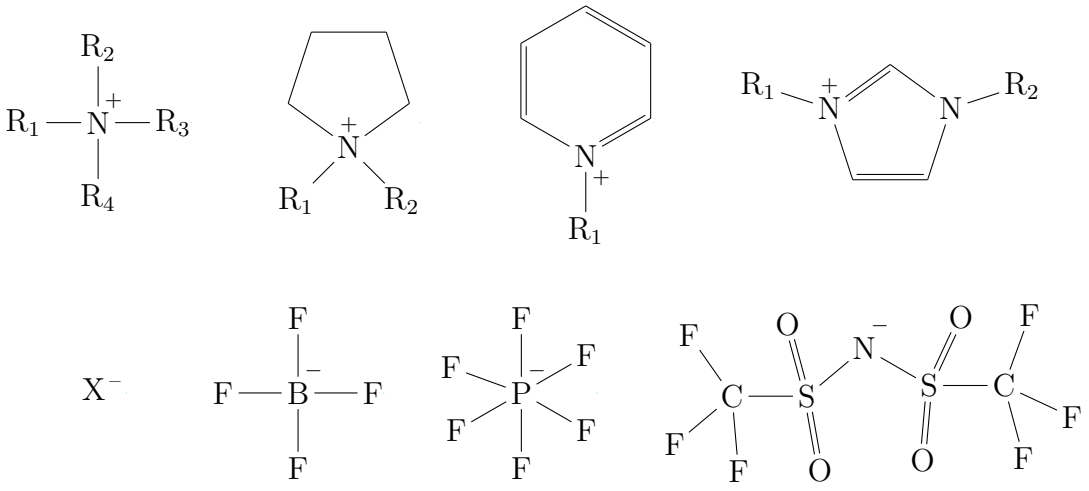

Figure 1.1: Common Ions found in Ionic Liquids. Typical cation structures are shown across the top row and include the tetraalkylammonium cation, dialkylpyrrolidinium cation, alkylpyridinium cation, and alkylimidazolium cation, where $R_{1\text{-}4}$ indicate alkyl substituent groups. Typical anions are shown across the bottom row and include halides, tetrafluoroborate, hexafluorophosphate, and bis(trifluoromethanesulfonyl)imide

Aside from being salts with relatively low melting points, there is nothing that restricts ILs to particular structural features or functional groups. ILs have earned the moniker "designer solvents" because the physical properties can be tailored by changing the combination of ions, or by changing the connectivities or identities

of substituent groups within those ions. Similar tactics are used to create new ILs by introducing (or exaggerating) molecular asymmetry, creating size mismatches between ions, delocalizing charges, elaborating side chains, and/or making fluorous substitutions.[6]

Like traditional inorganic salts, ionic liquids are dominated by electrostatic interactions, but because their melting points are significantly lower, they require less thermal energy (and the specialized equipment designed to withstand high temperatures) to reach the liquid phase. With an accessible liquid phase and tunable properties, ionic liquids are being investigated for use in a wide variety of applications.[7–9] Before giving a few examples of the potential applications of ILs, we discuss some of the aspects of finding, and optimizing, a task-specific IL.

For a specific task, it is possible to prioritize desirable physical properties and performance attributes of the material. Task-specific ILs can integrate function, design, and safety elements at the level of ion structure, which encourages a holistic approach to material design. However, the identification of promising IL candidates with particular physical properties is not trivial.[10–12] Furthermore, determining which IL is best (as opposed to well-suited) for a particular application is even more difficult.[13]

Early in the screening process, IL candidates are eliminated for undesirable properties such as high toxicities and corrosivities.[14] Thermal stability (decomposition) and reactivity (potential degradation) are considered for the operating conditions and expected life cycle of the application. The thermal conductivities and heat capacities are also important.[14] Tunable properties such as the densities, viscosities, hydrophobicities,[15,16] electrical conductivities, liquid phase range, hygroscopic tendencies, surface and bulk structures, and/or solubilities are tailored into the desired

range for the particular applications. Wide electrochemical windows—the voltage range limited by oxidation and reduction of the ions—are also a common feature and desirable attribute of ILs for electrochemical applications.

The range of IL properties far exceeds those of conventional organic solvents.[17] ILs have been called "green" solvents because of their low volatilities and the environmentally attractive possibility of being able to recycle/reuse ILs with relative ease, in comparison to more traditional volatile organic solvents. The designation of ILs as environmentally friendly solvents does not address issues of potential toxicity or biodegradability.[3] For solvent use, the bounds on the liquid range, viscosity, solubilities, and non-reactivity are the key tunable parameters. ILs provide a reaction environment with more electrostatic character, which influences the solubilities of organic and inorganic materials. IL solvents open up synthetic and kinetic pathways that may be more efficient (and diverse) than traditional organic solvent chemistry. Reactivity in terms of reaction rates, yield, product selectivity, and even enantioselectivity are all subject to change with different solvents.[3,18,19] Chiral ILs have been used successfully in asymmetric synthesis.[20]

ILs are also promising as electrolytes.[14] The desirable properties of electrolytes include a wide electrochemical window, high conductivity, wide operating temperature range, and for safety reasons, low flammability and low volatility.[14,21] As the scale of battery-powered devices increases into vehicle-sized objects, the demand for safer batteries also increases.[21] Large batteries based on strong electrolytes, such as $H_2SO_{4\,(aq)}$ and $KOH_{(aq)}$, would present safety hazards due to the amounts (and concentrations) involved. The safety measures required for containment are due to extreme pH and reactivity, not necessarily the high conductivity. ILs are an enticing alternative. The tunable nature of IL properties can be exploited to

dampen reactivity but maintain sufficient conductivity for use as an electrolyte.

ILs have been investigated for a variety of other novel applications. We note a small sample of them here. High thermal stabilities, densities, and heat capacities also make ILs promising candidates as heat (energy) transfer and storage fluids.[14,22–26] Long alkyl chains on ILs increase the likelihood of tail aggregation, making ILs attractive as surfactants.[27,28] Tunable viscosities and high thermal stabilities make ILs attractive options for lubricants.[29–31] ILs with low vapour pressure that are capable of absorbing large amounts of CO_2 are being investigated for carbon sequestration.[32–36] ILs can be tailored to have optimal solubilities for a targeted chemical species and (im)miscibility with traditional solvents, making ILs extremely attractive as separation/extraction media.[6,37–39] ILs can also serve as multifunction tools in catalysis,[33,40–44] where they can act as a solvent to bring together both organic and inorganic species, act as a catalyst or co-catalyst, or act as a ligand source.[42,44]

The peculiar physical properties of ILs are not yet well understood. The complex relationship between molecular structure and physical properties is an important research question from both theoretical and practical standpoints.[10,45–47] Structure-property relationships, based on the earliest known ILs, developed in a rather empirical fashion.[48] A goal of theoretical research is not only to explain the trends in the physical properties that are observed experimentally, but also to understand the fundamental physics that governs IL behaviour and move toward predicting the behaviour of potential ILs based on their chemical structures.[15,49,50] The Holy Grail for ILs would be being able to accurately predict *all* of the physical properties from the chemical structures of the ions alone.

1.2 Computational Studies of ILs

The advances in computational resources are well timed for IL research.[47] Much simulation work is being done to find correlations between the molecular structure of ILs and their physical properties[13,51–55] and to determine accurate melting points of model ILs.[2,7,10,56]

Malvaldi and Chiappe studied structural and dynamical properties of a set of three salts with two-site cations and single-site anions.[45] They found orientational ordering and structural heterogeneity in the liquid phase. Ganzenmüller and Camp considered a set of five salts with one- and two-site cations and single-site anions with a size ratio of 1.3014:1.[57] They located the critical points and resolved cation translational and rotational motion in the conductivity spectra. Roy and coworkers have developed and refined a more realistic, three-site coarse grain model for an alkyl imidazolium cation and paired it with a single-site hexafluorophosphate anion.[58,59] Their studies of the liquid phase dynamics showed that the rotational diffusion coefficient appears to decouple from the viscosity as the temperature decreases.

Earlier simulations[60,61] employing simple model ions have shown that some trends in the dynamical properties of ILs can be correlated with a measure called the charge arm. The charge arm is defined by Kobrak and Sandalow as a measure of the separation of the center of charge and the center of mass.[62] It is one of the quantities we will discuss in more detail in Chapter 2.4. The simulation studies[60,61] showed that ions with small charge arms display decreased viscosity and increased diffusion and electrical conductivity, whereas ions with large charge arms show a significant increase in viscosity, constant diffusion rates, and the electrical conductivity approaches zero. While we employ simple model ions with fixed charge

arms, the charge arm is not a fixed quantity in molecular ions with conformational flexibility. Urahata and Ribeiro studied the heterogeneous dynamics of 1-butyl-3-methylimidazolium chloride using an atomistic model in MD simulations.[63] They found that the instantaneous charge arm acts as a structural signature of heterogeneous dynamics with larger charge arms being associated with slower dynamical behaviour.[63]

1.3 The Melting Points of Ionic Liquids

The melting point is a key physical property for IL applications and is the defining attribute that separates ILs from molten salts.[1] The fluid-solid transition has not received as much research attention as fluid-fluid transitions.[64] The normal melting point is the physical property we focus on in this thesis. Understanding how a variety of structural modifications influence the melting point is a key step in developing predictive tools for the rational design of ILs.[12,47,53,55,65]

It is not well understood why ILs have such low melting points compared to simple inorganic salts.[66,67] The low melting temperatures are usually explained by the differences in electrostatic interactions, namely the ion sizes, charges, and charge distribution.[66,68] There are many additional factors that nuance the relationship between the Coulombic interactions and melting points such as competing interaction types and the associated length scales, geometric considerations, and conformational flexibility.[51,55,68] While it is difficult to unravel and isolate the contributions of a single factor,[69] we outline a few of the generic features and the arguments for how they contribute to the low melting temperatures of ionic liquids.

At the level of ion structure, molecular asymmetry is usually one of the first reasons offered to explain the low melting points.[65] Asymmetric cations are more prevalent than asymmetric anions, although the anions are becoming more exotic. The ion asymmetry introduces an orientational dependence that can lead to reorientational degrees of freedom. Ion asymmetry may prevent the electrostatic ordering (lattice packing) that drives crystallization, thereby lowering the melting temperature.[7,54,63,70] The work presented in Chapters 3, 4, and 5 of this thesis study how redistributing the cation charge affects the melting temperature.

Ionic size is another clear factor that affects the melting temperature, with larger ions having weaker electrostatic interactions (electrostatic energies $\propto 1/r$) and therefore lower melting temperatures.[64,71] The work presented in Chapter 4 of this thesis examines the impacts of ion size and ion size ratios, and also examines the compounding effects of ion size, ion size ratios, and cation charge redistribution.

Conformational flexibility is another reason put forward to explain the low melting points. The mix of conformers with different shapes and charge distributions may frustrate the crystal packing.[7,52]

Combining a cation with an anion generates more factors to consider. A mismatch in ion size affects the packing and freezing behaviour. Large ions are more likely to have significant van der Waals interactions than smaller ions. The size difference can lead to a prefreezing or premelting phenomenon, where the diffusive motion of the smaller anions persists at lower temperatures than that of the larger cations. We explore the impact of size ratio in Chapter 4, and find salts with fast ion conductor or plastic crystal phases. Experimentally, salts with plastic crystal[72–74] and fast ion conductor[75] phases of ILs have been studied for potential use as solid state electrolytes.

Monoatomic ions are spherical, whereas molecular ions are typically aspherical. Just as combining two ions of different sizes introduces size ratio, combining two ions with distinct shapes introduces the possibility for shape "mismatches." Shape mismatch between the ions is often cited as a reason for the low melting points of ILs. If the mutual fit of the ion shapes is poor, the mismatch can limit the packing options.[20] Even if the ions find a densely packed structure that accommodates both ion shapes, the local arrangement of ions may lead to unfavourable interactions that destabilize the crystal structure.

Another feature that is introduced once we consider the cation/anion combination is the possible formation of ion pairs. Ion pairing has been correlated to low glass transition temperatures.[48] We also see strong correlations between directional ion pairs and low glass transition/melting temperatures in Chapters 3, 4, and 5. Ions that form strong, long-lived directional ion pairs may not interact very strongly with other neighbouring ions. The thermodynamic driving force behind solidification is the lower enthalpy in the solid phase. The lower enthalpy usually depends on particles creating strong, favourable interactions with multiple near neighbours, which is unlikely to be the case for salts that form strong, directional ion pairs.

Turning our focus to the solid, the bulk properties of the solid phase are another complicating factor for ILs. The crystal structure itself must be known in order to find a relationship between melting temperature and ion structure.[76] The strength (large lattice energy), or rather lack thereof, of the crystal structure is often cited as a reason for low melting ILs.[51] ILs, with their diverse properties, can vitrify,[15,48,77] crystallize,[51] crystallize with orientational disorder, crystallize as plastic crystals,[73,78–80] crystallize as fast ion conductors,[75,81] form liquid crystals,[77,82,83] and/or exhibit polymorphism.[15,55,77,84] We have observed all of these solidification

behaviours with our simple salt models except for the formation of liquid crystals. We would have to move away from spherical ions to induce liquid crystal behaviour. The dynamics in the solid phases of ionic liquids, including oscillations, reorientations, rotations, conformational changes, are especially active near the melting transition. The rich diversity of thermal motions in the solid add nuance to locating the onset and end of the solid-liquid (s-l) transition.

It is important to acknowledge the interdependencies among the levels of ion structure, pair energies, bulk liquid structure, and crystal packing that make it very difficult to isolate qualitative trends in melting temperatures.[52] The factors given here, and their interdependencies, support the idea that the morphologies of ILs are more complex than that of molten salts,[1] and particularly, the origin of the low melting temperatures is an important research question.

1.4 Experimental Melting Points

Normal melting points of pure ILs are a challenge to determine accurately. The main difficulty lies in obtaining pure, bulk samples (free of other ions, water, and carbon dioxide gas) and using a method that is reliable and accurate. IL samples are commonly dried under vacuum for hours to remove water and then stored in an inert atmosphere before measuring the melting point. It has been reported that dissolved carbon dioxide gas in tetrabutylammonium tetrafluoroborate can reduce the melting point by 120 K, from 429 K to 309 K at 150 bar of CO_2.[26,85]

Experimental melting points are subject to the compounding issues of sample purity, variations in sample preparation procedures, and the accuracy of the method employed. Differential scanning calorimetry and visual observation are two common

approaches for determining melting points. Reported experimental melting points for the same salt measured using different methods (and samples) do not necessarily agree within the given uncertainties of the method and are commonly separated by 25-35 K.[26] Reliable melting point data is limited to the popular ILs that have been characterized and studied extensively. One common ionic liquid, 1-hexyl-3-methylimidazolium bis[trifluoromethyl)sulfonyl]amide, transitions to the liquid state from the liquid-quenched glass around 265 K, and from the crystal around 271 K.[26,86] IUPAC has proposed to use this common ionic liquid as a reference IL with its relatively narrow melting point range of 266-272 K.[26,87] The limited availability of accurate melting point data makes establishing empirical trends difficult.

The discrete nature by which molecular ions can be modified means that, within a homologous series of salts, substituting one (set of) neutral atom(s) for another can change the ion geometry (size and shape), mass and mass distribution, and the charge distribution of a molecular ion. Isolating how a single physical attribute affects the melting point using a series of salts with molecular ions and experimental data increases the complexity of the task dramatically.

In order to connect the results obtained here for coarse grain model salts to experimental ones, we take a brief look at the melting point trends across a series of alkyl-substituted ammonium bromide salts in Chapter 6.

1.5 Simulation Methods for Estimating Melting Temperatures

Equilibrium melting temperatures are well defined thermodynamically. The chemical potentials of both phases vary slowly with pressure. Determining the precise coexistence points using computer simulations is challenging, especially for molecular crystals which are complex.[88]

The *s-l* transition is impossible to characterize completely without knowledge of the solid phase structure. In this work, most of the salts (about 84%) spontaneously crystallize when cooled from the liquid phase, while a minority of salts become trapped in "glassy" states. We explore the solid state structures of the glassy salts by preparing and heating common crystal structures using NPT molecular dynamics. Another method of determining crystal structures was also developed for this project. A genetic algorithm was written to find low energy unit cells of salts. The calculation details are described in Appendix A and the program is described in Appendix C.

Different approaches have been developed to estimate melting points from simulations and, not surprisingly, the more accurate methods tend to be computationally intensive.[69,89,90] A collection of methods has been recently reviewed in an excellent work by Zhang and Maginn.[89] The two methods we use, the hysteresis method and two-phase simulations, are described briefly here and in more detail in Chapter 2.

We use the hysteresis method,[91] as an initial estimate of the melting point in this work. The hysteresis method determines the melting point from the transition

temperatures of freezing the liquid and melting the solid. The freezing and melting transitions do not occur at the same temperature due to hysteresis. Hysteresis describes the phenomenon of a lag in response to a change in conditions or forces acting upon a system. The state of a hysteretic system depends on the history of the system as well as the current conditions. When the liquid is cooled, the system will remain liquid below the equilibrium freezing point (supercooling) and when the solid is heated it will remain solid above the equilibrium melting point (superheating). Hysteresis is a non-equilibrium phenomenon, and the dominant cause of the hysteretic behaviour around the *s*-*l* transition is the free energy barrier associated with nucleation.[91]

One disadvantage of using the hysteresis method for the ionic systems simulated in this thesis is that the thermal width of the hysteresis is large and spans hundreds of degrees. To refine the melting temperature estimate, we use NPT MD simulations that start as a composite of two phases. The final solid and liquid configurations from the hysteresis simulations are used to create composite supercells with two *s*-*l* interfaces. We use the two-phase simulations to narrow the transition range to 50 K.

In this work, we are interested in the melting point trends as the ion parameters are systematically varied and not the exact melting points of individual salts. Therefore, our estimates of the melting points of individual salts are not the most accurate possible. However, the methods employed are expedient and sufficient for identifying trends across sets of salts.

Chapter 2

Models and Methods *

We employ molecular dynamics (MD) simulations to estimate the melting points of sets of coarse grain model salts. In this chapter, we first present the details of the ion models, and then the simulation methods.

2.1 Ion Topologies

We use a coarse grain approach in this work because it provides insights into the influence of particular molecular features. By reducing the complexity of the ions, relationships among model parameters and observables, particularly melting points, become more prominent. Coarse grain models have been used to study the fluid phases of ILs and have been successful at reproducing some observed behaviour.[60,61,92]

*Parts of this chapter have been published. E. K. Lindenberg and G. N. Patey, "How distributed charge reduces the melting points of model ionic salts," J. Chem. Phys. **140**, 104504 (2014).

All of the salts we consider can be viewed as extensions of the so-called restricted primitive model (RPM). The RPM is an equimolar mixture of equal-sized, charged hard spheres, and is perhaps the simplest model of inorganic salts.[93] We modify this model by introducing Lennard-Jones (LJ) interactions, by changing the cation-anion size ratio, and by redistributing a fraction of the cation charge away from the ion center. Charge redistribution is not an applicable extension of the RPM for monoatomic ions, where the center of mass and the center of charge necessarily coincide, however, it is applicable for molecular ions, which are common in real ILs.

Each ion is monovalent and has a single LJ interaction site that, for our purposes, defines the ion center. The LJ parameters are specified in Chapter 2.2. Each ion has a total mass of 1.993×10^{-25} kg (120 amu), and the mass distributions are discussed further in Chapter 2.3.

We present a brief overview of each ion geometry before specifying the complete ion parameters. A summary table is included at the end of this section where we list the salts studied in the following chapters.

The 1C Ion

The 1C ion is closely related to the ions in the RPM. The ions have a single interaction site located at the ion center that carries the entire unit charge. Unlike the RPM ions, the 1C ions also interact via a LJ potential. The 1C - 1C salt acts as a reference salt for our work and is included in each chapter. The deviations in the melting points of the other salts are measured relative to the 1C - 1C salt.

The 2L Ion

Ions with some charge located at an off-center site are labelled 2L, indicating two interaction sites in a linear arrangement, as shown in Fig. 2.1.

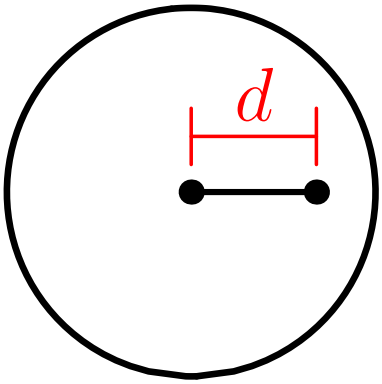

Figure 2.1: A diagram of the 2L model ions. Each ion carries a total charge of $\pm 1e$, where e is an elementary charge. The site at the ion center interacts via a Lennard-Jones potential and, in most cases, an electrostatic potential. The off-center site interacts via an electrostatic potential only. The two parameters for the 2L ions are the amount of charge at each interaction site and the distance between the two sites, d.

The 2L ion parameters are the distance between the sites d and the fraction of charge on each site. We examine 2L ions with four different charge distributions, with 1/3, 1/2, 2/3, and all of the unit charge on the off-center site. The ion labels are 2Lfc-d, where fc is the fractional charge on the off-center site as a rounded percentage, and d is the separation distance between the two interaction sites on the same ion, expressed in units of 0.01 nm. For example, a 2L67-12 ion has 2/3 of the total ion charge on the off-center site, which is located 0.12 nm from the ion center.

The 3s Ions

The 3s ions are a set of ions with three interaction sites. The third ion site is another off-center charge site, which, like the off-center charge site in the 2L ions, is located a distance d from the ion center. The third site introduces another model parameter, θ, the angle made between vectors from the ion center to the two off-center sites. We systematically vary θ across seven values: 60°, 90°, 105°, 120°, 135°, 150°, and 180°. An example of a labelled cation is shown in Fig. 2.2, and minimalist diagrams of the entire 3s ion set are shown in Fig. 2.3.

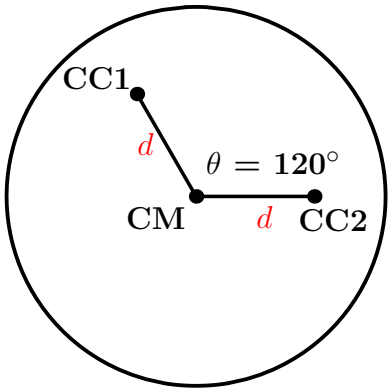

Figure 2.2: A fully labelled schematic of the 3s(120°) model ion.

The 3s ion geometry labelling follows a convention similar to that of the 2L ions, given as 3s(θ)fc-d, which specifies the ion geometry, fractional charge distribution, followed by the extent of the charge separation d. The angle θ is in degrees, fc denotes the percentage of charge on interaction site CC1, and d follows the same convention as the 2L ions. An example of a full 3s ion label is 3s(105°)33-18. The ion label gives the number of sites (3s), the angle between the two off-center sites (105°), the amount of charge at CC1 [fc = 33, $q(CC1) = 1/3$], and finally, the displacement distance d is given in units of 0.01 nm (0.18 nm).

In the 3s - 1C salts we consider, the off-center interaction sites are both the same distance d from the ion center. The charge distribution fc specifies the amount of charge on one off-center site (CC1), while the other off-center site (CC2) always carries 1/3 of the unit charge. In Chapter 5, we study two variations in charge distribution. In the first case, the CC1 site carries 1/3 of the charge ($fc = 33$) and the ion center carries 1/3 of the unit charge. In the second case, CC1 carries 2/3 of the unit charge ($fc = 67$) and the ion center is uncharged (but still interacts via the LJ potential).

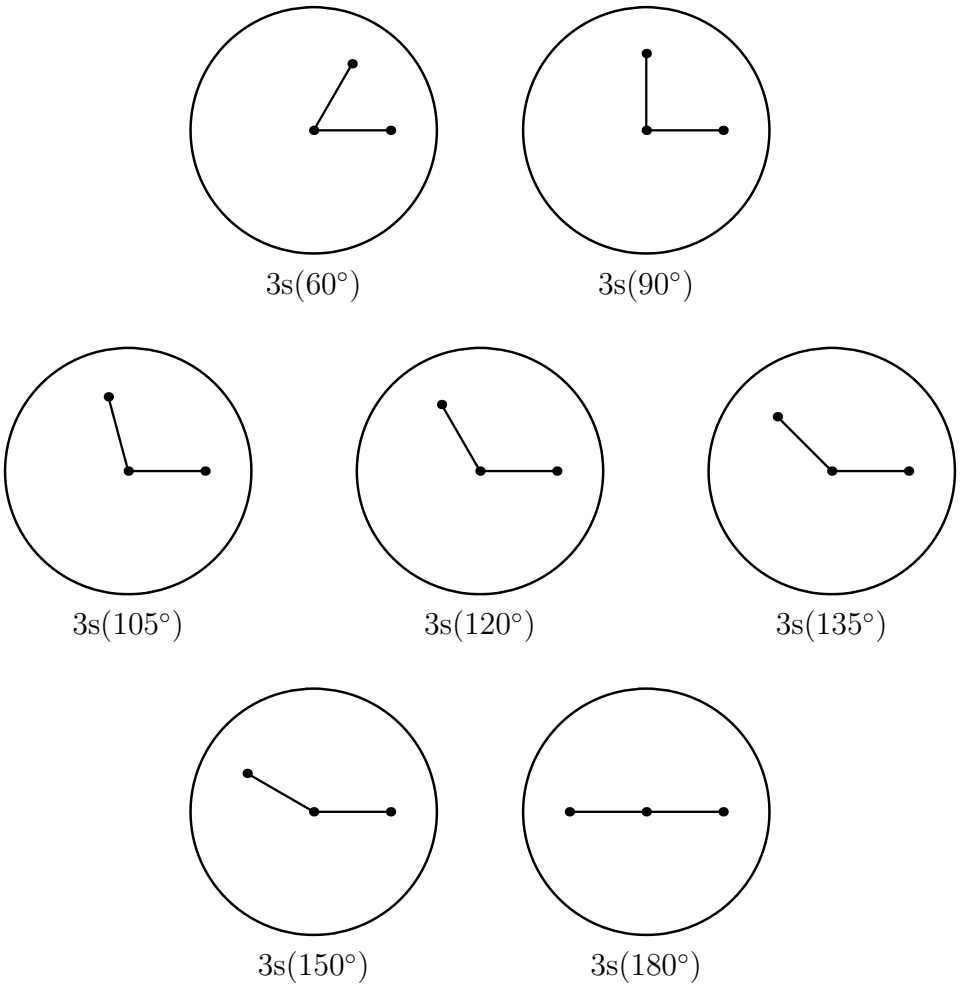

Figure 2.3: Diagrams and labels of the 3s ions. The cationic version of these seven ions, each paired with the 1C anion, are studied in Chapter 5.

Ion Size Ratios

We have defined the general features of the ion topologies in the preceding sections, and now turn to the combination of two ions to create a salt. The relative size ratio of the two ions, as well as the absolute ion sizes are both relevant parameters to be varied. With the exception of the salts considered in Chapter 4, the cations and anions are the same size, with a LJ diameter $\sigma = 0.50$ nm.

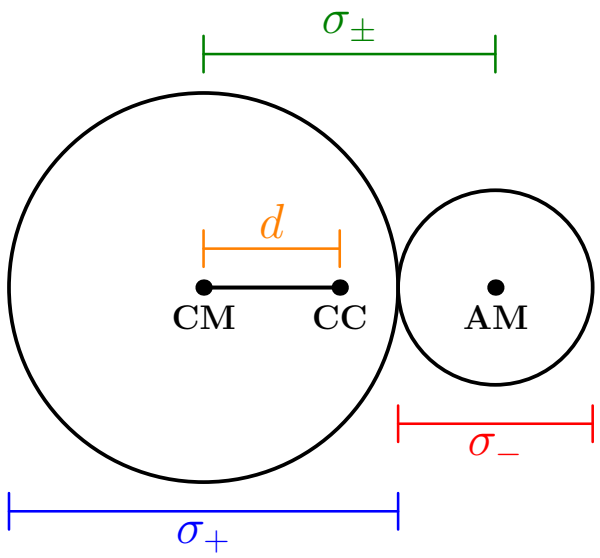

Figure 2.4: A schematic of the size-asymmetric model salts. The interaction sites, CM, CC, and AM denote the cation center, cation off-center charge site, and anion center, respectively. The size ratios are varied in Set A by fixing $\sigma_\pm$ to 0.50 nm while varying σ_+ and σ_-. In Set B, the size ratios are varied without a constraint on $\sigma_\pm$; instead σ_- is held constant while σ_+ and $\sigma_\pm$ increase. In addition to varying the size ratio, we also examine two cation charge distributions where either all of the unit charge is located at CM, or 2/3 of the unit charge is located off-center at the CC site, at a distance d from the ion center.

The cation:anion radius ratio is controlled by the length parameter of the LJ interaction, σ. Allowing the ion sizes and resulting size ratios to vary creates three different length scales to consider, σ_+, σ_-, and $\sigma_\pm$, which affect the cation-cation, anion-anion, and cation-anion interactions, respectively. We vary the cation:anion radius ratio in two different ways, generating two sets of size-asymmetric salts. In Set A, the distance between cation-anion centers $\sigma_\pm$ is held fixed, which isolates the influence of size asymmetry and minimizes the changes in strength of the attractive electrostatic interactions. In Set B, σ_+ is increased (which also increases $\sigma_\pm$) while σ_- is held constant. The salts in Set B are somewhat more practical representations of ILs because $\sigma_- = 0.50$ nm was initially chosen to be consistent with the "size" of typical IL anions. We explore seven different size ratios, ranging from 1:1 to 3:1. The parameters for each size set are given in Table 2.1. Note that the size-symmetric cases, A100 and B100, are identical; we refer to these salts using the A100 label only.

Table 2.1: The two sets of size parameters of the salts considered in this work. In Set A, $\sigma_\pm$ is constrained to 0.50 nm, while in Set B, the anion radius is held constant at 0.50 nm and $\sigma_\pm$ is unconstrained.

Size Ratio	Label	Set A		Set B	
		σ_+ (nm)	σ_- (nm)	σ_+ (nm)	σ_- (nm)
1:1	100	0.500	0.500	0.500	0.500
1.33:1	133	0.571	0.429	0.667	0.500
1.67:1	167	0.625	0.375	0.833	0.500
2:1	200	0.667	0.333	1.000	0.500
2.33:1	233	0.700	0.300	1.167	0.500
2.67:1	267	0.727	0.272	1.333	0.500
3:1	300	0.750	0.250	1.500	0.500

In Chapter 3, we consider five different sets of charge distributions in size-symmetric salts. In Chapter 4, we vary the size ratios and focus on two cation charge distributions, where the entire unit charge is located at the cation center (labelled 1C), or where 2/3 of the unit charge is displaced from the cation center (labelled 2L67). We chose the 2L67 charge distribution because the size-symmetric 2L67 - 1C salt series was one of two that obtained melting points of 50% of the size-symmetric 1C - 1C salt in Chapter 3. Also, we found that the series of size-symmetric 2L67 - 1C salts captured the typical behaviour of the salts we observed over the larger set of charge distributions. We vary the charge distribution on the 2L67 cations by changing d, which ranges from 0.06 nm from the cation center up to the edge.

The labels for the salts give the size ratio information first, followed by the cation and anion geometries. For example, the A233 2L67-18 - 1C model salt indicates the size ratio as A233, meaning the salt is in Set A, with a size ratio of 2.33:1, (the number gives the cation size relative to the anion as a percentage). The cation geometry is specified next as 2L67-18, meaning 67% of the unit charge is displaced $d = 0.18$ nm from the cation center. Finally, the last term in the label specifies the anion geometry as 1C. The vast majority of the salts considered here are combinations of a 2L67 cation with a 1C anion; it is the size ratio information and d that are the key variables in Chapter 4. Note that the size ratio (A100) is excluded from the size symmetric salt labels in Chapters 3 and 5.

As the ion sizes change, the cutoff distance for the short-range interactions also changes. The short-range interaction cutoff distance is maintained at approximately $3.2\sigma_+$ and increases as the cation size increases. The cutoff distances are given in Table 2.2.

Table 2.2: The short-range interaction cutoff values (R_{cut}) for the size-asymmetric salts. The LJ diameter of the cation, σ_+ is larger than the anion for all of the size-asymmetric salts and was used to determine R_{cut} as $R_{cut} \approx 3.2\sigma_+$.

Size Ratio Label	σ_+ (nm)	R_{cut} (nm)
A100	0.500	1.70
A133	0.571	1.83
A167	0.625	2.00
A200	0.667	2.14
A233	0.700	2.24
A267	0.727	2.33
A300	0.750	2.40
B133	0.667	1.83
B167	0.833	2.00
B200	1.000	2.14
B233	1.167	2.24
B267	1.333	2.33
B300	1.500	2.40

2.2 Ion Interaction Parameters

The ions have a combination of electrostatic and LJ interactions because we want to include both ionic and molecular character in our model ions. The ions interact through the pair potential

$$u(r_{ij}) = 4\varepsilon_{ij}\left[\left(\frac{\sigma_{ij}}{r_{ij}}\right)^{12} - \left(\frac{\sigma_{ij}}{r_{ij}}\right)^{6}\right] + \frac{1}{4\pi\epsilon_0}\sum_{\alpha\,,\beta}\frac{q_{i\alpha}\,q_{j\beta}}{r_{i\alpha j\beta}}, \tag{2.1}$$

where ε_{ij} and σ_{ij} are the LJ energy and length parameters for the LJ interaction between ions i and j, r_{ij} is the distance between the LJ sites on ions i and j, ϵ_0 is the permittivity of free space, $q_{i\alpha}$ is the charge on ion i at site α. The $r_{i\alpha j\beta}$ value is the distance between site α on ion i and site β on ion j, where both sites carry charge.

Each ion has one LJ interaction site at its center. The LJ energy parameter is identical across all models; $\varepsilon_{ij} = 6.0 \times 10^{-21}$ J. The value of ε_{ij} is consistent with earlier work[60,61,92] and is roughly consistent with the model parameters of a typical hydrocarbon, neopentane.[94]

The ion topologies were set up with each ion site as an "atom" with a label, mass, charge, and LJ parameters. The connectivities between interion sites were set up as distance constraints. An example topology file for the A100 2L100-16 - 1C salt is given in Appendix F.

In Chapters 3 and 5, the LJ length parameter is held constant across all ion models, $\sigma = 0.50$ nm. The ion diameter of 0.50 nm approximates the ion "size" in some common ILs, such as the PF_6^- or BF_4^- anions. In Chapter 4, the LJ length parameter changes to create salts with cation-anion size ratios varying

from 1:1 to 3:1. The cation-anion length parameter, σ_{ij}, is calculated using the Lorentz-Berthelot mixing rules, $\sigma_{ij} = (\sigma_{ii} + \sigma_{jj})/2$.

In the charge-centered case, the pair potential is spherically symmetric and depends only on the distance from the ion center. When d increases in the 2L ions, part of the charge is moved closer to the ion surface. For the 2L - 1C salts, the location and depth of the potential minima changes dramatically from the 1C - 1C case. Three dimensional (3D) surface plots of the pair potential for select 2L67 - 1C salts are shown in Fig. 2.5. Each plot shows the potential energy surface around a particular cation, as experienced by a 1C anion.

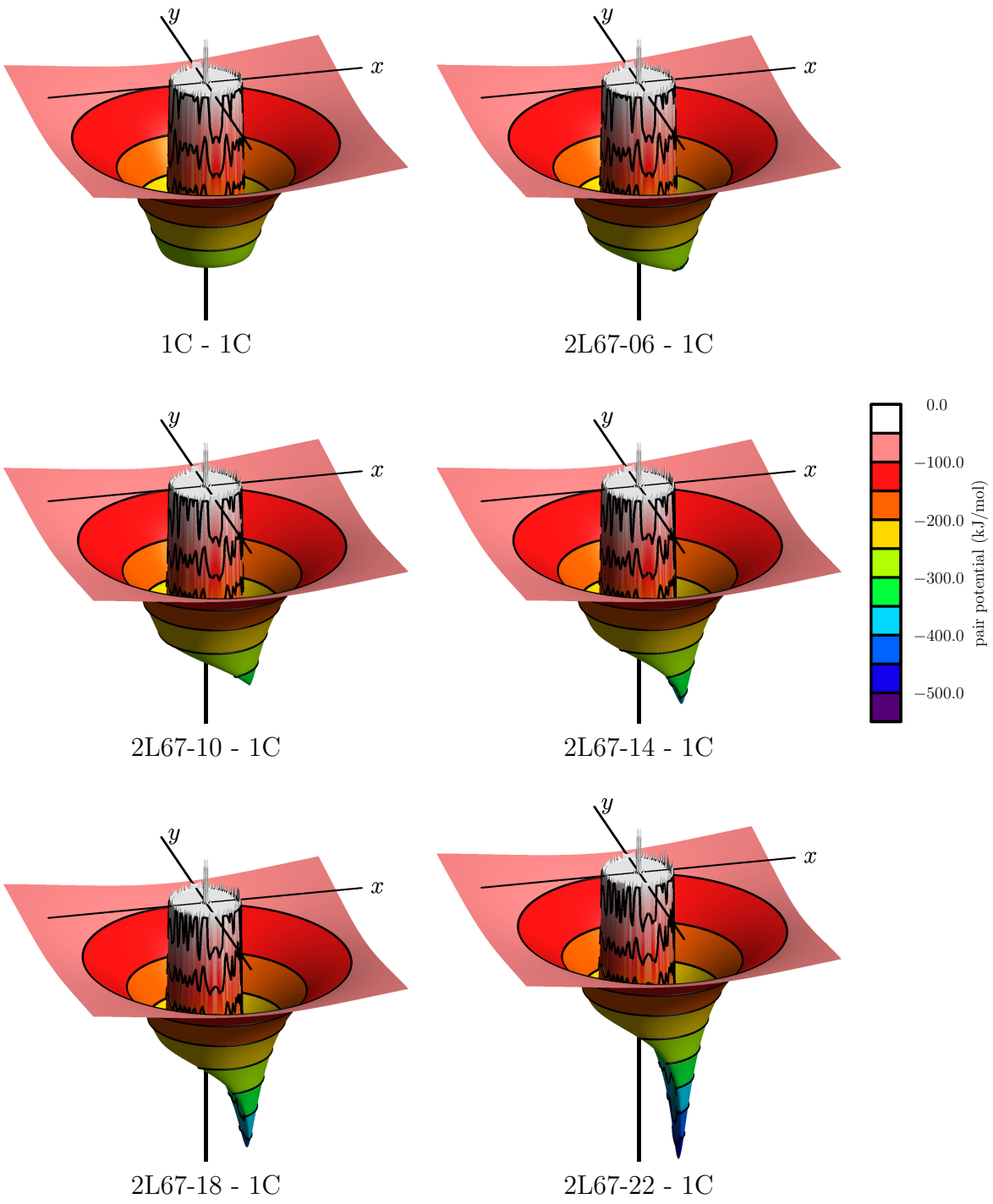

Figure 2.5: 3D potential energy surfaces around the cation for the 1C anion in a series of size-symmetric ion pairs. Each cation center is shown at the origin with the circle depicting the repulsive core (where $u(r_{ij}) > 0$). The off-center charge site on the 2L67 cations is aligned with the $+x$ axis.

2.3 Ion Masses

For the 2L and 3s cations, the ion center defined by the LJ site is distinct from the ion's center of mass because a fraction of the mass is located at the off-center site(s). The amount of mass at each interaction site depends on the cation displacement distance, d. The distribution was selected to minimize fluctuations in the moments of inertia as d varies. The distribution of mass affects the dynamics, but does not affect equilibrium properties such as the normal melting points. The masses assigned to the ion center (labelled CM) and each off-center ion site (labelled CC) are given in Table 2.3.

Table 2.3: The mass distribution for the ions with off-center interaction sites. The total mass of each ion is 120 amu (1.993×10^{-25} kg), and the mass distribution over the interaction sites varies with the separation distance d. For the 3s ions, both off-center sites were assigned the same mass.

	2L Ions		3s Ions	
d (0.01 nm)	m(CM) (amu)	m(CC) (amu)	m(CM) (amu)	m(CC) (amu)
0	120.00	—	120.00	—
6	70.00	50.00		
10	102.00	18.00		
14	112.00	8.00		
18	115.00	5.00	115.00	2.50
22	116.75	3.25		
26	117.75	2.25		
30	118.25	1.75		
34	118.70	1.30		
≥ 42	118.70	1.30		

2.4 Charge Arm

The charge arm, defined by Kobrak and Sandalow[62] as $|q_{\text{off center}}|\, d$, is a useful combination of both parameters that occur for 2L ions. The notion of charge arm is a defining feature in the set of 2L - 1C ion models considered here. In the present work, we use the normalized charge arm

$$L_c = \frac{|q_{\text{off center}}|\, d}{|q_{\text{ion}}|\, R_{\text{ion}}}\,, \tag{2.2}$$

where q_{ion} is the total ion charge and R_{ion} is the radius of the ion. In this work, all the ions considered are monovalent, so $|q_{\text{ion}}| = 1e$. With the exception of the work in Chapter 4, $R_{\text{ion}} = 0.25$ nm. In Chapter 4, R_{ion} ranges from 0.25 nm to 0.75 nm. The charge arm characterizes the geometry of one ion only, and does not consider changes to the other ion. In Set A of Chapter 4, the cation charge geometry and both the cation and anion radii change, so a measure that reflects only the change in the cation may be misleading. Rather than using L_c for Set A, we simply correlate the melting temperatures with d for each size ratio (Fig. 4.5). In Set B of Chapter 4, however, the anion size is fixed, and it is instructive to consider the changes to the salt through the normalized charge arm (Fig. 4.7).

A model cation with a smaller (larger) charge arm is somewhat analogous to a heterocyclic cation with a shorter (longer) alkyl side chain. In the model ions, displacing the charge away from the ion center creates a stronger electrostatic interaction on one side of the ion and effectively "exposes" the van der Waals interaction on the opposite side.

2.5 Minimum Potential Energies of Isolated Ion Pairs, U_{iso}^{IP}

The minimum potential energy for an isolated pair of ions, U_{iso}^{IP}, is another useful quantity for characterizing the salt models. The pair potential considers the geometry of both ions in the salt, rather than just one, which permits comparison across salts where the geometries of both ions change. A linear arrangement of CM-CC-AM, as depicted in Fig. 2.4, is used to compute U_{iso}^{IP}.

Once we have determined a crystal structure for a salt, we use the ratio of the average configurational energy per ion pair in the crystal at the melting temperature to the minimum potential energy of an isolated ion pair, $\bar{U}_s^{\mathrm{IP}}/U_{iso}^{\mathrm{IP}}$, to provide some insight into what fraction of the crystal energy is coming from ion pairing rather than from the packing arrangement. This ratio is somewhat analogous to the Madelung constant for point charges on a perfect lattice. The Madelung constant is a factor that relates the total electrostatic potential of a specific ionic crystal structure to the minimum distance between two counterions, r_0, by

$$U_{ES} = M\frac{q_+q_-}{4\pi\epsilon_0 r_0}, \tag{2.3}$$

where M is the Madelung constant. By rearranging Eq. (2.3) and substituting in the minimum potential energy of an isolated ion pair, $U_{iso}^{\mathrm{IP}} = q_+q_-/4\pi\epsilon_0 r_0$, the expression for the Madelung constant becomes

$$U_{ES}/U_{iso}^{\mathrm{IP}} = M. \tag{2.4}$$

Like the Madelung constant, $\bar{U}_s^{\mathrm{IP}}/U_{iso}^{\mathrm{IP}}$ is a measure of how much stability is gained in the solid phase relative to a collection of isolated ion pairs.[65] At a ratio of 1.0, the solid would have no energetic advantage over an equal number of isolated ion pairs. However, $\bar{U}_s^{\mathrm{IP}}/U_{iso}^{\mathrm{IP}}$ is unlike the Madelung constant in that it includes the LJ interactions, thermal fluctuations, and any lattice defects present.

2.6 Outline of the Salts Studied in This Thesis

In Chapter 3, we examine a set of 2L - 1C salts made by combining a 2L cation with a 1C anion. The size-symmetric 1C - 1C salt, like the RPM, is perfectly symmetric with respect to sign reversal on the charges. The 2L - 1C salts extend the simple models by introducing asymmetric charge distributions, which are more realistic for modelling ionic liquids. The choice of redistributing the cation charge is arbitrary and reversing the charge signs would produce a 1C - 2L salt with identical physical properties. Chapter 3 examines the effect of varying the charge distribution on the 2L cations. The ions are the same size and the anion is always a 1C ion.

In Chapter 4, we examine how the absolute ion sizes and size ratios affect the melting temperatures of 2L67 - 1C and 1C - 1C salts. The coarse grain model salts considered in Chapter 4 mimic two features commonly found in ionic liquids, size asymmetry and distributed cation charge.

In Chapter 5, we study the set of 3s - 1C salts to further explore the affect of cation charge distribution on the *s*-*l* transition. The ions are size-symmetric and always paired with a 1C anion. While we vary θ in this chapter, the displacement distance d is held fixed at 18 (0.18 nm). The displacement distance is far enough to have an effect on the melting temperature, yet not so far that ion pairing dominates

the ion interactions.

Table 2.4: Table of the salts studied in each chapter of this thesis. Each chapter also includes 1C - 1C salt(s) as the reference salt(s).

Chapter	Cation(s)	Anion(s)	Ion Sizes σ (nm)	d values (0.01 nm)
3	2L	1C	0.50	0 - 24
4 (Set A)	2L67	1C	0.25-0.75	0 - 26
4 (Set B)	2L67	1C	0.50-1.50	0 - 58
5	3s	1C	0.50	18

2.7 Hysteresis Method for Estimating Melting Temperatures

Since we are interested in melting point trends as the ion parameters are systematically varied rather than determining the exact melting point of individual salts, our estimates of the melting points are not the most accurate possible. However, the methods we employ are expedient and sufficient for identifying trends across sets of salts.

One relatively simple method for estimating melting points is the so-called hysteresis method proposed by Luo *et al.*[91] A hysteresis loop is evaluated by supercooling the liquid until it freezes at a temperature below the thermodynamic melting point and superheating the solid until it melts at a temperature above the thermodynamic melting point. The melting point, T_m, is estimated using the limits

of supercooling and superheating as[91]

$$T_m = T_+ + T_- - \sqrt{T_+ T_-}\,, \tag{2.5}$$

where T_+ is the highest temperature of the superheated solid and T_- is the lowest temperature of the supercooled liquid.

When a system is supercooled or superheated, the difference in chemical potential provides thermodynamic incentive to freeze or melt. Under isobaric conditions, the rate of heating or cooling determines the maximum extent of the superheating or supercooling, and has been established as[91,95]

$$\beta \propto \theta_c (1 - \theta_c)^2 \tag{2.6}$$

where β is a dimensionless nucleation barrier parameter and θ_c is either the maximum extent of superheating ($\theta_+ = T_+/T_m - 1$) or supercooling ($\theta_- = 1 - T_-/T_m$). The nucleation barrier parameter, β, should be identical for both melting and freezing, so

$$\theta_+ (1 - \theta_+)^2 = \theta_- (1 - \theta_-)^2. \tag{2.7}$$

From Eq. (2.7), an expression for the melting point, T_m, [Eq. (2.5)] is obtained by using the quadratic formula.

The hysteresis method has been used to obtain reasonably accurate estimates of the melting points of a pure LJ system[91] and of molecular solids.[88,96] Since we are using rather large temperature increments of 50 K, we employ Eq. (2.5) as an initial estimate.

We started each simulation by equilibrating the salt in the liquid phase. The initial simulation temperature was 1600 K for most salts. Some salts evaporated at 1600 K, so the initial temperature was lowered until we found a stable liquid. The molten salts were then cooled using serial NPT runs with temperature differences of 50 K. The freezing of the supercooled liquid was identified by significant decreases in the average configurational energy and volume, and confirmed by inspection of the radial distribution functions and mean square displacements. The solid was then heated following an analogous procedure. For most of the salts, the solid-liquid transition temperatures from the cooling and heating cycles show evidence of hysteresis.

A few of the salts (about 16%) did not crystallize under our simulation conditions and time scales, but tended to form "glassy" states as they were cooled. These salts are discussed in the relevant results chapters. The vitrification creates three related issues if one wishes to estimate T_m using Eq. (2.5). We cannot determine the values of T_- or T_+ directly from cooling and heating curves, and we do not know which crystal structure(s) exist below the glassy state. Zheng *et al.*[88] have argued that a reasonably good estimate of T_- is given by a glass transition temperature, T_g, defined as the temperature where the diffusion coefficient falls below 10^{-11} m^2/s on the cooling curve, and we follow this prescription here. The value of T_+ can be determined by heating a prepared crystal until it melts, if the appropriate crystal structure is known.

To find candidate crystal structures, we set up common crystal types (such as CsCl, NaCl, NiAs, and wurtzite) for each glassy salt. The initial crystal density was set at $\rho^* = 1.1$, where $\rho^* = N\sigma^3/V$ (N is the number of ions, σ is the LJ diameter, and V is the volume of the simulation cell). The configurational energies

were minimized, and the crystals were heated from $T = 50$ K to determine T_+. Upon heating, some of the solids rearranged into more stable crystal structures, which are discussed in the relevant results chapters. The configurational energies of the new crystal structures were minimized for each of the glassy salts and the crystals were heated beginning at 50 K, as with the other prepared crystals.

2.8 Two-Phase Simulation Method for Estimating Melting Temperatures

To refine melting point estimates, we simulated supercells of $N \approx 1600$ (Chapter 3) or $N \approx 4000$ (Chapters 4 and 5) particles prepared with two solid-liquid interfaces. The two-phase simulation setup, shown in Fig. 2.6, is expected to eliminate some of the kinetic barriers to homogeneous nucleation, and narrow the range of our melting temperature estimates with respect to the thermal range of the hysteresis loops (T_- to T_+). From the hysteresis simulations, we have liquid and solid configurations in 50 K increments between T_- and T_+. We construct a *s-l-l-s* composite from the solid and liquid configurations for each simulation temperature between T_- and T_+. We use each composite as the initial configuration for a short NVT equilibration simulation and then a longer NPT simulation. During the simulations, each system usually evolves into a single phase.

The series of independent two-phase simulations carried out in 50 K increments between T_- and T_+ determine another two transition-related temperatures. The highest temperature at which a two-phase simulation evolved into a solid is denoted T_s, and the lowest temperature at which a two-phase simulation evolved into a liquid is denoted T_l. The difference between T_s and T_l is usually 50 K, the

temperature grid spacing between independent two-phase simulation runs. In a few cases, the two-phase simulations did not evolve into a single-phase; both phases persisted through the entire simulation. The persistence of both phases indicates that the salt is at or near its melting temperature, rather than clearly above or below it. For these exceptions where a two-phase simulation ended apparent coexistence, we take the apparent coexistence temperature as T_s and the first temperature that gives a pure liquid as T_l.

An example configuration of the two-phase simulations is shown in Fig. 2.6. The central simulation cell and the simulation cell with periodic images in two directions are both shown. The boundaries around the central simulation cell are drawn in black. The periodic images are shown to emphasize that the number of particles and their arrangement in the *s*-*l*-*l*-*s* composite cell should emulate bulk behaviour for each phase.

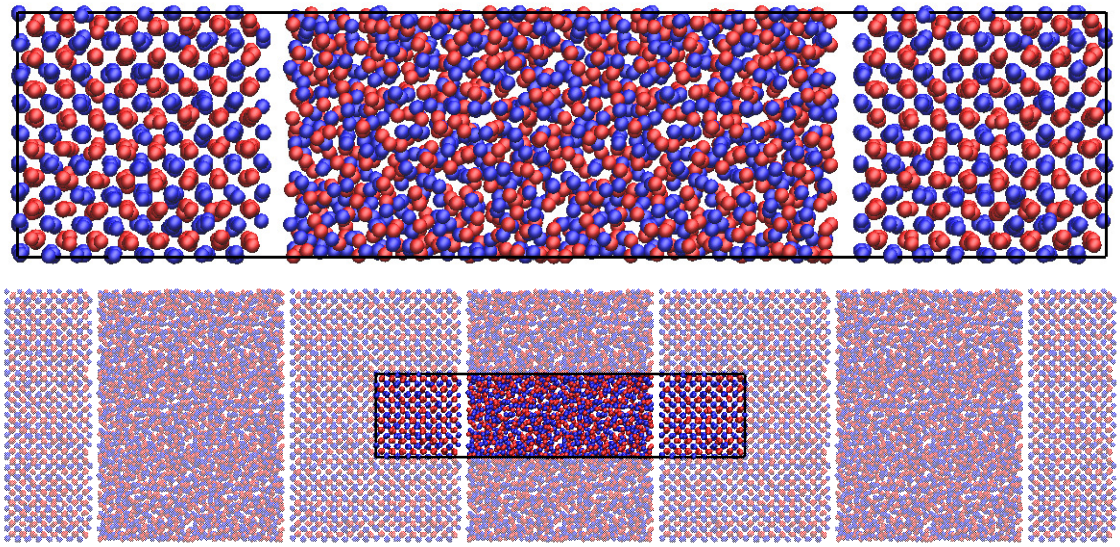

Figure 2.6: Snapshots of the initial configuration for the two-phase simulations for the size-symmetric 1C - 1C salt at $T = 1250$ K. The full simulation cell (top) and the simulation cell with periodic images in two directions (bottom) are shown. Periodic boundary conditions were used for all of the molecular dynamics runs in this thesis, including the two-phase simulations. The cations and anions are shown in blue and red, respectively. The ions are not shown to scale to highlight the arrangement of the crystal.

2.9 Simulation Details

The hysteresis loop simulations were done using Gromacs 4.5.4[97–99] in Chapters 3 and parts of 4, whereas Gromacs 4.6.2 was used for some of Chapter 4 and all of the simulations in Chapters 5. The change in Gromacs versions coincided with a system upgrade on Compute Canada's computing cluster Orcinus.

To start the single phase simulations in the hysteresis loops, the coarse grain ions were arranged in a CsCl crystal structure at a reduced density of 0.8 and equilibrated at sufficiently high temperatures to maintain the liquid phase. The systems were cooled and heated by taking the final frame of one 4.0 ns NPT simulation at a given temperature and using it as the initial configuration for the next 4.0 ns NPT simulation at a temperature 50 K lower or higher. Example Gromacs input files (*.top, *.mdp, *.gro) and the execution script (*.pbs) are included in Appendix F.

Each simulation in the hysteresis cycles was executed in the NPT ensemble with a pressure of 1.0 bar. The number of particles in each simulation varies. In Chapter 3 we used $N = 432$ particles (216 ion pairs) whereas in Chapters 4 and 5, we used $N = 1024$ particles (512 ion pairs). We did not find any significant discrepancies in our final results based on the version of Gromacs used, or any significant system size dependencies.

All simulations were done using custom forcefields to specify the ion topologies as described earlier. A leap-frog integrator propagated the system through time with a time step of 1.0 fs for all runs. The trajectories were 4.0 ns long with the first 2.0 ns for equilibration. Structural and dynamic properties were analyzed over the final 2.0 ns, except for radial distribution functions (rdfs), which were analyzed over the last 1.0 ns.

We used a Nosé-Hoover thermostat[100–102] and a Parrinello-Rahman barostat[103,104] throughout. The Nosé-Hoover thermostat regulated the temperature of the system using two coupling groups, one for the cations and one for the anions. The relaxation time of the thermostat was 0.10 ps. An isotropic Parrinello-Rahman barostat was used for the runs in cooling and heating cycles with a relaxation time of 5.0 ps; the compressibility of the salt was set to 3.0×10^{-5} bar^{-1} along the three primary axes, and 0.0 otherwise.

Periodic boundary conditions and the minimum image convention were use for the short-ranged interactions, which were spherically truncated at 1.70 nm for the size symmetric salts, and at approximately $3.2\sigma_+$ for the size asymmetric salts. The cutoff radii used in Chapter 4 are specified in Table 2.2. Long-range corrections were applied to the LJ energy and pressure. The long-ranged electrostatic interactions were accounted for using the Particle Mesh Ewald (PME) method[105] with a Fourier spacing of 0.20 nm. The constraints on "all-bonds" between interion sites were maintained using the Lincs algorithm.[106]

The simulation procedure for heating the prepared crystal structures is the same as the cooling and heating procedure, but uses a larger number of ions ($N =$ 686 to 2240) and an anisotropic Parrinello-Rahman barostat to maintain the pressure in the solid phase.

While the hysteresis simulations were split across two versions of Gromacs, the two-phase simulations were done with Gromacs 4.6.2, with the exception of the work in Chapter 3. There is some duplication of salts across chapters, particularly the size-symmetric 2L67 - 1C salts, which were studied in both Chapters 3 and 4. For the duplicated salts, the simulations were carried out within each set for consistency. The results from Gromacs 4.6.2 with $N = 1024$ ions were consistent

with the earlier results from Gromacs 4.5.4 with $N = 432$ ions for all salts.

We used the final configurations from the hysteresis simulations to create a supercell for the two-phase simulations at each temperature between T_- and T_+. The liquid configurations were cropped in two directions to match the dimensions of the simulation cell of the solid, and excess ions were removed as necessary to preserve electroneutrality. A small space (equivalent to σ_+) was left at each *s*-*l* interface. The configurational energies were minimized to remove poor interactions across the new interfaces, and the system was re-equilibrated in the NVT ensemble for 0.25 ns before running under NPT conditions for 4.0 ns. A run length of 4.0 ns was sufficient for most systems to evolve into a single solid or liquid phase. Periodic boundary conditions were also used for the two-phase simulations.

One issue with using the NPT ensemble for determining the melting point, and particularly for the two-phase simulations, is that the specific temperature of the phase boundary proved to be somewhat sensitive to the barostat parameters, and could vary by as much as ±200 K. The barostat sensitivity has been noted previously for water simulations[107] and was minimized by using larger system sizes. The results given here for the two-phase simulations were obtained employing an anisotropic Parrinello-Rahman barostat[103,104] with a relaxation time of 50.0 ps and a compressibility of 3.0×10^{-5} bar^{-1} along the three primary axes and 0 otherwise. The slower relaxation time of the barostat dampens volume fluctuations allowing the two-phase system to evolve more smoothly into a single phase. The two-phase simulations provide smoother melting point trends, but due to the barostat sensitivity, do not improve the absolute accuracy of the melting point. However, importantly, melting point trends across the model salts were consistent, regardless of the barostat settings.

We emphasize that all three temperatures from the hysteresis method (T_-, T_+, and T_m) as well as T_s and T_l from the two-phase simulations give similar melting point trends, so we would expect the same trends to apply to the thermodynamic melting temperatures as well.

All of the results presented in this thesis are from Gromacs simulations. I wrote a molecular dynamics (MD) program for this project, but chose to use the Gromacs package for the MD simulations for efficiency and convenience. Details of the configuration representations and evaluation are given in Appendix A. A brief overview of how molecular dynamics works is given in Appendix B.

2.10 Crystal Structures

Experimentally, some ionic liquids exhibit polymorphism, where the substance can crystallize into multiple crystal structures.[84,108] Some of the simple model salts considered in this work also exhibit polymorphism, and the melting temperatures (at $P = 1$ bar) of the different crystals can vary by hundreds of degrees.

We are interested in which crystal structures are stable near the melting transition. When T_s is different for different crystal structures of the same salt, we assume that the crystal structure with the highest T_s is the most stable at temperatures near the melting point. This assumption is reasonable near the melting points because the isotropic liquid is an accessible, equilibrium reference state for both solids, one of which is more stable than the liquid, the other which is less stable. Comparing the solids using the liquid as a reference state makes sense at temperatures near the normal melting point. However, this comparison does not allow us to make any statements about which structures are thermodynamically

stable at lower temperatures because the temperature dependence of the chemical potential is different for each crystal structure. It is also impossible to discern the more stable structure if the polymorphs have the same T_s with our grid spacing of 50 K.

The different polymorphs we observe near the melting point are usually distinguished by the degree of orientational order/rotational motion. In the models we are considering, we do see salts that likely undergo a *s*-*s* transition upon heating from a highly orientationally ordered solid to an orientationally disordered solid before melting, provided the pathway barriers (both potential and kinetic) are not prohibitive.

With the exception of the references to the actual NaCl and CsCl salts on Page 1, references to CsCl and NaCl are to the archetypal crystal structure. For simplicity, we refer to interpenetrating simple cubic lattices of cations and anions as "CsCl" solids. Similar definitions (with the appropriate ion lattices) are also used for "NaCl" solids, "NiAs" solids, and "wurtzite" solids. The archetypal crystal structures are for monoatomic ions. When the multi-site cations studied in this thesis are in the arrangement prescribed by the archetypal crystal structure, the cations may be orientationally ordered or disordered.

Chapter 3

How Distributed Charge Reduces the Melting Points of Model Ionic Salts *

3.1 Overview

In this chapter, we focus on how cation charge distribution reduces the melting points of simple model salts composed of size-symmetric, spherical, monovalent ions. We vary the cation geometries with up to one off-center charge site (2L or 1C geometry). The anions in this chapter have a single interaction site (1C geometry). The redistribution of charge away from the cation center can reduce the melting point by up to 50% compared with the charge-centered case. Our results demonstrate how charge distribution can reduce the melting point of molecular ionic solids to temperatures well below those of typical of inorganic salts. The model salts can be viewed as an interesting step away from inorganic molten salts, toward molecular ionic liquids.

*A version of this chapter has been published. E. K. Lindenberg and G. N. Patey, "How distributed charge reduces the melting points of model ionic salts," J. Chem. Phys. **140**, 104504 (2014).

3.2 Melting Point Results

The 1C - 1C Salt

It is convenient to begin with the 1C - 1C salt, which serves as a reference system from which to measure the influence of charge distribution. The 1C - 1C salt persists as a supercooled liquid at 1050 K (T_-) and solidifies at 1000 K. The freezing transformation is signalled by a sudden drop in the average configurational (potential) energy, $\bar{U}$, shown in Fig. 3.1. The crystalline solid persists at 1400 K (T_+). The melting of the superheated solid is signalled by a sudden increase in the average configurational energy between 1400 and 1450 K.

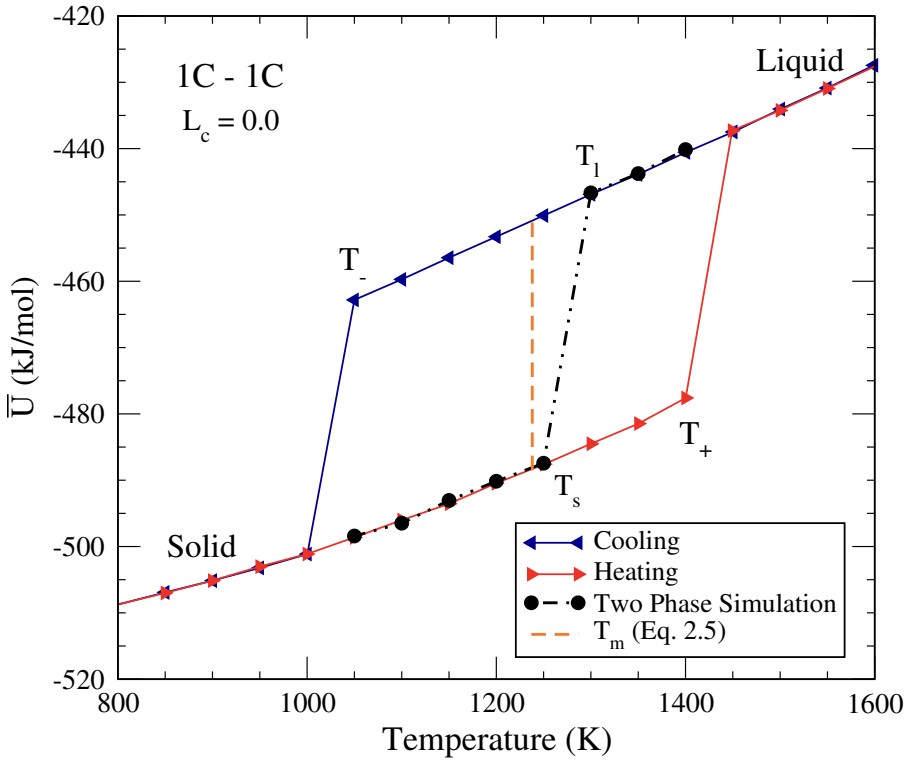

Figure 3.1: The average configurational energies from cooling and heating of the 1C - 1C salt. The supercooled liquid freezes between 1050 K and 1000 K, and the superheated solid melts between 1400 K and 1450 K. The estimated melting temperature is 1238 K using Eq. (2.5), and between 1250 K and 1300 K using two-phase simulations.

The melting temperature of the 1C - 1C salt is 1238 K, as estimated by Eq. (2.5), and the two-phase simulation result agrees with this estimate. At 1250 K (T_s), the two-phase system evolves into a solid and at 1300 K (T_l), the system evolves into a liquid. The stable crystal structure for the size-symmetric 1C - 1C salt is a CsCl crystal, which is predicted by both the phase diagram of the RPM[109] and the radius ratio rules. In the RPM, the fluid and CsCl crystal coexist at $T^* = kT\epsilon\sigma/q^2 = 0.0227$ and $P^* = P\epsilon\sigma^4/q^2 = 0$, where ϵ is the dielectric constant of the medium, σ is the hard sphere diameter, q is the ion charge divided by $\sqrt{4\pi\epsilon_0}$, and k is the Boltzmann constant.[109] For our model parameters (taking $\sigma = 0.50$ nm and $\epsilon = 1.0$), the RPM solid-liquid (s-l) transition temperature would be 759 K at $P = 0$ bar. For a pure LJ system with our model parameters, the s-l transition would be near 310 K.[110] The 1C - 1C salt has a higher melting temperature than both the corresponding RPM and pure LJ systems, as one would expect.

The 2L - 1C Salts

With the s-l phase behaviour of the 1C - 1C salt established as a reference case, we turn to the 2L - 1C set of salts. Relevant simulation results for the 1C - 1C salt are included in our discussion of trends across salt models (Table 3.1). Average configurational energy hysteresis loops for a selection of 2L - 1C salts are shown in Fig. 3.2. We discuss the group of salts that show hysteresis and clear phase transitions, as in Fig. 3.2(a-g), before addressing the salts that lack obvious signs of a first-order transition, as in Fig. 3.2(h).

Nearly seventy-five percent of the 2L - 1C salts considered in this chapter show freezing and melting transitions within hysteresis loops. Specifically, all of the salts with the 2L33 and 2L50 cations, the 2L67 cations with $d \leq 18$, and the 2L100

cations with $d \leq 10$ exhibit distinct *s-l* phase transitions. These salts crystallize spontaneously as CsCl solids with the cation and anion centers occupying the Cs^+ and Cl^- sites, respectively. The off-center charges on the cations do not occupy lattice sites. For the salts with relatively small charge arms, the off-center charge sites are essentially in free rotation around the cation center, and the crystal is orientationally disordered.[111,112] For salts with larger charge arms, the rotational motion is hindered. We return to this point in the discussion of reorientational dynamics below.

The melting point trends are easily identified by comparing T_+ or T_- in Fig. 3.2(a-g). The *s-l* transition shifts to lower temperatures within each column of Fig. 3.2 (constant d) and each row (constant fc), indicating that both model parameters influence the melting temperature.

In Fig. 3.2, the vertical distance between the two phases at the melting temperature corresponds approximately to $\Delta_{\text{fus}}\bar{U}$, which decreases significantly as the charge arm increases. The average configurational energies of the solids are consistently near -525 kJ/mol at 450 K. It is the average configurational energies of the liquids that decrease.

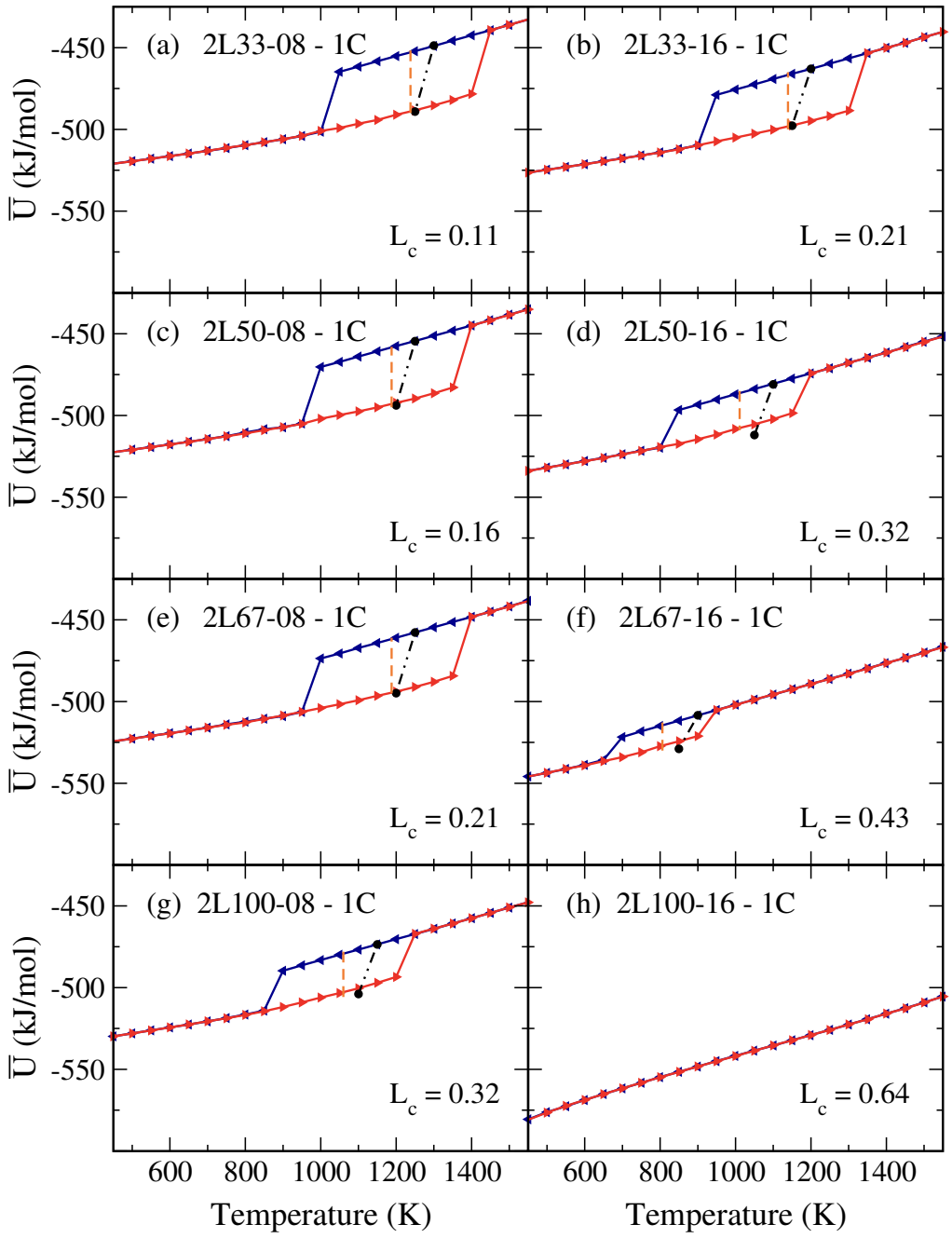

Figure 3.2: The hysteresis loops of the 2L - 1C salts with $d = 08$ and $d = 16$ show that increasing the charge arm decreases the melting point. Increasing either model parameter shifts the *s-l* transition to lower temperatures. The 2L100-16 - 1C salt does not show any hysteresis in panel (h). This salt becomes trapped in a glassy state with a glass transition temperature, as defined in the text, of 400 K. The legend is the same as Fig. 3.1.

Table 3.1 contains numerical results for the model ILs that crystallize spontaneously. We report the melting temperature calculated from Eq. (2.5), T_m, rounded to the nearest simulation temperature. The T_m values decrease with increasing charge arm, and range from 1250 K to 700 K. The temperature-dependent properties given in the last six columns are reported at T_m.

The average reduced densities $\bar{\rho}^*$ for the solid and liquid states are calculated as $N\sigma^3/\bar{V}$, where N is the number of ions, σ is the LJ length parameter, and $\bar{V}$ is the average simulation cell volume in nm^3. The reduced average densities of the solids do not show much variation from the 1C - 1C value of $\bar{\rho}^*_s = 1.03$ as the charge arm increases and T_m decreases. The liquid phase, however, is more sensitive to changes in charge arm and temperature. The average reduced density of the liquid $\bar{\rho}^*_l$ increases from 0.78 (1C - 1C at 1250 K) to 0.99 (2L67-18 - 1C at 700 K).

The sixth column in Table 3.1 gives $\bar{U}^{\mathrm{IP}}_s/U^{\mathrm{IP}}_{iso}$, which is the ratio of the average configurational energy per ion pair in the solid at T_m to the minimum potential energy of an isolated ion pair. The $\bar{U}^{\mathrm{IP}}_s/U^{\mathrm{IP}}_{iso}$ values are larger than 1.0 for all of the salts in Table 3.1, which is expected because all of the salts crystallize spontaneously. As the charge arm increases, $\bar{U}^{\mathrm{IP}}_s/U^{\mathrm{IP}}_{iso}$ decreases, which indicates that a larger fraction of the crystal energy comes from ion pairing rather than from the packing arrangement.

The values of $\Delta_{\mathrm{fus}}\bar{H}$ are calculated as $\bar{H}_l$ - $\bar{H}_s$ using the single phase simulations from the hysteresis cycles. The enthalpy values of the solids calculated from the hysteresis cycles will be artificially high due to the random orientation of the crystal within the simulation cell and crystal stacking faults. The magnitude of the increase varies from salt to salt. We estimate that the potential energies are increased by up to $\sim$5 kJ/mol compared to a properly oriented crystal. Artificially

high values of $\bar{H}_s$ would lead to underestimations of $\Delta_{\text{fus}}\bar{H}$. However, as with the melting temperature estimates, it is the trends in $\Delta_{\text{fus}}\bar{H}$ across a series of salts that are instructive, not the specific values themselves.

Table 3.1: Properties of the crystallizing 2L - 1C salts near their melting points. The charge arm L_c is included for easy reference. The temperature T_m is calculated from Eq. (2.5) and rounded to the nearest simulation temperature. The quantities in the last six columns are reported at T_m. The average reduced number densities $\bar{\rho}^*$ of the liquids show a more pronounced increase than the solids as the charge arm increases. The ratio of average configurational energies per ion pair in the solid to the potential energy of an isolated ion pair, $\bar{U}_s^{\text{IP}}/U_{iso}^{\text{IP}}$, and enthalpies of fusion, $\Delta_{\text{fus}}\bar{H}$ (kJ/mol ion pairs), both decrease as the charge arm increases. The relative contributions of the Lennard-Jones (LJ) and electrostatic (ES) energies to $\Delta_{\text{fus}}\bar{H}$ are given in the last two columns as percentages.

Cation	L_c	T_m	$\bar{\rho}^*(s)$	$\bar{\rho}^*(l)$	$\bar{U}_s^{\text{IP}}/U_{iso}^{\text{IP}}$	$\Delta_{\text{fus}}\bar{H}$	$\Delta_{\text{fus}}\bar{H}$	
	—	(K)	—	—	—	(kJ/mol)	%LJ	%ES
1C	0.00	1250	1.03	0.78	1.70	38	40	60
2L33-06	0.08	1250	1.03	0.78	1.62	37	40	60
2L33-08	0.11	1250	1.03	0.79	1.58	36	40	59
2L33-10	0.13	1200	1.00	0.80	1.55	31	41	58
2L33-12	0.16	1200	0.96	0.81	1.50	25	41	59
2L33-14	0.19	1150	1.01	0.83	1.49	28	44	56
2L33-16	0.21	1150	1.05	0.83	1.46	32	46	54
2L33-18	0.24	1100	0.99	0.84	1.40	21	48	52
2L33-20	0.27	1050	1.03	0.86	1.37	23	52	47
2L33-22	0.29	1050	1.05	0.86	1.33	25	57	42
2L33-24	0.32	900	1.05	0.90	1.30	19	65	35
2L50-06	0.12	1150	0.99	0.82	1.58	28	42	58
2L50-08	0.16	1200	1.04	0.80	1.59	35	42	58
2L50-10	0.20	1150	1.01	0.83	1.50	29	44	56
2L50-12	0.24	1150	1.04	0.83	1.46	31	46	54

Continued on next page...

Table 3.1: (Continued)

Cation	L_c	T_m	$\bar{\rho}^*(s)$	$\bar{\rho}^*(l)$	$\bar{U}_s^{\mathrm{IP}}/U_{iso}^{\mathrm{IP}}$	$\Delta_{\mathrm{fus}}\bar{H}$	$\Delta_{\mathrm{fus}}\bar{H}$	
	—	(K)	—	—	—	(kJ/mol)	%LJ	%ES
2L50-14	0.28	1150	1.08	0.83	1.43	34	49	51
2L50-16	0.32	1000	1.04	0.88	1.37	21	55	45
2L50-18	0.36	900	1.03	0.92	1.33	16	62	38
2L50-20	0.40	850	1.06	0.93	1.29	16	65	35
2L50-22	0.44	800	1.05	0.93	1.26	15	64	36
2L50-24	0.48	750	1.05	0.93	1.22	15	64	36
2L67-06	0.16	1250	1.07	0.79	1.56	41	42	58
2L67-08	0.21	1200	1.03	0.81	1.50	33	43	57
2L67-10	0.27	1150	1.04	0.83	1.45	30	46	54
2L67-12	0.32	1000	1.04	0.89	1.41	22	53	47
2L67-14	0.37	950	1.05	0.90	1.36	19	58	41
2L67-16	0.43	800	1.05	0.96	1.32	12	68	31
2L67-18	0.48	700	1.11	0.99	1.29	13	70	30
2L67-20	0.53	700	1.10	0.97	1.24	15	66	34
2L100-06	0.24	1100	1.03	0.85	1.49	27	45	55
2L100-08	0.32	1050	1.03	0.87	1.43	23	50	50
2L100-10	0.40	1000	1.11	0.89	1.39	26	58	42

From the values in Table 3.1, we see that increasing the charge arm reduces both the melting point and $\Delta_{\mathrm{fus}}\bar{H}$. The breakdown of the LJ and electrostatic contributions to $\Delta_{\mathrm{fus}}\bar{H}$ are given in the last two columns of Table 3.1. For the 1C - 1C salt, the LJ and electrostatic contributions to $\Delta_{\mathrm{fus}}\bar{H}$ are 40% and 60%, respectively. The stabilization provided by the LJ energy is one of the thermodynamic driving forces for crystallization, even though it accounts for only ∼6% of the average po-

tential energy of the 1C - 1C salt in the CsCl solid. As the charge arm increases, the relative contribution of the LJ interactions to $\Delta_{\text{fus}}\bar{H}$ increases, although $\Delta_{\text{fus}}\bar{H}$ decreases in magnitude. The 2L67-18 - 1C salt has a $\Delta_{\text{fus}}\bar{H} = 13$ kJ/mol, with 70% coming from LJ interactions and 30% from electrostatics. The marked decrease in the electrostatic contribution to $\Delta_{\text{fus}}\bar{H}$ suggests that the configurations in the liquid are comparable, at least in terms of electrostatic energies, to those in the CsCl solid.

The LJ contribution to $\Delta_{\text{fus}}\bar{H}$ also decreases in magnitude as the charge arm increases, but it contributes an increasing percentage of the $\Delta_{\text{fus}}\bar{H}$ value. The 2L67-16 - 1C salt has the lowest $\Delta_{\text{fus}}\bar{H}$ of the spontaneously crystallizing salts with a value of 12 kJ/mol, with 8 kJ/mol from LJ interactions and 4 kJ/mol from electrostatic interactions. For this salt, the ion pair energy is about 75% of the average configurational energy per ion pair in the solid. The majority of the configurational energy difference between the CsCl solid and the liquid for the salts with large charge arms can be attributed to the difference in LJ interactions.

The LJ potential energies in the CsCl solids increase (become less negative) with increasing d and, in the case of the 2L50-24 cation, become positive. The strong electrostatic interaction causes the ions to "penetrate" the repulsive LJ sphere and create bound ion pairs that exist in both the solid and liquid phases. The ion pairs are bound tightly and each ion sphere is deformed (flattened) on one side.

The values of both $\bar{U}_s^{\text{IP}}/U_{iso}^{\text{IP}}$ and $\Delta_{\text{fus}}\bar{H}$ decrease as the charge arm increases. Both quantities measure the relative stability of the solid, the former with respect to a collection of isolated ion pairs, and the latter with respect to the liquid phase. As the charge arm increases, the salts clearly have less thermodynamic incentive to crystallize.

The molar entropy of fusion ($\Delta_{\text{fus}}S = \Delta_{\text{fus}}\bar{H}/T_m$) can be estimated from

the $\Delta_{\text{fus}}\bar{H}$ and T_m values given in Table 3.1. For the systems included in Table 3.1, $\Delta_{\text{fus}}S$ also decreases with increasing charge arm, indicating that there is less entropic gain associated the *s*-*l* transition. In isolation, the reduction of $\Delta_{\text{fus}}S$ would usually increase melting temperatures, however, the fractional change in the entropy of fusion with respect to the 1C - 1C system is less than that for $\Delta_{\text{fus}}\bar{H}$, consistent with the reduced melting points observed.

We have discussed the enthalpies of fusion at length in this section, which depend on both the charge arm and the melting temperature. We will revisit the enthalpic properties of the salts again in Chapter 3.4 when we examine the enthalpies at set temperatures in both the solid and liquid phases.

The "Glassy" 2L - 1C Salts

We now discuss the 2L - 1C salts that do not crystallize spontaneously when cooled, at least not on time scales currently convenient for simulation. Instead, they become trapped in "glassy" states. Because glass formation can depend on the cooling rate, all of the salts that formed glasses when cooled in 50 K increments (ten in total), were again cooled in 25 K increments. Only one of the ten salts (2L67-20 - 1C) crystallized at the slower cooling rate, and can be regarded as lying at the boundary between salts that spontaneously crystallize, and those that tend to form glasses. The nine salts that did not spontaneous crystallization include the cations 2L67-22, 2L67-24, and 2L100 with $d \geq 12$. The glass transition temperatures T_g (defined in Chapter 2.7) for these salts occur between 350 and 450 K, which is near the conventional threshold value of 373 K that is used to "define" ionic liquids, as opposed to molten salts.

In order to explore possible crystal structures for the glassy salts, and to obtain T_+ values for the melting point estimates, we heated prepared crystal structures from $T = 50$ K. Upon heating, two of the crystals of the 2L100-16 - 1C salt rearranged into a highly orientationally ordered, lower enthalpy structure. The space group of the new crystal is 111 ($P_{\bar{4}2m}$), as identified using the FINDSYM[113] program. We refer to this crystal structure as 111_n, following the labelling convention used by Filion and Dijkstra[114] of giving the space group and occupied Wyckoff position(s).

The 111_n crystal structure, shown in Fig. 3.3, has a tetragonal unit cell with two equal axes and one longer axis. There are staggered columns of ion pairs parallel to the long axis of the unit cell. The orientations of the cations are the same within each column, and alternate from column to column. Perpendicular to the columns, the crystal structure has alternating layers of electrostatic- and LJ-dominated interactions. The view in the $[\bar{1}\bar{1}0]$ direction, shown in Fig. 3.3(b), depicts the staggering of adjacent columns and highlights the electrostatic-dominated layers (red and white) and the LJ-dominated layers (blue). The 111_n crystal structure resembles the layered crystal structures used in intercalation studies and potential superconductors.[115,116] The crystal plane shown in Fig. 3.3(b) bears a resemblance to iron oxychloride (FeOCl, space group 59, P_{mmn}), where the Fe, Cl and O positions are occupied by the cation off-center charge site, cation center, and anion center, respectively.[117] The differences between the two crystal structures are visible in the other crystal planes.

The enthalpy of the 111_n crystal is lower than that of the CsCl crystal for all glassy salts. Upon heating, the 111_n structure did not rearrange to another crystal structure, or show any reorientational relaxation prior to melting, for any of the glassy salts. The orientationally disordered CsCl (OD-CsCl) and 111_n structures

are two potential crystal arrangements for our glassy salts near their melting temperatures. Our simulations do not indicate which is the more stable crystal. The OD-CsCl structure is perhaps partially stabilized by the reorientational entropy of the cation, whereas the 111_n structure is stabilized by a lower configurational energy.

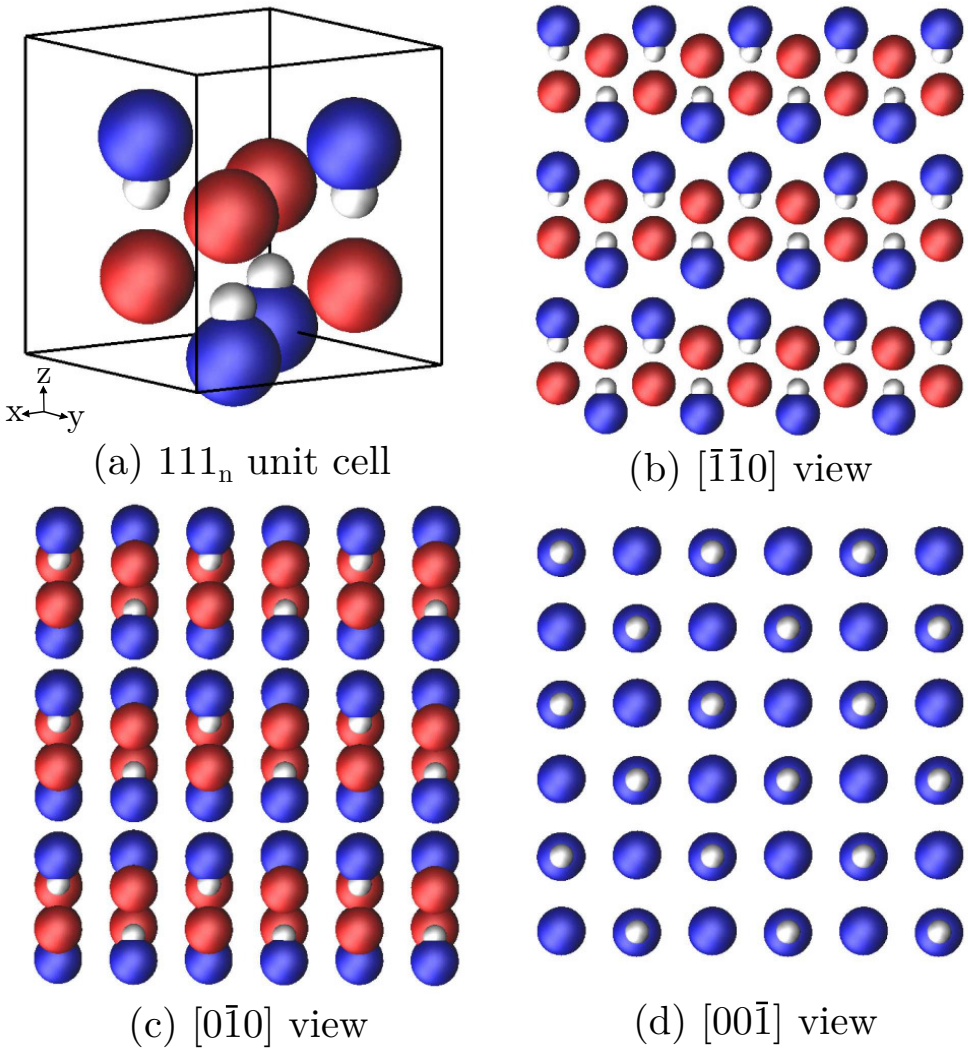

Figure 3.3: The 111_n crystal structure shown for the 2L100-16 - 1C salt. The crystal space group is 111 ($P_{\bar{4}2m}$). The cation centers, cation off-center charge sites, and anion centers are shown in blue, white, and red, respectively. The ions are not shown to scale; the off-center charge sites on the cations are embedded within the cation volume. In (d), the top layer of anions is not shown to highlight the alternating orientations of the cations.

The 2L67-20 - 1C salt lies between the salts that crystallize in a CsCl structure and the salts that vitrify. The salt crystallized during the heating part of the hysteresis loop, shown in Fig. 3.4. We cooled the liquid at a slower rate (25 K increments) and the 2L67-20 - 1C salt does crystallize into a CsCl structure. The 2L67-20 - 1C salt was the only glassy salt that crystallized at the slower cooling rate. For the CsCl solid, we take T_{-} as 550 K, rather than using the glass transition temperature of 400 K. For the 111_n solid, we use the glass transition temperature as T_{-}. Both superheated crystals melt at 900 K.

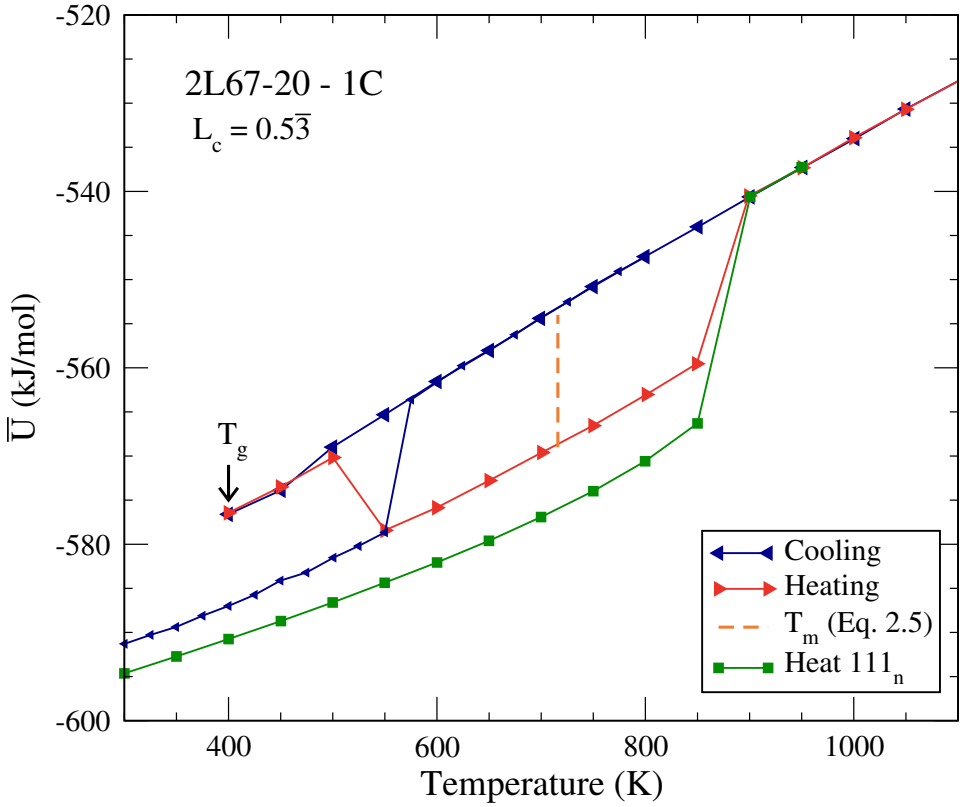

Figure 3.4: Hysteresis loops for the 2L67-20 - 1C salt. The salt freezes into a glassy state when cooled in 50 K increments, but crystallizes into a CsCl structure when it is cooled at a slower rate (25 K increments). The green squares mark the heating of the 2L67-20 - 1C salt in the 111_n crystal structure. The 111_n structure is highly orientationally ordered and the cations do not show significant reorientational relaxation until the salt melts.

The configurational energies as a function of temperature for the 2L100-16 - 1C salt are shown in Fig. 3.5, as a representative example of the glassy salts. The cooling and heating traces of the liquid/glassy systems nearly coincide. When heating the prepared crystal structures, the solids rearrange into one of two crystal structures before melting. The NiAs crystal (not shown) rearranges into the OD-CsCl structure when heated. The OD-CsCl crystal persists between 650 K and 800 K, and liquefies at 850 K. The wurtzite and NaCl structures rearrange into the 111_n structure when heated. The 111_n crystal melts at 1050 K.

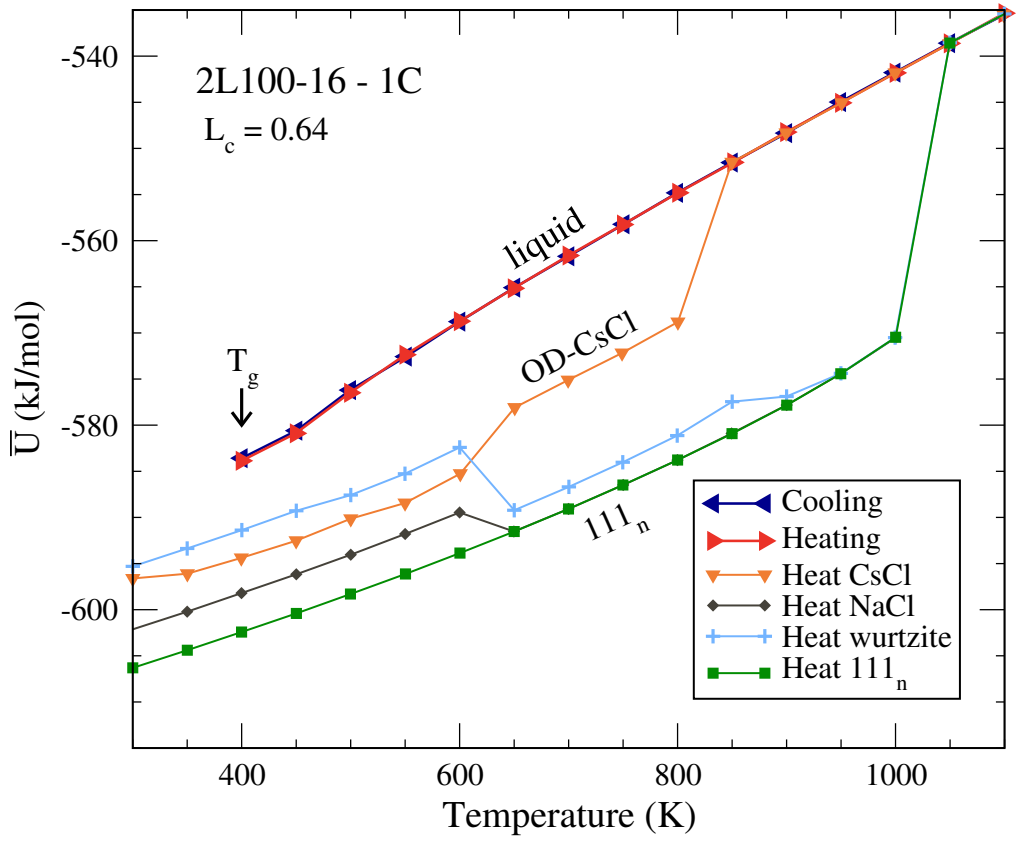

Figure 3.5: The average configurational energy hysteresis loop for the 2L100-16 - 1C salt. When cooling from the liquid state, this salt becomes trapped in a glassy state. The crystal structures heated from $T = 50$ K rearrange into an orientationally ordered 111_n structure or into an orientationally disordered CsCl crystal before melting.

(a) Liquid

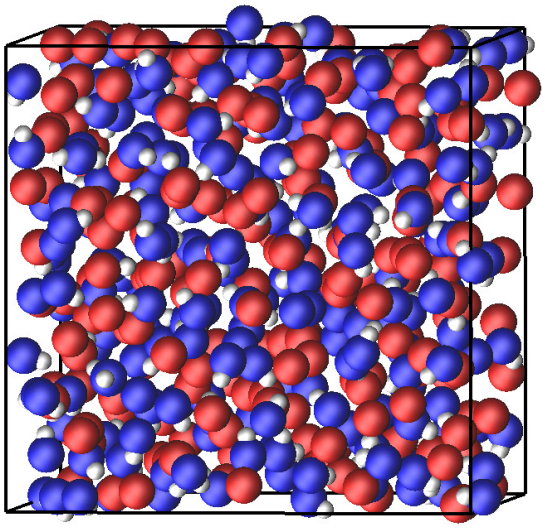

(b) OD-CsCl

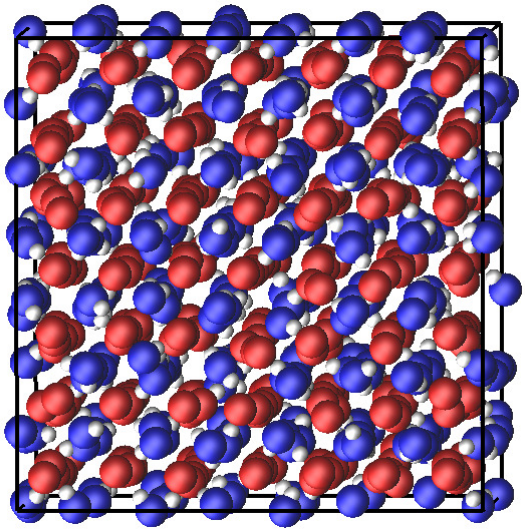

(c) 111_n

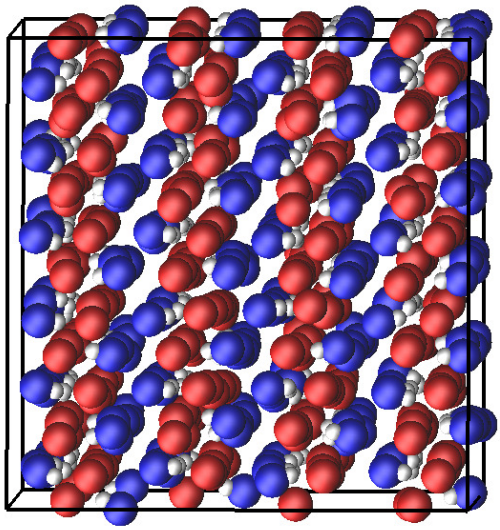

Figure 3.6: Configurational snapshots of the 2L100-16 - 1C salt in three different phases at $T = 700$ K. From the two-phase simulations, T_s for the 111_n structure of this salt is 800 K. The cation centers, cation off-center charge sites, and anion centers are shown in blue, white, and red, respectively. The ions are not shown to scale; the off-center charge sites on the cations are embedded within the cation volume.

Configurational snapshots of the 2L100-16 - 1C salt at T = 700 K are shown in Fig. 3.6. The three phases included (T = 700 K) are the supercooled liquid, the OD-CsCl solid, and the 111_n solid. The two-phase simulations with the 111_n crystal give T_s = 800 K for this salt. The simulation cells are not shown to scale. The number of particles in each simulation varies (liquid N = 432, CsCl N = 686, 111_n N = 576).

Table 3.2 contains the melting temperatures [from Eq. (2.5)] for both the CsCl and 111_n structures, and the reduced densities for the 2L - 1C glassy salts. As in Table 3.1, T_m is rounded to the nearest simulation temperature. The reduced densities are reported at the T_m of the 111_n structure. The temperature range in the table is only 250 K, so the variations values for the CsCl crystals continue the trends from Table 3.1, with T_m generally decreasing with increasing L_c. For the 2L100 - 1C series, the T_m values of the 111_n structure peak between $d = 14$ and 20 and are higher than the corresponding CsCl estimates.

In two-phase simulations including the 111_n crystal and liquid, the crystal was placed with the (110) plane facing the liquid. The crystal phase was able to grow and, at certain temperatures, the entire liquid phase crystallized. The lowest value of T_s obtained from our set of model salts was 600 K for 2L100-20 - 1C. The 2L100 - 1C salts with $d = 22$ and 24 were exceptions in that two-phase simulations did not result in freezing, even at 400 K. It is possible that these two salts have a different underlying crystal structure. In any case, for discussion purposes we take T_s to be 400 K for these salts.

Table 3.2: Properties of the 2L - 1C salts that vitrified. The values of T_m are given for both CsCl and 111_n solids. The reduced average densities are reported at T_m of the 111_n solid.

Cation	L_c	T_m CsCl (K)	T_m 111_n (K)	$\bar{\rho}^*$ (111_n)	(l)
2L67-20	0.53	700	650	1.084	0.991
2L67-22	0.59	650	650	1.079	0.967
2L67-24	0.64	650	650	1.064	0.946
2L100-12	0.48	900	700	1.073	1.007
2L100-14	0.56	750	750	1.093	0.986
2L100-16	0.64	650	750	1.114	0.977
2L100-18	0.72	600	750	1.117	0.952
2L100-20	0.80	650	750	1.097	0.912
2L100-22	0.88	600	650	1.088	0.933
2L100-24	0.96	—	500	1.108	0.998

3.3 Melting Point Trends

Our simulations give five transition-related temperatures for each salt: T_-, T_+, T_m from Eq. (2.5), and T_s and T_l as the boundaries of the two-phase simulations; all are presented concisely in Fig. 3.7. All five transition-related temperatures show a general decrease as the cation charge is moved further off-center. Since the qualitative behaviour of all five temperatures is the same, we would expect the general trends to apply as well to the true thermodynamic melting temperatures.

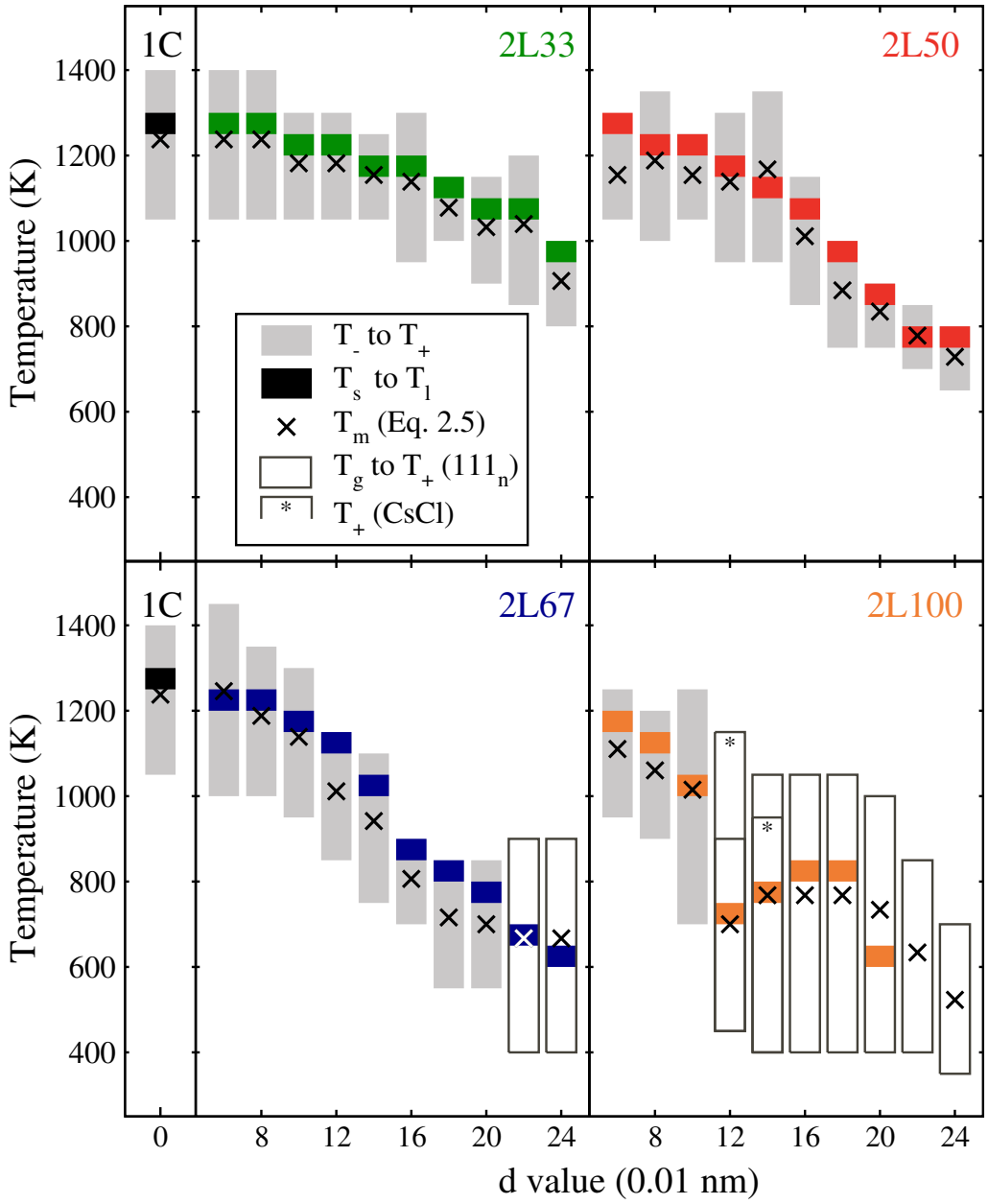

Figure 3.7: Melting temperature summary for the 2L - 1C salts. All five of the transition-related temperatures produce the same trends. The melting point decreases with increasing charge arm with the exception of the 2L100 cations with $d = 12 - 16$. The increase in melting points coincides with the change in crystal structure from CsCl to 111_n. Tabulated values are given in Appendix D in Tables D.1 and D.2.

As discussed in Chapter 2, the two-phase simulations were performed to refine the melting temperature estimates, and here we use T_s to discuss particular trends. In order to highlight the differences in melting points, we scale the T_s value of each salt by T_s of the reference 1C - 1C salt (1250 K).

The plots in Fig. 3.8 show how the melting point changes when one ion model parameter, fc or d, is varied holding the other fixed. In Fig. 3.8, we have plotted only the melting points for the salts that spontaneously crystallize into a CsCl structure. The melting points generally decrease as fc or d increases, but the decrease is not uniform.

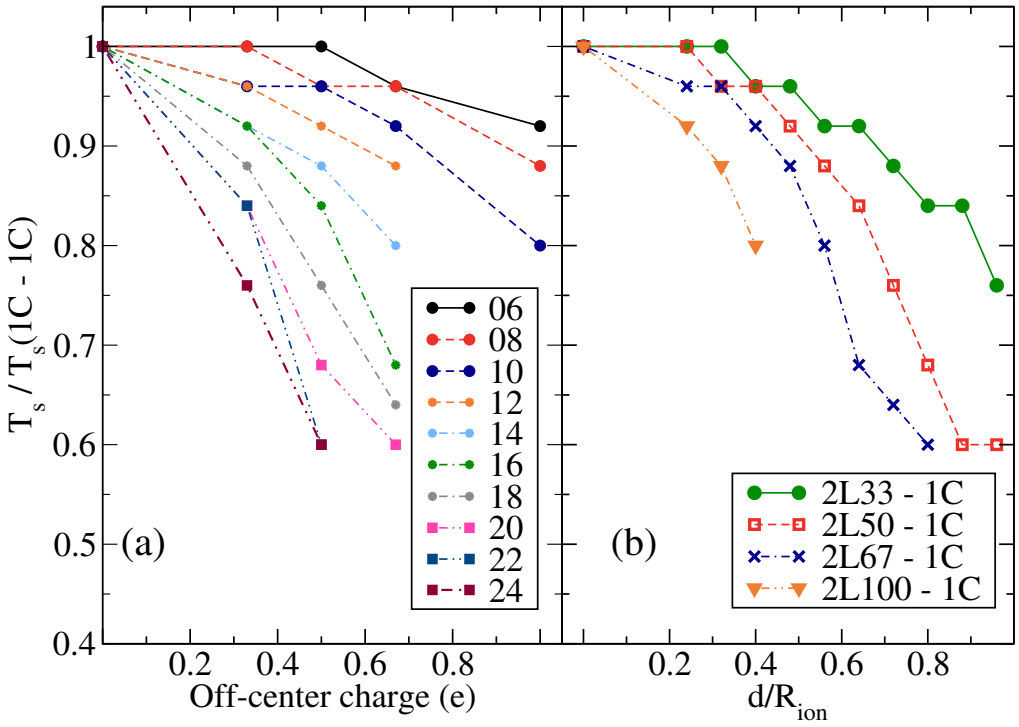

Figure 3.8: The two parameters of the 2L model ions, the amount of charge off-center, fc, and the displacement distance from the ion center, d, both influence the melting temperatures of the 2L - 1C salts.

The main results of this chapter are summarized in Fig. 3.9, where the ratio of T_s/T_s(1C - 1C) is plotted versus the cation charge arm. The influence the charge arm has on melting point is clear; moving some of the unit charge away from the center in an RPM-like salt generally decreases the melting temperature. For the salts near $L_c = 0.50$, where both CsCl and 111_n structures are viable possibilities, we plot the highest T_s value observed for each model salt in Fig. 3.9. Fig. 3.9 represents the minimum reduction in melting point for our model salts.

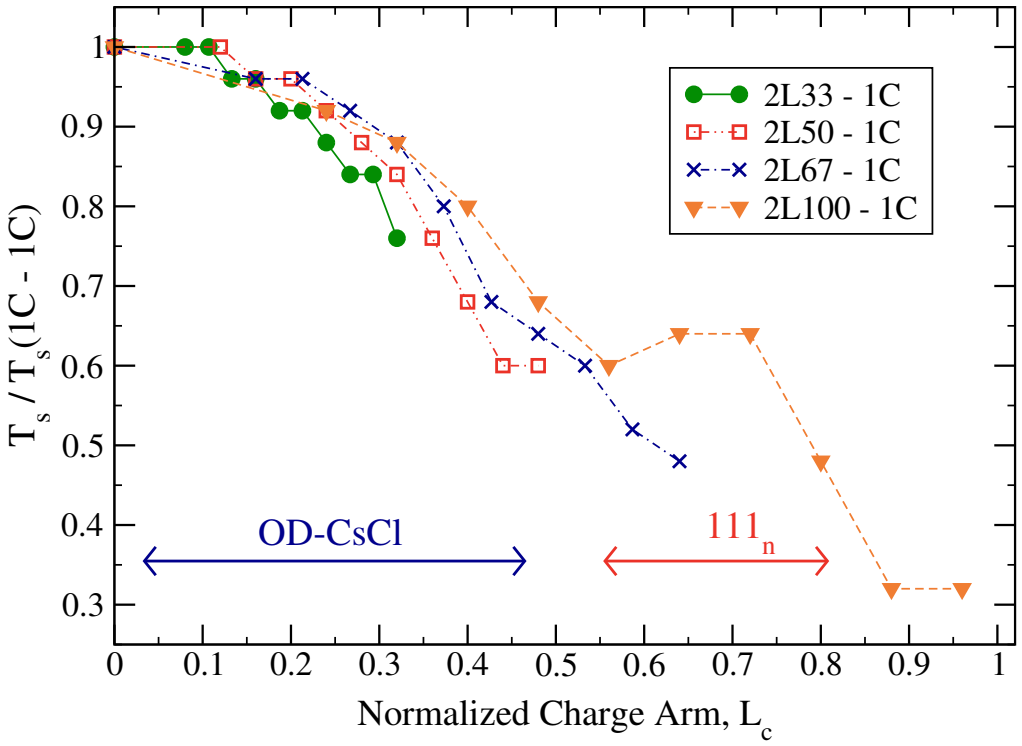

Figure 3.9: The plot of scaled melting temperatures against the normalized charge arm reveals that melting points of CsCl crystals decrease until the value of L_c reaches 0.50. Above $L_c = 0.50$, the 111_n has a lower enthalpy than the CsCl structure. The 111_n melting temperature peaks between $L_c = 0.64$ and 0.72. All of salts with $L_c \geq 0.50$ vitrify; none of these salts spontaneously crystallize into the 111_n structure from the liquid phase on simulation time scales.

The salts with $L_c \leq 0.50$ crystallize in a CsCl structure. For equivalent charge arm values below $L_c = 0.33$, the 2L33 - 1C salts melt at temperatures equal to, or lower than, the other model salts. The 2L33 - 1C salts have a maximum L_c value of 0.33. For $0.33 < L_c \leq 0.50$, the 2L50 - 1C salts are the lowest melting CsCl salts, until the maximum $L_c = 0.50$ is reached. For a given L_c a model cation with a larger d achieves a lower melting point than one with a larger amount of charge off center. This feature may be useful for the rational design of low-melting ILs.

At charge arms between 0.50 and 0.64, we see different trends for the 2L67 - 1C salts and the 2L100 - 1C salts. In this region, the highest melting crystal transitions from CsCl to 111_n. The two model salts in the crossover region are the 2L67-20 - 1C and 2L100-12 - 1C salts. The melting points of the CsCl solid were higher than those of 111_n for both of these salts. As the charge arm increases further, the melting points of the 2L67 - 1C salts continue to decline, despite the change in crystal structure, whereas the melting points of the 2L100 - 1C salts increase. The melting point increase in the 2L100 - 1C salt series occurs between $d = 14$ and 16. At $d = 14$, the ion geometry and the 111_n structure are compatible, but the optimal ion geometry for the 111_n structure occurs at larger charge arms ($d = 16$ to 18). The peak in the melting points lies near 800 K for the 2L100 cations with $0.64 \leq L_c \leq 0.72$. Once the charge arm is above 0.72, the melting points drop again.

We have shown that varying the charge distribution in size-symmetric, spherical, monovalent salts can lower the melting temperature by more than 50%. Upon cooling, the model salts considered here form orientationally disordered crystals or vitrify, two solidification behaviours that have been observed in real IL systems.[48,68,75] In the next section, we analyze thermodynamic, structural, and dynamic properties in both phases to better understand why the melting point decreases with

increasing charge arm.

3.4 2L - 1C Salt Properties

The thermodynamic melting point occurs when the chemical potentials of the solid and the liquid are equal at the same temperature and pressure. Typically, a solid is stabilized by enthalpy and a liquid by entropy. The average enthalpy is easily accessible in MD simulations, and it is the first property we examine. The charge arm alters both the symmetry and strength of the electrostatic interactions, and impacts the average enthalpy in both the solid and liquid phases.

The average enthalpies at $T = 1100$ K, shown in Fig. 3.10, offers insight into one of the main reasons why melting temperatures decrease with increasing charge arm. The horizontal black lines give the average enthalpy of the 1C - 1C salt in the solid phase (solid line) and supercooled liquid phase (dashed line) at $T = 1100$ K. The plot shows how the charge arm affects the average enthalpy of each phase as d increases. The ions with $d = 6$ are on the left side of Fig. 3.10, and the enthalpy values deviate slightly from those of the 1C - 1C reference salt. The enthalpies of the CsCl solids and the supercooled liquids at $d = 6$ are slightly higher (less negative) than the enthalpies of the reference 1C - 1C salt, but the enthalpic gap between phases remains near 40 kJ/mol. As d increases, the average enthalpy decreases for both the supercooled liquid and CsCl solid phases, primarily due to the increasing attractive strength of the electrostatic interaction from the off-center charge site. The rate of decrease is faster for the supercooled liquid, which indicates that the liquid phase benefits more from the charge redistribution than the CsCl solid. For each set of salts, there is a d value where the average enthalpy of the

solid increases. This increase marks where the CsCl solid becomes unstable with respect to the liquid across salt models. To the right of the increase, the salts are molten and the average enthalpies follow the trace of the liquid. At large d values, the average enthalpies of the liquids are significantly lower than those of the CsCl solids. The increase in charge arm stabilizes the liquids more than the CsCl solids, and the melting points shift to lower temperatures.

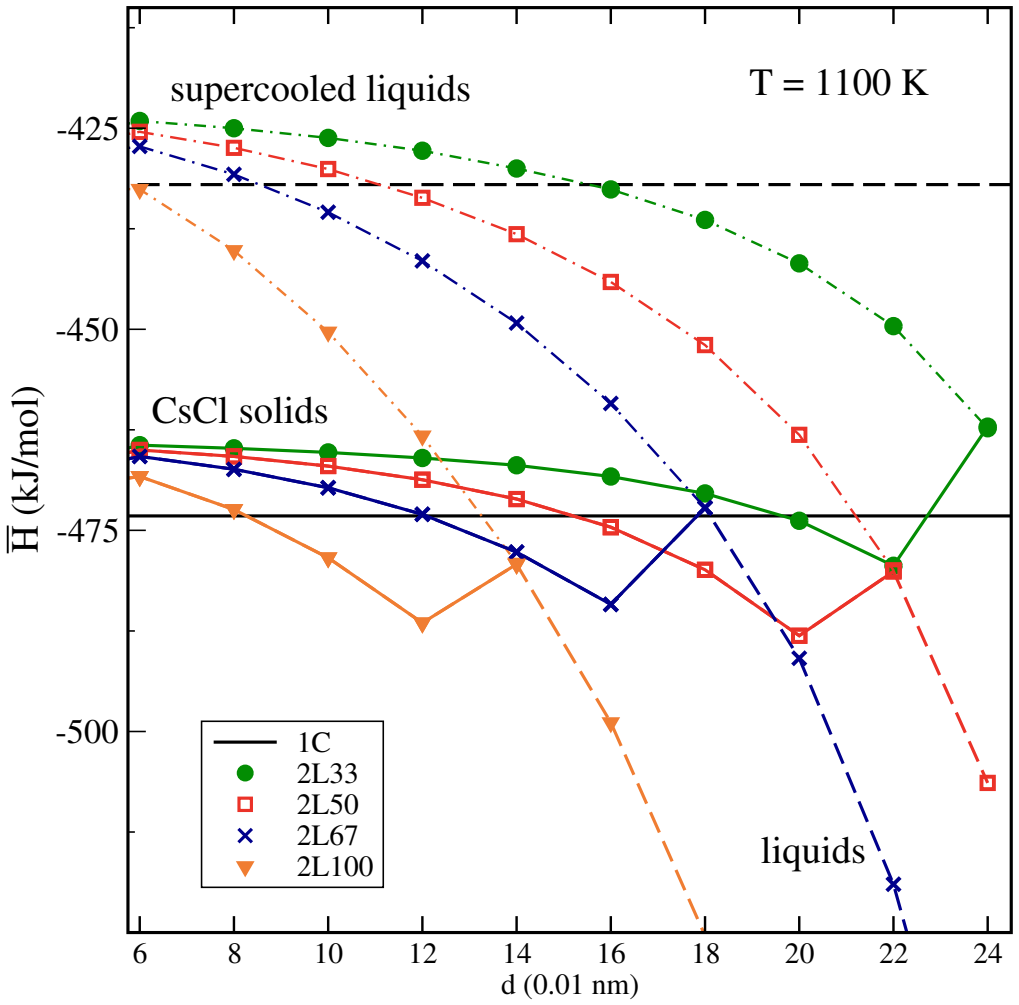

Figure 3.10: The average enthalpies as a function of charge displacement at $T = 1100$ K reveal one of the main reasons the melting points decrease. Moving from left to right, the enthalpies of the supercooled liquids (marked with dot-dash lines) decrease faster than the enthalpies of the solids (marked with solid lines) as the charge arm increases. The single enthalpic increase in each series marks the end of the superheated CsCl phase, and the approximate phase transition at 1100 K. On the right, the 2L50, 2L67, and 2L100 series salts are liquids (marked with dashed lines) that have significantly lower enthalpies than the reference 1C - 1C CsCl solid (solid black line).

A similar plot of the enthalpies at $T = 600$ K, shown in Fig. 3.11, shows that the 111_n structure has a higher enthalpy compared to the CsCl solid for the 2L100-10 - 1C salt, and a lower enthalpy for the 2L100-12 - 1C salt. The crossover between crystal types coincides with the boundary between salts that spontaneously crystallize and those that do not. For 2L67 cations with $d \geq 20$, the 111_n structures have a lower enthalpy than the CsCl structures. The 2L67-20 - 1C salt is on the boundary between the solidification behaviours but does crystallizes spontaneously into an OD-CsCl structure. The enthalpy traces across salt models still show the transition when the liquid becomes more stable than the solid but, in contrast to Fig. 3.10, the transition does not involve a marked increase in enthalpy.

In Fig. 3.10 and Fig. 3.11, the average enthalpies for the solids were calculated using prepared crystals where the orientation of the crystal axes and simulation cell axes are aligned. The axes alignment gives smoother trends for discussion.

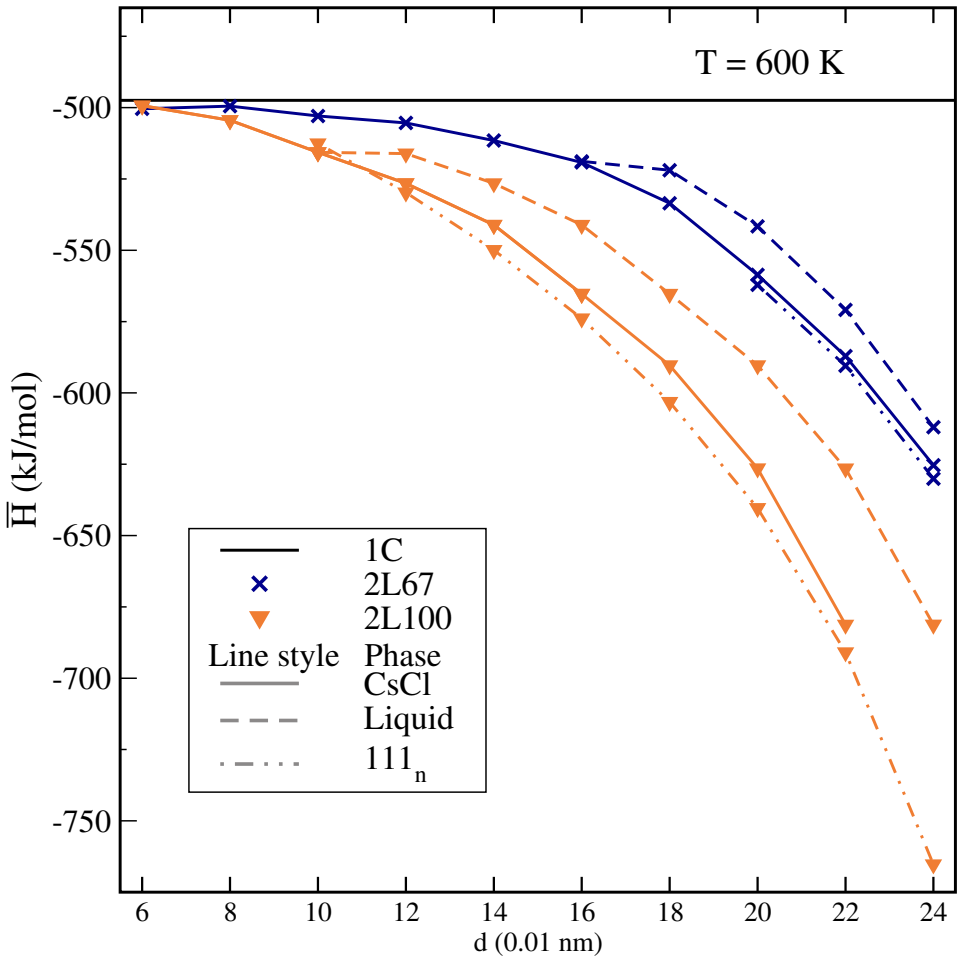

Figure 3.11: Average enthalpies as a function of charge displacement at $T = 600$ K. The line styles denote the phase and the symbol shapes/colours denote the cation type. The solid black line is the enthalpy of the 1C - 1C CsCl solid. The CsCl solids for the 2L - 1C salts are shown as solid lines. For 2L100 cations with $d \geq 12$ and 2L67 cations with $d \geq 18$ the (supercooled) liquid enthalpies are connected with dashed lines. The dot-dash-dot lines connect the enthalpies of the salts in the 111_n structure.

For the remainder of this section, we highlight the changes in structural and dynamical properties by focusing on a subset of the 2L67 - 1C salts. The 2L67 cations have 2/3 of the unit charge located on the off-center site. The 2L67 cations with d = 06, 10, 14, 18, and 22 capture the typical behaviour with respect to changes in charge arm and temperature. It is worth remarking that in real ILs, at low temperatures cations with shorter side chains show qualitatively similar behaviour to cations with longer side chains at higher temperatures.[12] We see qualitatively similar behaviours between salts with small cation charge arms at low temperatures and salts with large cation charge arms at higher temperatures. Both the alkyl chain length and charge arm represent at some level the degree of displacement between the center of charge and the center of mass.

We discuss properties of the salt subset at 500 K and 1100 K. The salts and their phases at T = 500 K and 1100 K are given in Table 3.3.

Table 3.3: The phase behaviour of the 2L67 - 1C salt subset at T = 500 K and 1100 K listed for reference. The dynamic properties of these salts are discussed in the rest of this section.

Temperature	2L67-d - 1C Salt Subset				
(K)	d = 06	10	14	18	22
500	CsCl	CsCl	CsCl	CsCl	slow liquid or 111_n
1100	CsCl	CsCl	liquid	liquid	liquid

The radial distribution functions (rdfs) at T = 500 K are shown in Fig. 3.12. In panels (a-d), the salts are CsCl crystals. In panel (e), the 2L67-22 - 1C salt is a slow liquid nearing its glass transition temperature and shows little long-range order. In panel (f), the 2L67-22 - 1C salt is shown again, but in the 111_n crystal structure. Across the set of rdfs, the changes in structure due to increases in the charge arm are most pronounced in the CC-AM rdf (light blue). In panels (a) and

(b), the first peak in the CC-AM rdf is broad and centered around the first CM-AM peak. The CC sites on the cations are essentially in free rotation around the CM sites. As the charge arm increases, a pronounced shoulder appears on the left of the first CC-AM peak in panel (c), and it develops into a separate peak in panels (d-f). The splitting of the first CC-AM peak indicates that the CC sites on the cations prefer to be directed towards particular anions rather than rotating freely over all orientations. In panel (e), the combined evidence of the position of the first peak in CC-AM, and the similarities in the CM-CM (black) and AM-AM (red) rdfs, suggests that the salts are developing ion pairs. In the 111_n structure shown in panel (f), the short CC-AM separation signals ion pairing, but the differences in CM-CM (black) and AM-AM (red) rdfs indicate a more complicated arrangement than simple ion pairs.

At 1100 K, the solids in Fig. 3.13(a-b) are still CsCl crystals, and the rdf peaks show the expected thermal broadening and shifts to longer distances. The liquids in Fig. 3.13(c-e) have the left shoulder (peak) at shorter separations in the CC-AM rdfs. The 2L67-18 - 1C and 2L67-22 - 1C salts show signs of ion pairing as discussed above. The liquids do not show significant ordering beyond 1 nm. In the liquid phase, the ion pairing reduces the longer range charge ordering that can occur in inorganic molten salts.

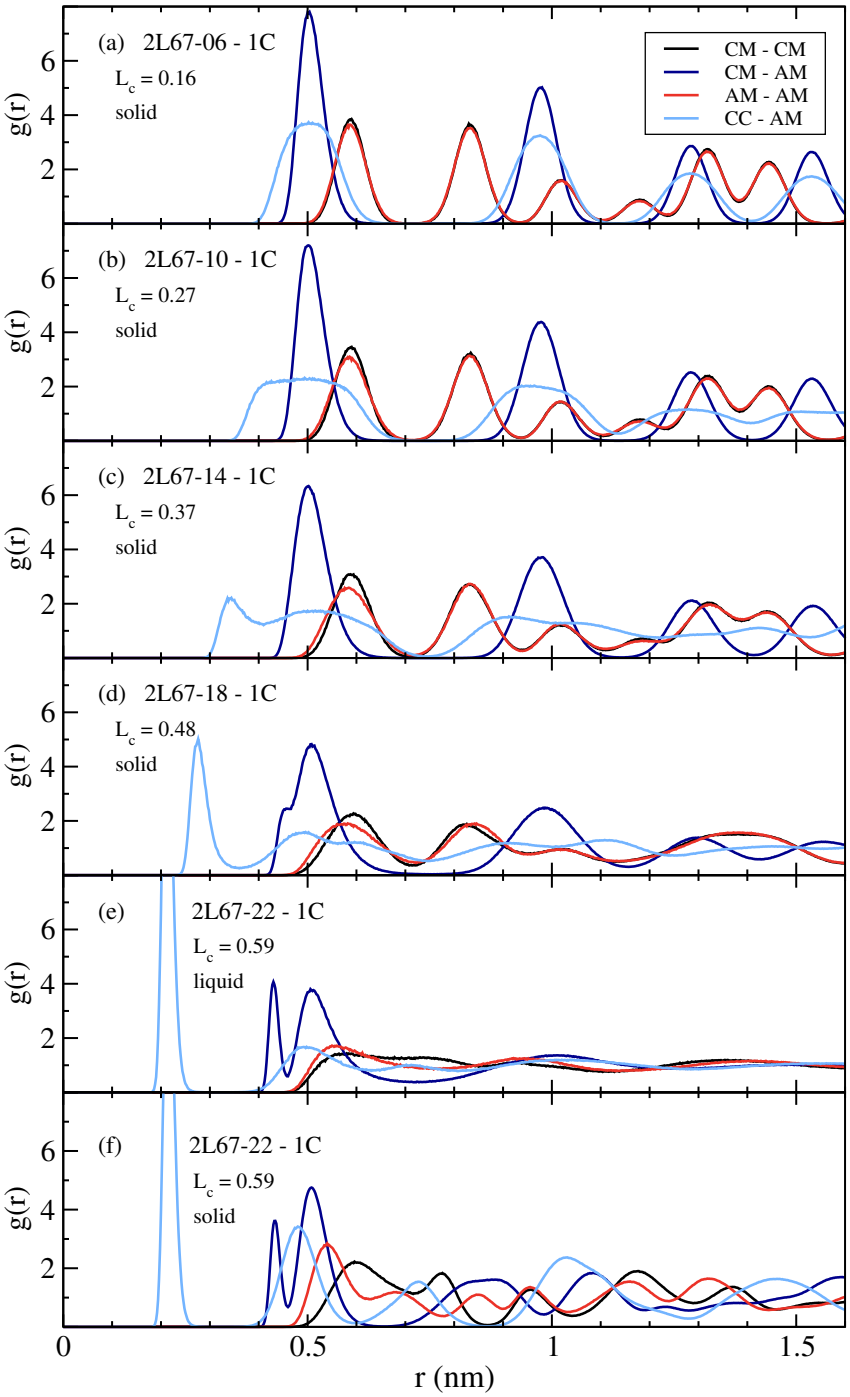

Figure 3.12: Radial distribution functions for selected 2L67 - 1C salts at $T = 500$ K and $P = 1$ bar. The CC-AM rdf (light blue, cation off-center site to anion central site) shows the largest variation as d increases. In panels (a) and (b), the cation is in nearly free rotation, whereas in panels (e) and (f), the cation is part of an ion pair and cannot rotate freely. The solids in panels (a-d) are OD-CsCl structures, and in panel (f) the salt has a 111_n structure.

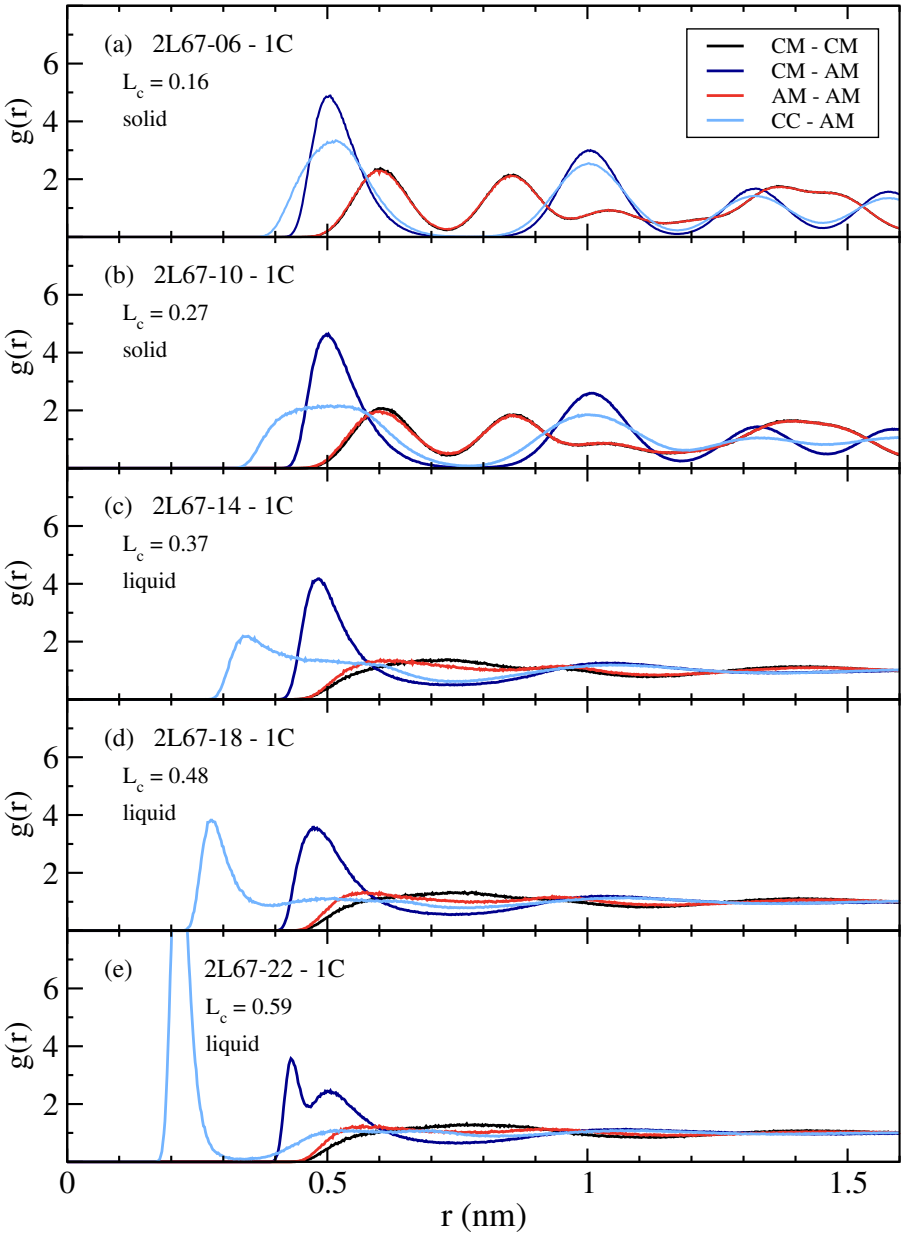

Figure 3.13: Radial distribution functions for selected 2L67 - 1C salts at $T = 1100$ K and $P = 1$ bar. In panels (a) and (b), the salts are OD-CsCl solids, whereas in panels (c-e) the salts are liquids. The liquids show little long-range order. As in Fig. 3.12, as the value of d increases the CC-AM rdf (light blue) shows the largest variation in the shape and location of the first peak.

Ion pairing was observed in earlier studies of the dynamical properties of similar model salts in the liquid phase.[60,61] Further evidence of ion pairing is found in the velocity autocorrelation functions (VACFs). Normalized VACFs are defined in the usual way,[118–120]

$$C_v(t) = \frac{\langle \boldsymbol{v}(t) \cdot \boldsymbol{v}(0) \rangle}{\langle \boldsymbol{v}(0) \cdot \boldsymbol{v}(0) \rangle,} \tag{3.1}$$

where $\boldsymbol{v}(t)$ is the velocity at time t.

In Fig. 3.14, we show VACFs for three of the 2L67 - 1C salts at T = 1100 K; the behavioural trends at 500 K are similar. In Fig. 3.14(a), the 2L67-06 - 1C salt is a CsCl crystal. The negative regions indicate caging effects, which all three interaction sites exhibit. In panel (a), the plots for the ion centers, CM and AM, are distinct, indicating that the ion centers are moving somewhat independently. The VACF of the CC site follows the AM site; the CC and AM sites move nearly in phase with the AM site having a slightly larger amplitude. In panel (b), the VACFs of the CM and AM sites are similar, and the CC VACF has a few oscillations about zero. In panel (c), the CC VACF oscillates about zero and the plots for the ion centers, CM and AM, nearly coincide. For the 2L67-22 - 1C salt, the ions are clearly bound in pairs and are not moving independently. The rapid oscillation in the CC VACF suggests that the ion pair is undergoing librational/vibrational motion. The VACFs in panel (c) provide dynamical evidence of strong ion pairing in the liquid phase.

Further insight into ion-ion correlations and the nature of the solid and liquid phases can be obtained by considering reorientational autocorrelation functions of the cation. For example, if ion pairs are formed we would expect the cations to exhibit longer reorientational correlation times. Reorientational autocorrelation

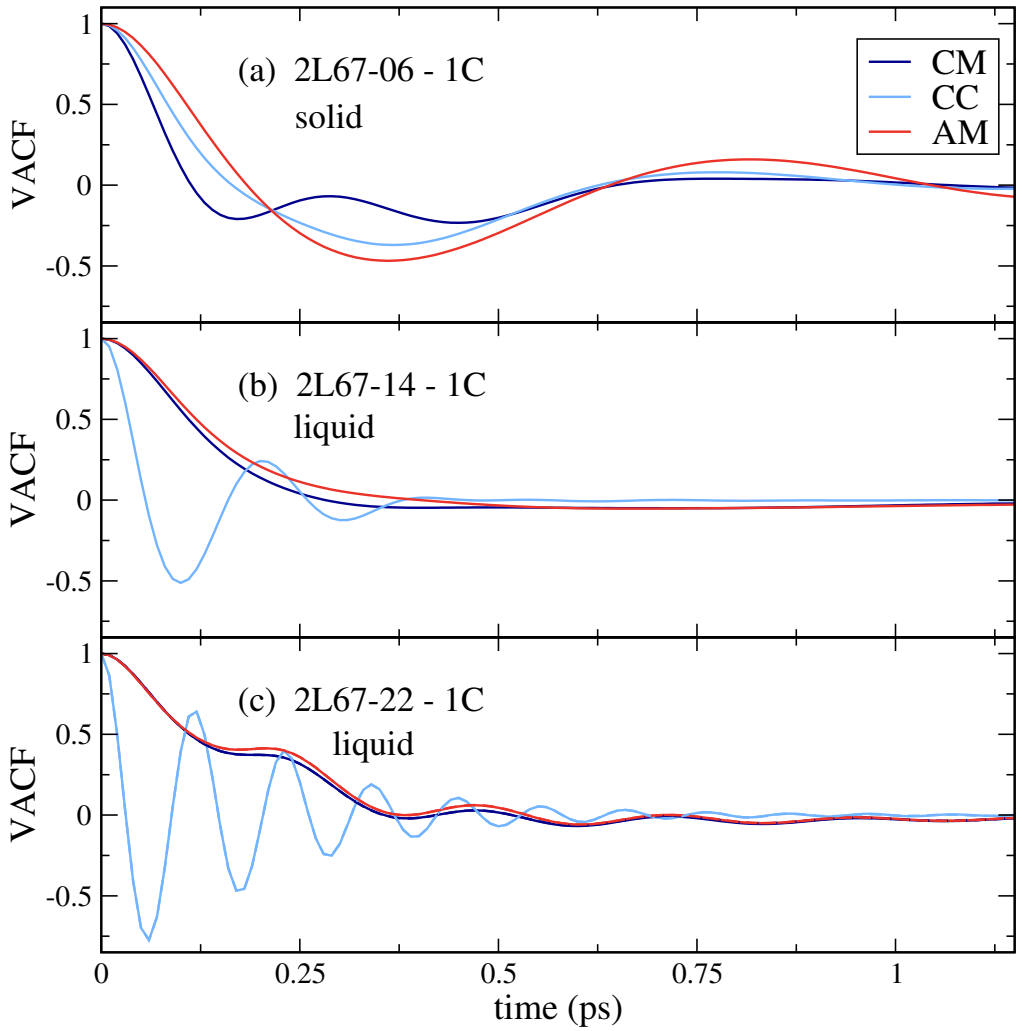

Figure 3.14: VACFs for selected 2L67 - 1C salts at 1100 K. The CsCl solid in panel (a) shows negative regions, indicating ion caging. In panels (b) and (c), the VACFs for the ion centers CM and AM are similar and the CC VACF oscillates about zero. In combination, these two characteristics suggest that ion pairs are formed in the liquid phase.

functions are calculated as[118–120]

$$C_l(t) = \frac{1}{N}\sum_{i=1}^{N}\langle P_l(\boldsymbol{\mu}_i(t)\cdot\boldsymbol{\mu}_i(0))\,\rangle, \tag{3.2}$$

where P_l is the l^{th} rank Legendre polynomial and $\boldsymbol{\mu}_i(t)$ is the unit vector from CM to CC on cation i at time t. We use the first-rank Legendre polynomial to calculate the correlation function for the subset of 2L67 - 1C salts at 500 K and 1100 K. Normalized results are shown in Fig. 3.15. At both temperatures, $C_1(t)$ decays on picosecond time scales for cations with $d = 6, 10, 14$. The decay becomes slower as the charge arm increases.

The negative regions in the reorientational correlation function for the 2L67-06 and 2L67-10 cations at $T = 500$ K indicate that the cations are behaving essentially as free rotors undergoing inertial motion. Both salts are OD-CsCl solids at both temperatures, and the cations reorient with $\boldsymbol{\mu}(t)$ changing direction easily and often. There is no steric hindrance to prevent the cations from reorienting within the CsCl crystal. The "cage" created by the anions is symmetric, and there is little or no change in the occupied space when the cation reorients. The energetic barriers to cation reorientation are low, and the increased entropy from the reorientation increases the stability of the CsCl crystal.

The reorientational correlation function for the 2L67-14 cation does not change dramatically between $T = 500$ K and 1100 K, although the salt does go through a *s*-*l* phase change between these two temperatures. In both phases, after a brief inertial period, slower decay is observed.

The 2L67-18 - 1C salt is a CsCl crystal at 500 K, but the cations are unable to reorient freely. The value of $C_1(t)$ reaches 0.25 near 50 ps at $T = 500$ K, and then

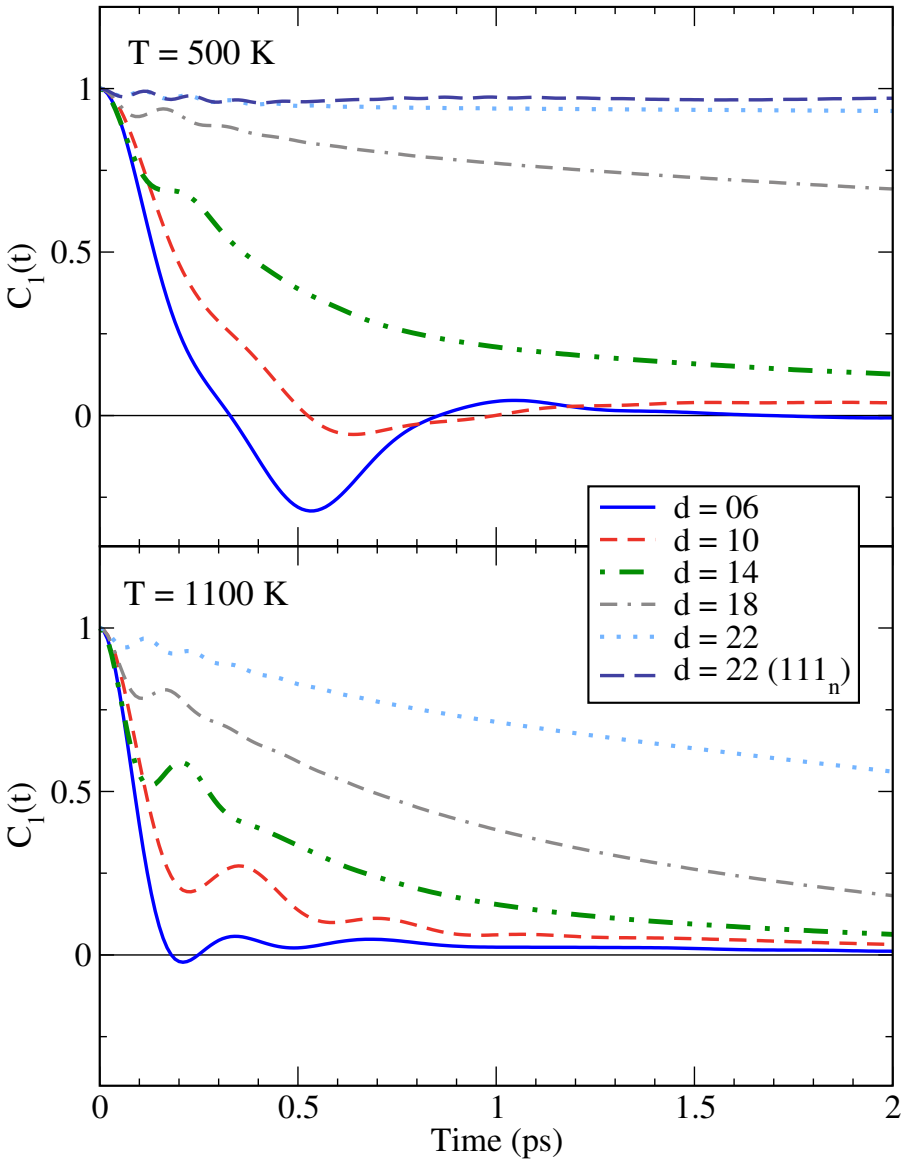

Figure 3.15: The reorientational correlation functions, $C_1(t)$, for selected 2L67 - 1C salts at $T = 500$ K and $T = 1100$ K. At 500 K, the 2L67-06 and 2L67-10 cations (CsCl solids) exhibit negative values indicating inertial rotation. At 1100 K, these two salts remain CsCl solids, and the decay remains on picosecond time scales. The correlation functions for the 2L67-14 cations decay on picosecond time scales at both 500 K (CsCl solid) and 1100 K (liquid). At 500 K, the 2L67-18 (CsCl solid) and 2L67-22 (slow liquid) cations show little decay on picosecond time scales. At 1100 K (liquids), these two salts form ion pairs and exhibit hindered rotational motion.

decays even more gradually. In the CsCl solid at $T = 500$, the relaxation essentially occurs in "jumps" with $\boldsymbol{\mu}$ redirecting from one anion neighbour to another. The majority of the reorientation in the liquid (at $T = 1100$ K), occurs within the first 3 picoseconds.

For the 2L67-22 - 1C salt at $T = 500$ K, we show reorientational correlation functions for a slow liquid, and for the 111_n crystal. Both systems show strong, long-lived orientational correlations. The slow liquid decays on nanosecond time scales, whereas all salts in the 111_n crystal structure remained orientationally ordered until melting. At $T = 1100$ K, the 2L67-22 cation (liquid) does show relaxation, and the reorientational correlation function decays on the order of tens of picoseconds.

In general, the liquids at $T = 1100$ K show an initial rapid decay, corresponding to molecular librations,[121] followed by more gradual decay after the first 0.5 ps, which is consistent with a rotational diffusion mechanism. Roy and coworkers also found that there were two components to the rotational relaxation in model ILs, the first on subpicosecond time scales and the second on picosecond to nanosecond time scales.[59]

The reorientational correlation functions corroborate the findings from the rdfs and the VACFs. Cations with small charge arms are essentially in free rotation. As the charge arm increases, the ions are more likely to form ion pairs. The ion pair lifetimes increase with increasing charge arm,[60] and at large charge arms ions spend significant time bound in ion pairs.

For the salts with large charge arms, the liquid phase does not exhibit spatial or orientational ordering. An orientationally ordered 111_n crystal melts to form an orientationally disordered liquid in a single step. Cooling model ILs with large charge arms removes energy from both translational and rotational modes. The gradual

reduction of the rotational diffusion rate on cooling is unlikely to naturally restore the orientational order present in the 111_n crystal. Model salts with large charge arms tend to vitrify likely because the cooperative orientational relaxations required to spontaneously form an orientationally ordered molecular crystal are simply much too slow, at least on simulation time scales.

3.5 Chapter Summary

We have shown that, in general, the melting point decreases with increasing charge arm, and for salts with identical charge arms, the melting point is lowest for the salts with the largest charge displacement d. These observations may prove useful for the rational design of low melting salts.

We emphasize that the ability of the cation to rotate can strongly influence the crystal structure, melting point, and behaviour of a particular IL as it is cooled. We would expect the CsCl structure to be the stable crystal for all of the 2L - 1C model salts, provided the cations are relatively free to reorient. Cations with smaller charge arms are relatively free to rotate and crystallize spontaneously into orientationally disordered CsCl structures. Cations with larger charge arms form long-lived, directional ion pairs, and the salts do not spontaneously crystallize into any crystal structure. The model salts tend to become trapped in glassy states on simulation time scales. For these "glassy" salts, we found an orientationally ordered 111_n structure that has a lower enthalpy than the CsCl crystal. The low energy 111_n crystal requires that the cations be orientationally ordered. Upon heating, the orientational order of the cations persists in the 111_n structure until the salt melts. We conjecture that the entropy cost of this orientational order creates a nucleation

barrier that is too high for spontaneous crystallization of 111_n to be observed on simulation time scales.

The charge arm influences both the enthalpy and entropy of fusion. At least for the CsCl crystals, both $\Delta_{\text{fus}}\bar{H}$ and $\Delta_{\text{fus}}S$ decrease with increasing charge arm, the former favouring and the latter opposing melting point reduction. However, the change in $\Delta_{\text{fus}}\bar{H}$ outweighs that of $\Delta_{\text{fus}}S$ resulting in the reduced melting points observed. Physically, the directional electrostatic forces arising from charge displacement lower the average enthalpy of both the liquid and CsCl solid phases, but as a function of charge arm, the decrease is faster in the liquid than in the solid. This leads to decreasing values of $\Delta_{\text{fus}}\bar{H}$ and lower melting points of the CsCl crystals as the charge arm increases.

Chapter 4

Melting Point Trends and Solid Phase Diffusivities of Size-Asymmetric Model Salts with Distributed Cation Charge *

4.1 Overview

In this chapter, we study the combined effects of charge distribution and size asymmetry with size-asymmetric 1C - 1C and 2L67 - 1C salts. The ion size ratios are varied in two ways. In Set A, the distance between cation-anion centers is constrained, $\sigma_{\pm} = 0.50$ nm, whereas in Set B, the anion size is held constant, $\sigma_{-} = 0.50$ nm, as discussed in Chapter 2.1. The "size" of the ions is consistent with common anions in real ionic liquids, in between BF_4^- and PF_6^-. The results in this chapter are divided into four parts. In Chapter 4.2, we briefly discuss the size-symmetric salts (labelled A100), which act as a reference set for both size-asymmetric sets, and then examine the Set A size-asymmetric salts. In Chapter 4.3, we present the second set of size-asymmetric salts (Set B). In Chapter 4.4, we discuss the solid state structures and diffusion dynamics of the A300 series of salts.

*Parts of this chapter are being prepared for submission as a journal article.

4.2 Size Set A (Constrained $\sigma_{\pm}$)

The size-symmetric salts were studied in detail in Chapter 3. The charge displacement distance on the cation is a key factor in whether or not the cation is able to reorient, which affects the solidification behaviour of the salts. At small displacements, the cation is in essentially free rotation and the salts spontaneously crystallize into an orientationally disordered cesium chloride (OD-CsCl) solid. At large displacements, the reorientational motion is hindered such that the ions can form directional ion pairs, and cooling the salts gives "glassy" states rather than crystals. The underlying crystal structure is orientationally ordered. The cooperative orientational relaxations required to spontaneously crystallize are much to slow, at least on current simulation time scales.[2] Properties and numerical results for the size-symmetric salts are included below in Table 4.1.

When the ions are size symmetric, there is one uniform length scale for all three types of ion-ion interactions (cation-cation, cation-anion, and anion-anion). Lifting the condition of size symmetry removes the uniformity and creates three distinct length scales for each type of ion-ion interaction. In Set A, we change the ion size ratios while minimizing the changes in cation-anion interactions. We constrain all of the salts in Set A to have the same $\sigma_{\pm}$ while varying σ_{+} and σ_{-}. The specific size ratios considered are given in Table 2.1.

We first consider the charge-centered 1C - 1C salts in Set A. The seven salts we consider span size ratios from 1:1 to 3:1. One might expect that the series of 1C - 1C salts would follow the predictions from the radius ratio rules for charged hard spheres and crystallize as CsCl, NaCl, or wurtzite structures. The 1C - 1C salts from A100 through A233 spontaneously crystallize in CsCl (A100 and A133)

or NaCl (A167, A200, and A233) structures, as predicted. According to the radius ratio rules, the A267 and A300 1C - 1C salts are expected to crystallize in a wurtzite structure; instead, these salts form NaCl crystals. We suspect that the LJ contribution to the interaction potential favours the NaCl arrangement with six neighbouring counterions rather than the wurtzite structure with four. The prepared wurtzite crystals of the A267 and A300 1C - 1C salts rearrange into the lower-enthalpy NaCl structure during heating.

An example of a hysteresis loop is shown in Fig. 4.1, where the average configurational (potential) energy of the A300 1C - 1C salt is plotted as a function of temperature. The thermal width of the hysteresis is 450 K, which is typical for the salts considered here. The average potential energy of the NaCl solid formed upon cooling is higher than the prepared NaCl crystal energy because the spontaneously formed crystal axes and simulation cell axes are not aligned and the solid has a stacking fault. Both liquid and solid phases persist through the entire two-phase simulation at $T = 1100$ K for the A300 1C - 1C salt. The persistence of both phases indicates that the salt is at or near its melting temperature, rather than clearly above or below it. We take the apparent coexistence temperature as T_s and the first temperature that gives a pure liquid as T_l.

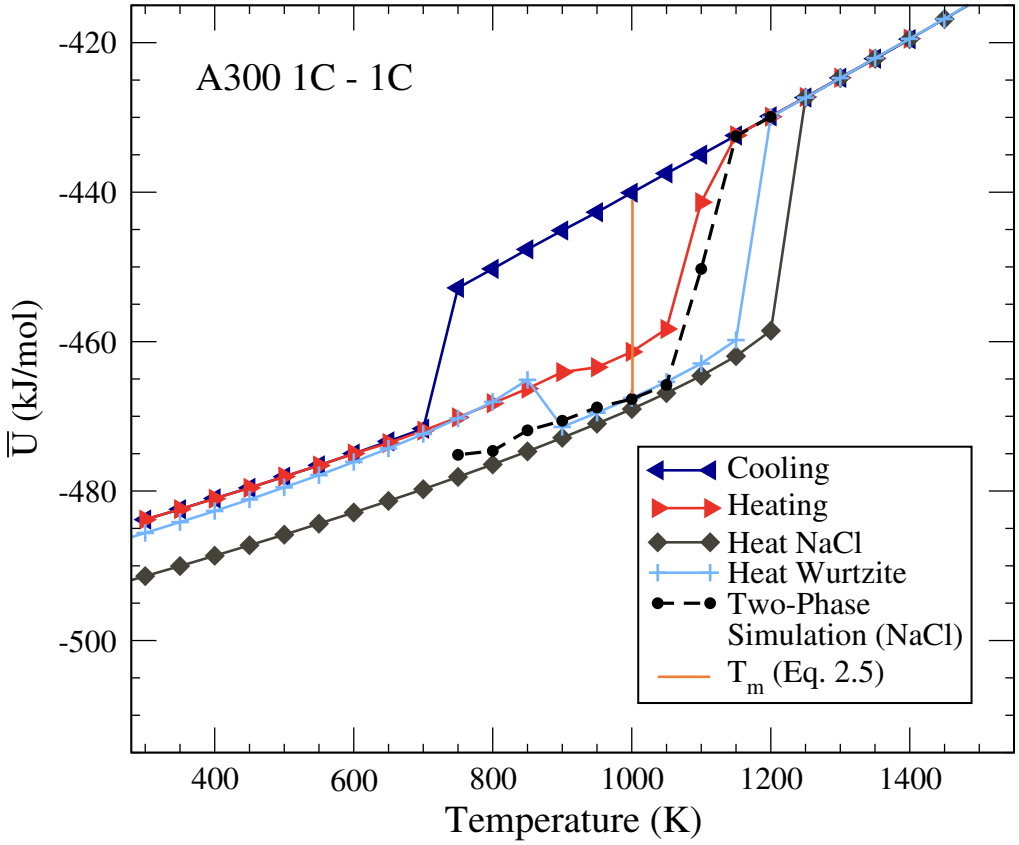

Figure 4.1: Hysteresis plot of the A300 1C - 1C salt. This salt freezes into a NaCl structure. At a size ratio of 3:1, the expected crystal structure for charged hard spheres is wurtzite. The wurtzite crystal we prepared and heated rearranges into NaCl before melting. The five transition-related temperatures for this salt are: $T_- = 750$ K, $T_+ = 1200$ K, $T_m = 1001$ K, $T_s = 1100$, and $T_l = 1150$ K.

The five transition-related temperatures for the series of 1C - 1C salts in Set A are shown in Fig. 4.2. The melting points of the A100, A200, and A233 1C - 1C salts are highest, with $T_s = 1250$ K. These three size ratios coincide with the optimal (or near-optimal) matches between size ratio and packing structure for CsCl and NaCl crystals. The decrease in melting point of the A133 1C - 1C salt marks the destabilization of the CsCl structure, and the subsequent increase in melting point of the A167 1C - 1C salt marks the onset of stabilization of the NaCl structure. For A267 and A300 1C - 1C salts, the melting point decreases which indicates that the NaCl structure is becoming less stable.

Increasing the size ratio from 1:1 to 1.33:1 decreases the melting point by about 100 K. Doubling the size ratio from 1.33:1, to 2.67:1 results in the same melting point, with a peak at intermediate size ratios (between 2:1 and 2.33:1). Beyond size ratios of 2.33:1, the 1C - 1C salts show decreasing melting point trends. Over size ratios varying from 1:1 to 3:1, T_s decreases by about 150 K which indicates that size ratio alone has a marginal effect on the melting temperature.

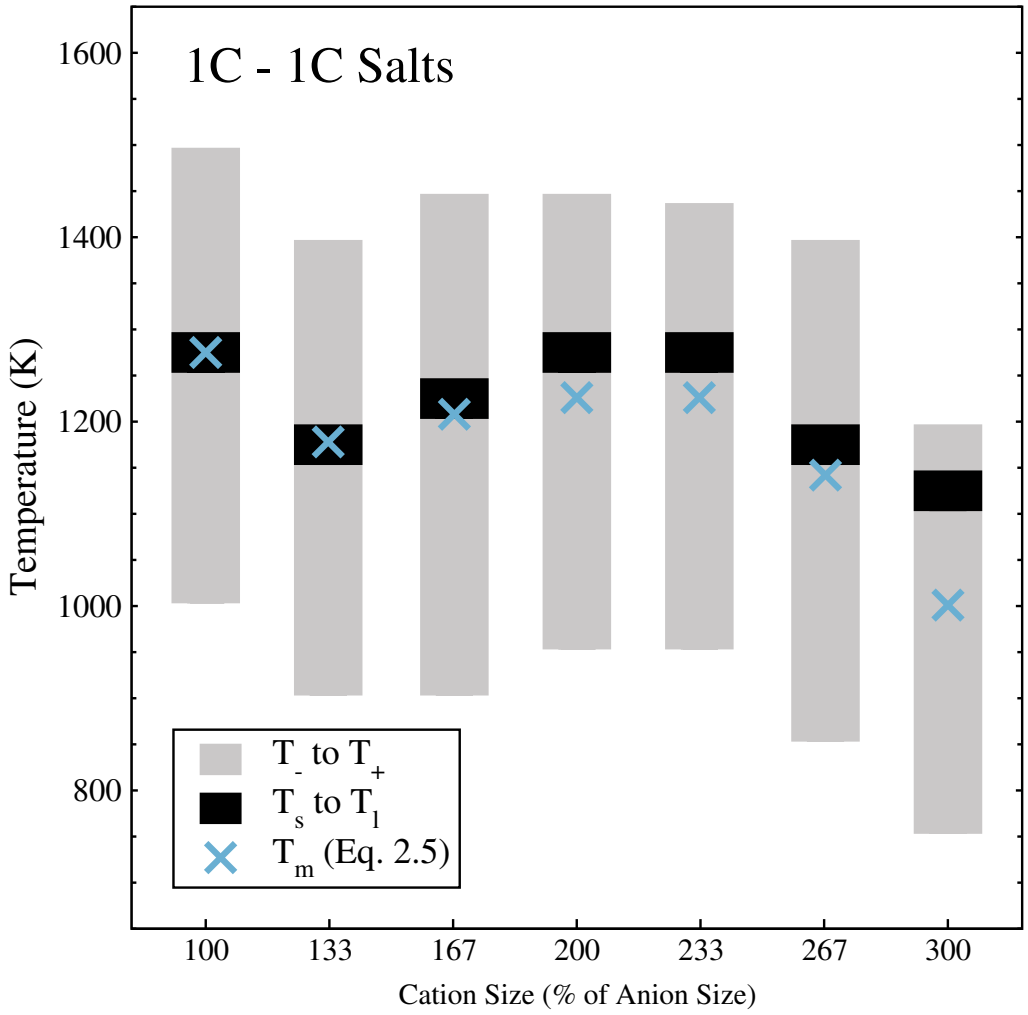

Figure 4.2: Transition temperature summary for the 1C - 1C salts in Set A. The salts in Set A isolate the impact of ion size ratio on melting point by keeping the value of $\sigma_{\pm}$ fixed and varying both σ_{+} and σ_{-}. The overall reduction in T_s as the ion size ratios vary from 1:1 to 3:1 is about 150 K. The melting temperature peak for size-symmetric ions (A100) is for the CsCl structure, while the maximum melting temperatures for the NaCl structure occur at size ratios of 2:1 and 2.33:1.

We have established the melting points, and melting point trends, of the charge-centered salts in Set A. We now use these 1C - 1C salts as starting points for redistributing the cation charge. For each size ratio, we estimate the melting temperatures for a series of salts where 2/3 of the charge is moved away from the cation center by a distance d.

Example hysteresis loops for four salts are shown in Fig. 4.3. In Fig. 4.3(a), the molten salt vitrifies and the cooling and heating traces nearly coincide. The configurational (potential) energies of the CsCl structure and 111_n structure (shown in Fig. 3.3) of this salt increase with increasing temperature at different rates. The structure with the lowest potential energies switches from 111_n to CsCl between 650 K and 700 K. The 111_n crystal has a lower melting point than the CsCl crystal because the CsCl solid permits cation reorientation while the 111_n solid does not. The salts in Fig. 4.3(b) and (c) are typical examples of the hysteresis loops for the spontaneously crystallizing salts. In both Fig. 4.3(b) and (c), the salts freeze as NaCl solids. In (b) there is a slight rearrangement on heating that produced a single crystal, rather than a solid with stacking faults. In Fig. 4.3(d), the salt undergoes the phase transition in stages in both directions. We discuss the premelting structures and the ion dynamics in more detail in Chapter 4.4.

Of the salts in Set A, 38 out of 48 spontaneously crystallize. At size ratios of 2:1 and larger, all of the salts spontaneously crystallize into NaCl solids. The ten salts that do not spontaneously crystallize were the A100 2L67 - 1C salts with $d = 18$ and $d = 22$, and the 2L67 - 1C salts with $14 \leq d \leq 26$ with size ratios A133 and A167.

In Chapter 3, the A100 2L67-18 - 1C salt spontaneously crystallizes into a CsCl structure. Here, with a larger number of ions in the simulation cell, the

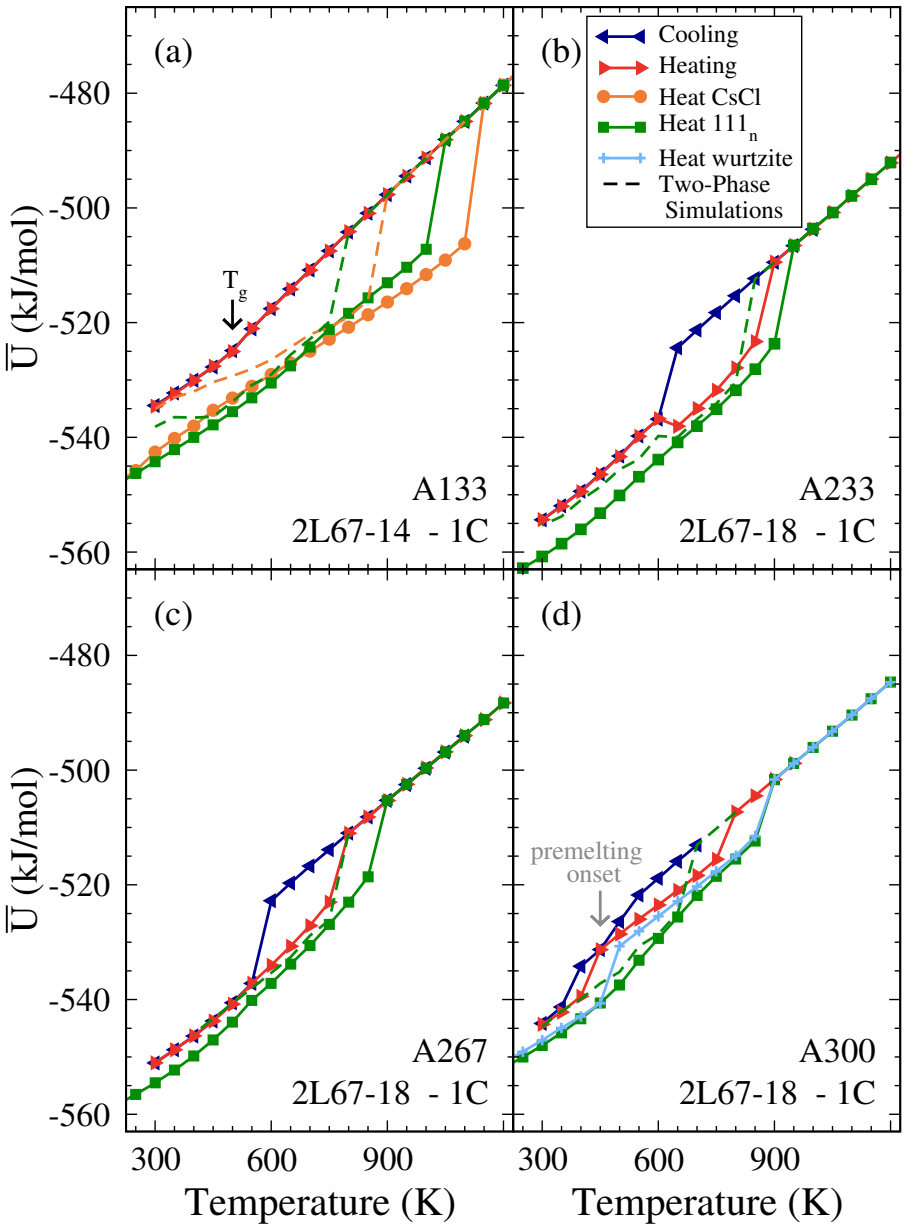

Figure 4.3: The hysteresis loops of four 2L67 - 1C salts in Set A. In (a), the A133 2L67-14 - 1C salt vitrifies upon cooling. The two-phase simulations with each solid, CsCl and 111_n, give different melting temperatures, with CsCl melting between 850 and 900 K, and 111_n melting between 750 and 800 K. This salt is on the borderline between salts with stable CsCl solids and 111_n solids. In (b) and (c), the A233 2L67-18 - 1C and A267 2L67-18 - 1C salts both spontaneously crystallize as NaCl solids. In (d), the A300 2L67-18 - 1C salt crystallizes and melts in phases.

salt vitrifies. It also vitrifies when cooled in smaller temperature increments of 25 K. From heating the set of crystalline solids, we find that the CsCl crystal has the highest T_+. The CsCl structure is likely the solid phase that lies nearest to the liquid for this salt under ambient pressures, which is consistent with the work described in Chapter 3. At lower temperatures, the A100 2L67-18 - 1C salt may undergo solid-solid transitions to a structure with more orientational order. At a slightly larger d, the A100 2L67-22 - 1C salt also vitrifies, which is consistent with the results in Chapter 3. The underlying crystal structure of this salt is orientationally ordered. One candidate crystal structure is a variation on a CsCl structure with orientational order. Some snapshots and details about the crystal structure are given in Appendix E. We heated this structure and found T_+, but did not do two-phase simulations with this structure.

The A133 and A167 salts that vitrify follow the same pattern as the A100 series. As d increases, the melting point decreases and the salts become trapped in glassy states once the reorientational motion of the cations is hindered. The hysteresis cycle for the A133 2L67-14 - 1C salt is shown in Fig. 4.3(a), and the low-temperature behaviour of the crystals was discussed above. The A167 2L67-14 - 1C salt melts from a NaCl structure. The A133 2L67-18 - 1C and A167 2L67-18 - 1C salts both show the CsCl and wurtzite crystals transition to an orientationally disordered solid before melting. For the A133 2L67-18 - 1C salt, we find that the orientationally ordered 111_n solid has the highest melting temperature. However, A167 2L67-18 - 1C salt rearranges into an orientationally disordered NaCl structure before melting. For both A133 and A167 size ratios at $d \geq 22$, the orientationally ordered solid melts directly, while heating other crystal structures results in lower melting points and subtle rearrangements before melting.

Table 4.1 gives some of the properties of Set A salts, where the $d = 0$ entry corresponds to the 1C - 1C salt. In Table 4.1, T_s gives the highest temperature of the stable solid from the two-phase simulations for each salt, with the relevant crystal structure given in the third column. For the polymorphic salts and salts that show premelting transitions, we give the highest melting point because we are interested in the minimum melting point reductions.

The temperature-dependent properties of each salt are reported at T_s. The average reduced densities, $\bar{\rho}^*$, for the solid and liquid states are calculated as $(N_+\sigma_+^3 + N_-\sigma_-^3)/\bar{V}$, where N and σ refer to the number of ions and the LJ length parameter with subscripts referring to the cations (+) or anions (−), $\bar{V}$ is the average simulation cell volume in nm^3. The ratio $\bar{U}_s^{\mathrm{IP}}/U_{iso}^{\mathrm{IP}}$ is a measure of how much stability the crystal structure gains relative to the minimum potential energy of an isolated ion pair, with higher numbers indicating that there is more thermodynamic incentive for the salt to crystallize. The enthalpy of fusion, $\Delta_{\mathrm{fus}}\bar{H}$, at T_s is estimated as $\bar{H}_l - \bar{H}_s$, where the average enthalpies of each phase at T_s are calculated from single-phase simulations.

The trends within most size ratios follow the trends of the size-symmetric salts. The average reduced densities of the liquids generally increase while T_s, $\bar{U}_s^{\mathrm{IP}}/U_{iso}^{\mathrm{IP}}$, and $\Delta_{\mathrm{fus}}\bar{H}$ generally decrease with increasing cation charge displacement. For the 1C - 1C salts in Set A, $\bar{U}_s^{\mathrm{IP}}/U_{iso}^{\mathrm{IP}}$ decreases monotonically as the size ratio increases, from 1.72 to 1.62. In Set A, the heats of fusion range from 44 kJ/mol of ion pairs (A100 1C - 1C) to 6 kJ/mol of ion pairs (A300 2L67-26 - 1C). The *s-l* transition occurs in stages for the A300 2L67-26 - 1C salt; the low $\Delta_{\mathrm{fus}}\bar{H}$ is a reflection of the increased solid enthalpy after the premelting transitions at lower temperatures. Another indication that the solids of the A267 and A300 salts undergo premelting

transitions comes from a notable decrease in the average reduced densities of the solid as d increases. The premelting transitions are discussed in Chapter 4.4 below.

Table 4.1: Properties of the Set A salts. The crystal structures marked with an asterisk likely have a s-s transition to a more orientationally ordered crystal structure at lower temperatures. The var-CsCl structure is shown in Appendix E.2. The crystal structures listed as fcc(+) and fcc(PC) melt from a cation fcc lattice and fcc plastic crystal phase, respectively.

Size Ratio	d	Crystal Structure	T_s (K)	$\bar{\rho}^*(s)$ —	$\bar{\rho}^*(l)$ —	$\bar{U}_s^{\mathrm{IP}}/U_{iso}^{\mathrm{IP}}$ —	$\Delta_{\mathrm{fus}}\bar{H}$ (kJ/mol)
A100	0	CsCl	1250	1.08	0.78	1.72	44
	06	CsCl	1200	1.08	0.81	1.57	40
	10	CsCl	1150	1.09	0.83	1.47	35
	14	CsCl	1000	1.11	0.89	1.37	27
	18	CsCl*	800	1.13	0.95	1.29	19
	22	var-CsCl	650	1.14	0.97	1.22	22
A133	0	CsCl	1150	1.10	0.84	1.71	34
	06	CsCl	1100	1.10	0.86	1.56	31
	10	CsCl	1000	1.12	0.90	1.46	26
	14	CsCl*	850	1.13	0.95	1.37	18
	18	111n	700	1.08	1.00	1.30	18
	22	111n	650	1.10	0.98	1.22	21
	26	111n	550	1.10	0.99	1.18	16
A167	0	NaCl	1200	1.03	0.86	1.70	36
	06	NaCl	1150	1.04	0.87	1.55	33
	10	NaCl	1100	1.05	0.89	1.44	29
	14	NaCl	950	1.07	0.94	1.36	21
	18	NaCl*	750	1.10	0.99	1.28	18
	22	111n	700	1.09	0.96	1.20	18
	26	111n	550	1.11	0.99	1.17	15

Continued on next page...

Table 4.1: (Continued)

Size Ratio	d	Crystal Structure	T_s (K)	$\bar{\rho}^*(s)$ —	$\bar{\rho}^*(l)$ —	$\bar{U}_s^{\mathrm{IP}}/U_{iso}^{\mathrm{IP}}$ -	$\Delta_{\mathrm{fus}}\bar{H}$ (kJ/mol)
A200	0	NaCl	1250	1.10	0.86	1.69	40
	06	NaCl	1200	1.11	0.88	1.54	37
	10	NaCl	1150	1.11	0.89	1.43	32
	14	NaCl	1000	1.12	0.93	1.34	24
	18	NaCl	800	1.13	0.98	1.26	18
	22	NaCl	700	1.11	0.97	1.19	16
	26	NaCl	600	1.11	0.96	1.16	14
A233	0	NaCl	1250	1.14	0.88	1.66	39
	06	NaCl	1200	1.15	0.89	1.52	37
	10	NaCl	1100	1.16	0.92	1.42	31
	14	NaCl	950	1.17	0.96	1.33	23
	18	NaCl	800	1.14	0.98	1.25	16
	22	NaCl	650	1.15	0.99	1.19	16
	26	NaCl	550	1.13	0.99	1.15	13
A267	0	NaCl	1150	1.19	0.92	1.65	35
	06	NaCl	1100	1.19	0.93	1.50	32
	10	NaCl	1050	1.19	0.94	1.40	27
	14	NaCl	900	1.18	0.97	1.32	19
	18	NaCl	750	1.15	0.99	1.24	13
	22	fcc(+)	600	1.16	1.00	1.18	12
	26	fcc(PC)	550	1.09	0.98	1.14	8
A300	0	NaCl	1100	1.20	0.94	1.62	30
	06	NaCl	1050	1.21	0.95	1.48	27
	10	NaCl	900	1.22	1.00	1.39	21
	14	NaCl/fcc(+)	750	1.22	1.03	1.31	15
	18	fcc(+)	650	1.17	1.03	1.23	10
	22	fcc(+)	550	1.15	1.02	1.17	8
	26	fcc(PC)	550	1.07	0.98	1.13	6

The melting point trends across Set A are summarized in Fig. 4.4, where we show T_s to T_l for each salt. The $d = 0$ series of salts are the 1C - 1C salts, repeated from Fig. 4.2. The distance between counterion centers is held constant in Set A. The changes in the melting points of the 1C - 1C salts are due to the ion size ratios and, more specifically, to the changes in the interactions between like ions. As the size ratio increases, the electrostatic interactions become less repulsive between larger ions and more repulsive between smaller ions.

For the Set A salts with $d \leq 18$, the melting point trends are similar. The A100 and A200 salts are the two optimal size ratios for the CsCl and NaCl structures, and also have the highest melting points for $d \leq 18$. Each series of salts with equal $d \leq 18$ shows a decrease in melting point from A100 to A133 (destabilizing CsCl solid), an increase from A133 to A200 (stabilizing NaCl solid), and a decrease at or beyond A233 (destabilizing NaCl solid). Each size ratio series shows two distinct melting point peaks corresponding to the CsCl and NaCl solid structures when $d \leq 18$.

The melting point trends change for the $d = 22$ series of salts. There is only one peak in the melting temperature between A167 and A200. The A100 2L67-22 - 1C salt is not stable as a CsCl solid like the A100 salts with $d \leq 18$. Instead, the crystal structure of the A100 2L67-22 - 1C salt is orientationally ordered.

The variation of melting temperatures across size ratios ranges from 150 K for the 1C - 1C salts, to 250 K at $d = 10$ and 14, and down to 50 K for $d = 26$. For all of the size ratios except A200, $T_s = 550$ K. T_s of the A200 2L67-26 - 1C salt is only 50 K higher. The consistency of T_s for the $d = 26$ salts suggests that the variation in melting temperature due to the size ratios (with constant $\sigma_{\pm}$) can be suppressed by large cation displacement distances (d).

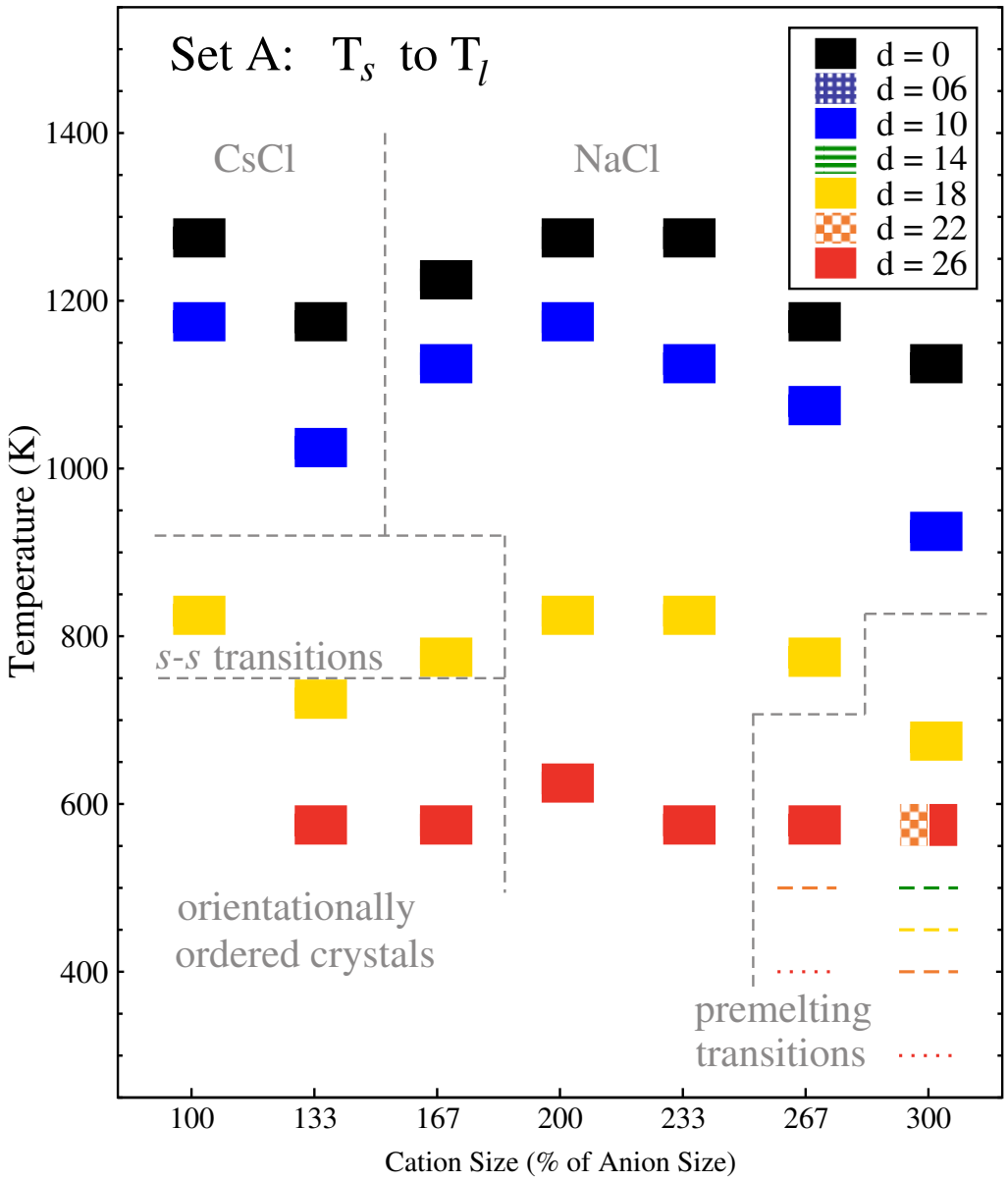

Figure 4.4: Melting temperature summary for the salts in Set A. The blocks give the 50 K range of T_s to T_l for each salt. The dashed grey lines separate the salts by their solid types. The majority freeze as NaCl solids. On the left, the salts with equal or near-equal size ions freeze as CsCl solids, show *s-s* transitions, or in the bottom left, become trapped in glassy states upon cooling, depending on d. In the bottom right, the horizontal lines indicate the approximate onset of fast ion conductor (dashed lines) and plastic crystal (dotted lines) phases. (See text for description and onset criteria details.)

A plot of T_s against the cation displacement distance, d, for the salts in Set A is shown in Fig. 4.5, and show similar trends for all of the size ratios. The plot in Fig. 4.5, highlights that the A133 and A300 salts have the lowest melting points while the A100, A200 and A233 are consistently the size ratios with the highest melting temperatures.

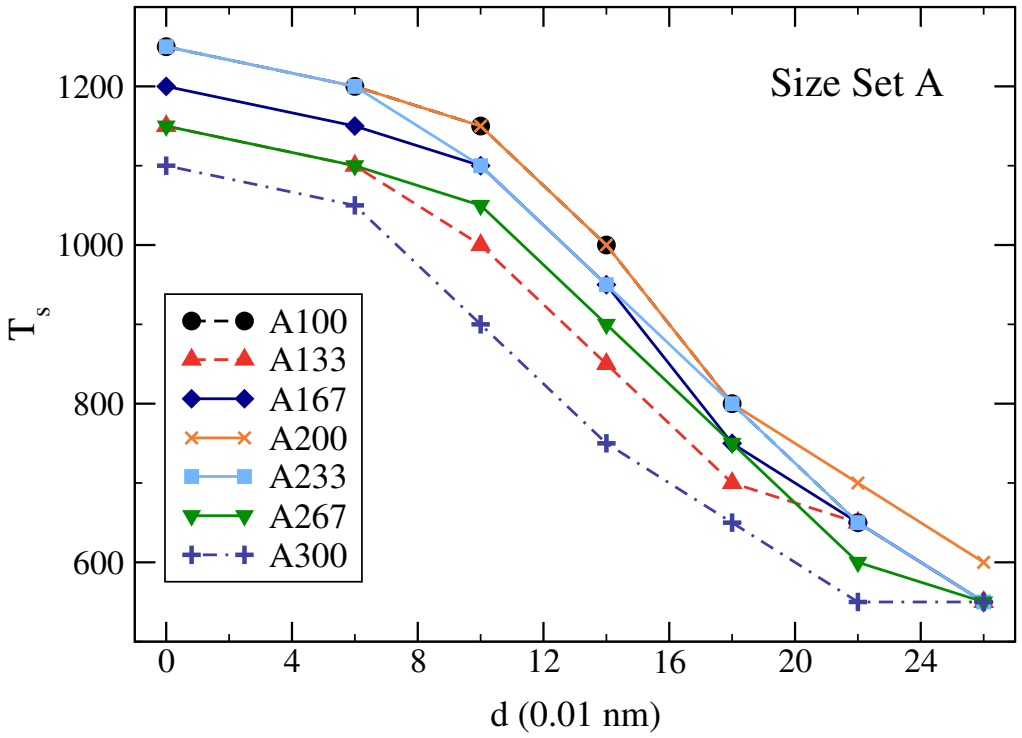

Figure 4.5: Melting points of the Set A salts as a function of the cation charge displacement distance d. The A100, A200, and A233 salts show the smallest melting point reductions, while the A133 and A300 show the largest melting point reductions.

The melting temperature trends of the Set A salts, with constrained $\sigma_{\pm}$, have been established and discussed. We now move on to Set B, where σ_{-} is fixed.

4.3 Size Set B (Unconstrained $\sigma_{\pm}$)

In Set B, we examine the impact of ion size on the melting point where σ_{-} is held constant at 0.50 nm while σ_{+} and $\sigma_{\pm}$ increase. Because $\sigma_{\pm}$ increases, the attractive electrostatic interactions between counterions become weaker. As in Set A, we consider size ratios between 1:1 and 3:1, with the specific size ratios given in Table 2.1.

In contrast with the charge-centered (1C - 1C) salts from Set A, the Set B 1C - 1C salts do not exhibit obvious markers of the crystal structure changes in their melting points trends. Instead, the melting points of the Set B 1C - 1C salts decrease monotonically. As the size ratio increases from 1:1 to 3:1, T_s of the 1C - 1C salts in Set B drops from 1250 K to 750 K, which is a significantly larger reduction than the salts in Set A (150 K). The melting point reduction of the Set B 1C - 1C salts is attributed to the increasing size of the cation and resulting weaker electrostatic interactions.

Properties of the Set B salts are given in Table 4.2. The properties in Table 4.2 are the same as those listed for Set A in Table 4.1, but with an additional column for the average potential energy of the solid $\bar{U}_s$ at T_s. The average potential energies of the solids $\bar{U}_s$ at T_s, for the Set B 1C - 1C salts are listed in Table 4.2 as the $d = 0$ entry, and increase from -494 to -250 kJ/mol of ion pairs as the size ratio increases. The increase of about 245 kJ/mol of ion pairs contrasts sharply with the 1C - 1C salts in Set A, which show an increase of about 30 kJ/mol of ion pairs, from -494 to -465 kJ/mol of ion pairs. The average potential energies of the Set B salts are in the same range as some prototypic ionic liquids (between -300 to -400 kJ/mol of ion pairs).[11,16,71]

The trends across the Set B 2L67 - 1C salts properties given in Table 4.2 are also worth noting. The average reduced densities of the solids vary between 1.0 and 1.1, much like the salts in Set A. The trend of increasing solid densities reverses for the B267 and B300 salts with large d. These salts also show premelting transitions, like the salts in Set A discussed in Chapter 4.4. The decrease in the average reduced density of the solid and $\Delta_{\rm fus}\bar{H} \leq 10$ kJ/mol of ion pairs are consistent with premelting transitions to higher entropy states. Within each size ratio, the trends for $\bar{U}_s^{\rm IP}/U_{iso}^{\rm IP}$ and $\bar{\rho}^*(l)$ are consistent with the Set A salts; as d increases, $\bar{U}_s^{\rm IP}/U_{iso}^{\rm IP}$ generally decreases while $\bar{\rho}^*(l)$ generally increases.

Table 4.2: Properties of the Set B salts. Each salt is identified by the size ratio and cation charge displacement distance d. As in Table 4.1, the crystal structure is that of the last stable solid before melting, where fcc(+) means a fcc lattice of cations. The highest temperature where the solid persists in the two-phase simulations is T_s. The average reduced densities, $\bar{\rho}^*$, average potential energy of the solid, $\bar{U}_s$, and $\Delta_{\rm fus}\bar{H}$ are given at T_s. At each size ratio, the $d = 0$ entry refers to the charge-centered 1C - 1C salt.

Size Ratio	d	Crystal Structure	T_s (K)	$\bar{\rho}^*(s)$ —	$\bar{\rho}^*(l)$ —	$\bar{U}_s$ kJ/mol	$\bar{U}_s^{\rm IP}/U_{iso}^{\rm IP}$ —	$\Delta_{\rm fus}\bar{H}$ (kJ/mol)
B133	0	CsCl	1050	1.08	0.83	-425	1.74	32
	6	CsCl	1050	1.07	0.83	-426	1.61	31
	10	CsCl	1000	1.08	0.85	-430	1.52	28
	14	CsCl	900	1.09	0.89	-439	1.44	23
	18	CsCl	750	1.11	0.95	-454	1.36	15
	22	var-111_n	600	1.12	1.00	-486	1.31	18
	26	var-111_n	600	1.08	0.97	-524	1.24	19
B167	0	NaCl	1000	0.99	0.83	-371	1.75	29
	6	NaCl	950	1.01	0.86	-374	1.64	27
	10	NaCl	950	1.00	0.86	-375	1.56	26
	14	NaCl	900	1.01	0.88	-380	1.48	22
	18	NaCl	800	1.03	0.92	-389	1.42	18

Continued on next page...

Table 4.2: (Continued)

Size Ratio	d	Crystal Structure	T_s (K)	$\bar{\rho}^*(s)$ —	$\bar{\rho}^*(l)$ —	$\bar{U}_s$ kJ/mol	$\bar{U}_s^{\mathrm{IP}}/U_{iso}^{\mathrm{IP}}$ -	$\Delta_{\mathrm{fus}}\bar{H}$ (kJ/mol)
	22	NaCl	700	1.05	0.95	-402	1.35	14
	26	111_n	600	1.08	0.98	-424	1.30	14
	30	111_n	550	1.09	0.98	-457	1.25	15
B200	0	NaCl	950	1.05	0.84	-334	1.78	31
	6	NaCl	950	1.05	0.84	-334	1.67	30
	10	NaCl	900	1.06	0.87	-337	1.61	28
	14	NaCl	900	1.06	0.86	-338	1.54	26
	18	NaCl	850	1.07	0.89	-343	1.47	23
	22	NaCl	800	1.07	0.90	-348	1.40	20
	26	NaCl	700	1.08	0.94	-359	1.34	15
	30	NaCl	600	1.08	0.97	-377	1.29	13
	34	NaCl	550	1.08	0.97	-402	1.24	12
B233	0	NaCl	900	1.08	0.85	-301	1.78	29
	6	NaCl	900	1.08	0.85	-301	1.69	29
	10	NaCl	900	1.08	0.85	-301	1.63	28
	14	NaCl	850	1.09	0.87	-304	1.57	26
	18	NaCl	800	1.10	0.89	-308	1.52	24
	22	NaCl	800	1.09	0.89	-310	1.45	21
	26	NaCl	700	1.11	0.93	-318	1.39	17
	30	NaCl	650	1.10	0.94	-325	1.33	14
	34	NaCl	600	1.08	0.95	-338	1.28	12
B267	0	NaCl	800	1.11	0.88	-274	1.80	25
	6	NaCl	800	1.11	0.88	-275	1.72	25
	10	NaCl	800	1.11	0.88	-275	1.66	25
	14	NaCl	800	1.11	0.88	-275	1.59	23
	18	NaCl	750	1.12	0.90	-278	1.55	22
	22	NaCl	750	1.11	0.90	-280	1.48	20
	26	NaCl	700	1.11	0.92	-284	1.43	17
	30	NaCl	650	1.11	0.94	-289	1.38	14

Continued on next page...

Table 4.2: (Continued)

Size Ratio	d	Crystal Structure	T_s (K)	$\bar{\rho}^*(s)$ —	$\bar{\rho}^*(l)$ —	$\bar{U}_s$ kJ/mol	$\bar{U}_s^{\mathrm{IP}}/U_{iso}^{\mathrm{IP}}$ -	$\Delta_{\mathrm{fus}}\bar{H}$ (kJ/mol)
	34	NaCl	600	1.10	0.95	-297	1.32	11
	42	fcc(+)	500	1.08	0.97	-325	1.36	8
	50	fcc(+)	450	1.04	0.97	-382	1.46	5
B300	0	NaCl	750	1.11	0.89	-250	1.79	22
	6	NaCl	750	1.11	0.89	-250	1.71	21
	10	NaCl	750	1.11	0.89	-250	1.66	21
	14	NaCl	700	1.13	0.91	-253	1.62	20
	18	NaCl	700	1.12	0.91	-254	1.57	19
	22	NaCl	700	1.11	0.91	-254	1.50	17
	26	NaCl	650	1.12	0.93	-258	1.46	15
	30	NaCl	650	1.09	0.93	-259	1.40	12
	34	NaCl	600	1.09	0.95	-265	1.36	10
	42	fcc(+)	550	1.02	0.95	-278	1.26	5
	50	fcc(+)	450	1.04	0.97	-315	1.21	4
	58	fcc(+)	450	1.02	0.95	-381	1.14	4

We plot T_s to T_l for the Set B salts in Fig. 4.6. The melting point trends in Set B differ from those in Set A. The differences between Set A (Fig. 4.4) and Set B (Fig. 4.6) highlight how isolating the effect of size asymmetry on melting point is difficult because of the different length scales involved.

The melting points of the Set B charge-centered salts decrease monotonically as the size ratio increases. As expected, moving 2/3 of the unit charge away from the cation center generally reduces the melting point. At small d values, the melting point trends follow the 1C - 1C trends closely across increasing size ratios.

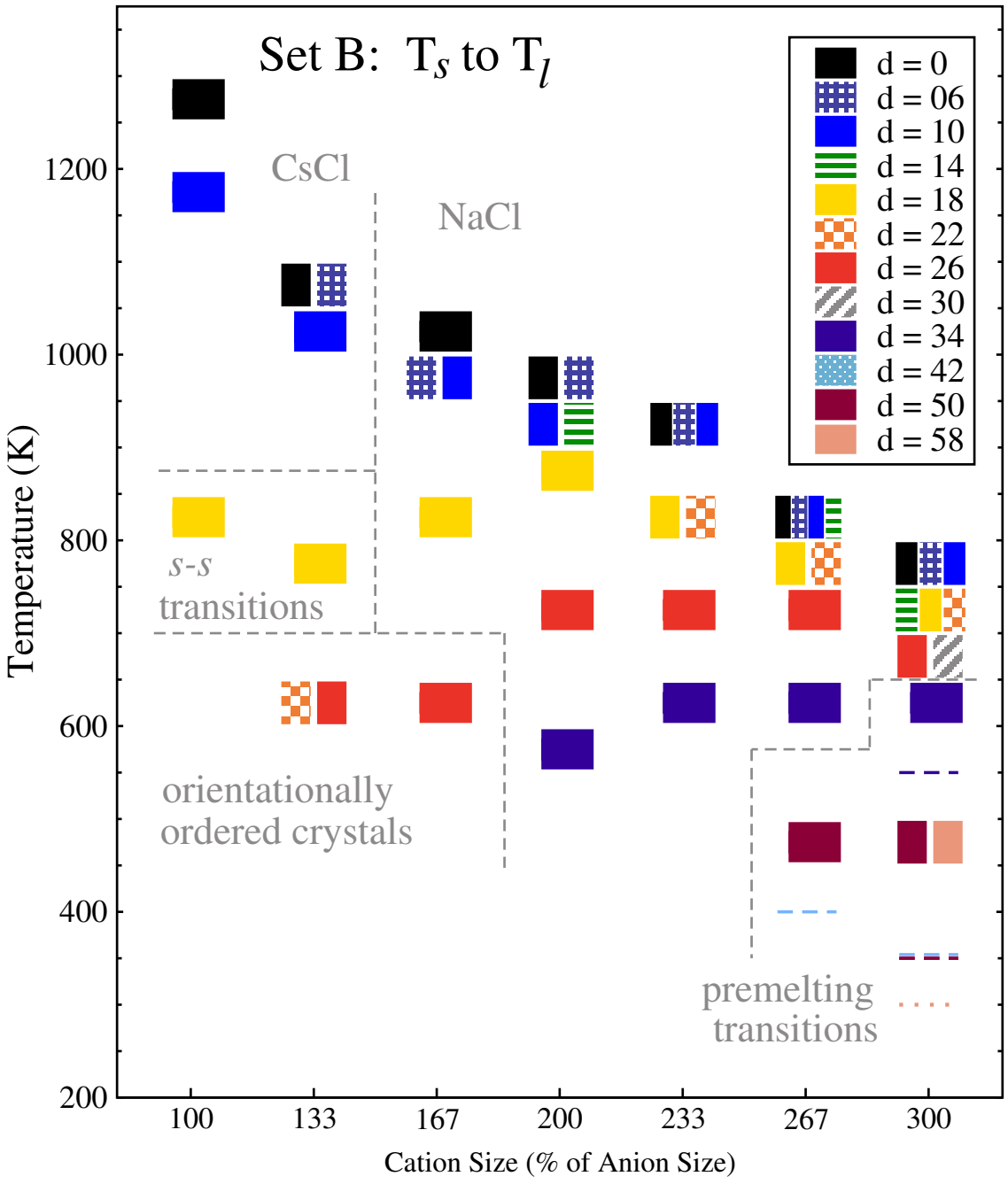

Figure 4.6: Melting point summary of the Set B salts. The blocks give the 50 K range of T_s to T_l for each salt. The dashed grey lines separate the salts by their solid types and the boundaries are similar to those found in Set A (Fig. 4.4). In the bottom left, the salts become trapped in glassy states upon cooling. In the bottom right, the horizontal lines indicate the approximate onset of fast ion conductor (dashed lines) and plastic crystal (dotted lines) phases.

At $d = 14$, we see the first indication that the crystal structures affects the melting point, with the B133 2L67-14 - 1C (CsCl) and B167 2L67-14 - 1C (NaCl) salts have the same melting point ranges. As d increases to 18, the melting point of the B133 salt (CsCl) is lower than either of the corresponding A100 (CsCl) or B167 (NaCl) salts. The drop in melting point of the B133 2L67-18 - 1C salt changes the melting point trends across the $d = 18$ series. The series of $d = 18$ melting points develops a second peak at B200 that is higher than the CsCl peak for the A100 2L67-18 - 1C salt. At $d \geq 22$, the second melting point peak extends to even higher size ratios, with $T_s = 800$ K for the size ratios of 2:1 and 2.33:1. In the $d = 26$, 30, and 34 salt series, the melting points have a single peak that spans multiple size ratios. The peaks extend to larger size ratios as d increases.

Insight into why the melting point peak shifts to larger size ratios is provided by the ratio of the average potential energy per ion pair in the solid to the minimum potential energy of an isolated ion pair, $\bar{U}_s^{\mathrm{IP}}/U_{iso}^{\mathrm{IP}}$. In Set A, $\bar{U}_s^{\mathrm{IP}}/U_{iso}^{\mathrm{IP}}$ decreases from 1.72 to 1.62 as the size ratio increased for the 1C - 1C salts. However, in Set B, $\bar{U}_s^{\mathrm{IP}}/U_{iso}^{\mathrm{IP}}$ peaks at B267 with a value of 1.80 for the 1C - 1C salts. Based on this ratio, the Set B salts with larger size ratios have *more* thermodynamic incentive to crystallize.

If we follow the melting point trends for $d = 22$, 26, or 30 in Fig. 4.6, we can see the transition between two main influences on melting point. In the lower left of Fig. 4.6, the cation charge distribution has the largest influence on the melting points. The charge distribution leads to strong ion pairing. The crystal structures are orientationally ordered to maintain the ion pairs. If the salt is dominated by ion pairing, then the melting point is low. As the cation grows larger in Set B, the off-center charge site recedes from the cation surface and the cation charge distri-

bution becomes a weaker influence on melting point; the melting points increase. The cations in these salts are able to reorient about the lattice sites and interact favourably with more than one nearest neighbour, which stabilizes the solid. Once the cation is large enough that d is a minor perturbation, the melting points of the salts join the downward trend due to the ion sizes.

The cations increase in size as the size ratio increases in the Set B salts. In the size-symmetric salts (A100), $d = 22$ (0.22 nm) leads to strong ion pairing because the cation radius is near 0.25 nm, but $d = 22$ does not lead to ion pairing for B300, where the cation radius is near 0.75 nm. A plot that takes these differences into consideration is shown in Fig. 4.7, where T_s/T_s(1C - 1C) is plotted against the normalized charge arm of the cation, as defined in Eq. (2.2). The trends in Fig. 4.7 are similar across size ratios, and also remarkably similar to the trends in Chapter 3 (Fig. 3.9) where different fractions of the cation charge are moved off-center in size-symmetric salts.

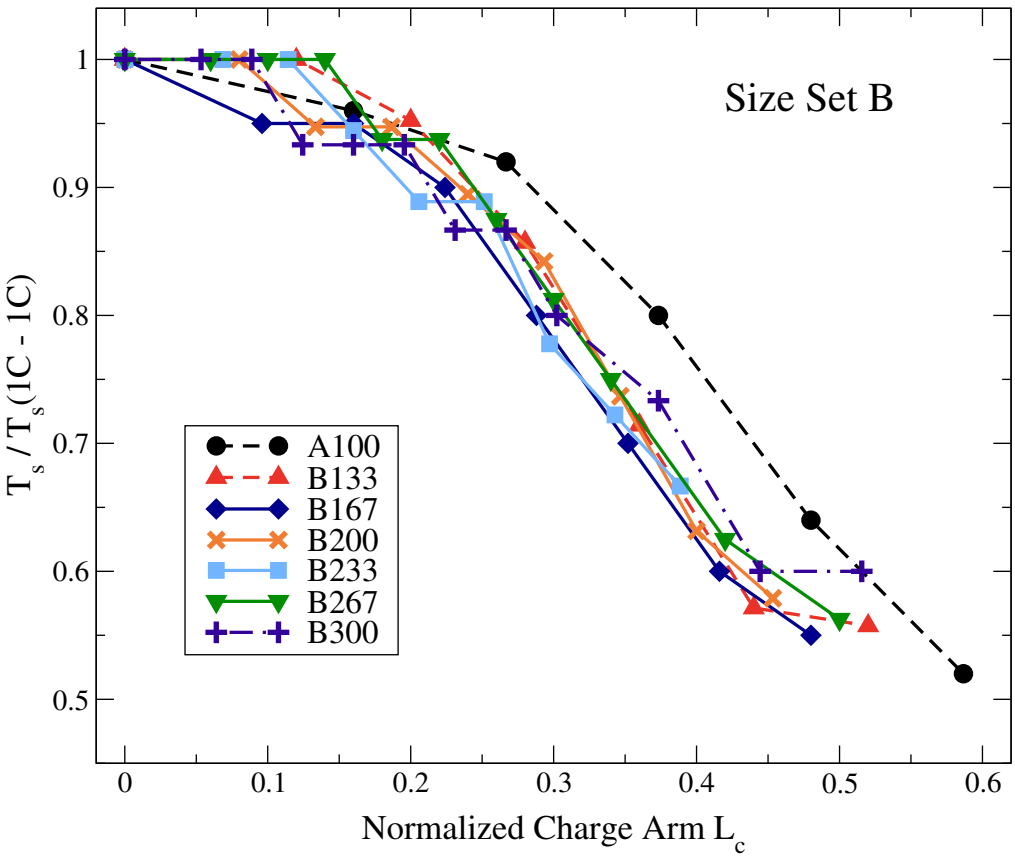

Figure 4.7: Melting points (T_s) scaled by T_s of the 1C - 1C salt (of the same size ratio) plotted against the normalized charge arm, L_c. The trends shown here are similar to the trends established in Chapter 3, where the fraction of off-center charge is varied. (See Fig. 3.9.)

4.4 Solid Structure and Ion Dynamics

Six of the A267 and A300 salts show premelting transitions noted in Fig. 4.4. The A267 2L67 - 1C salts with $d \geq 22$ and the A300 2L67 - 1C salts with $d \geq 14$ display intermediate phases between the low-enthalpy solids and the liquids. In this section, we explore the ion dynamics for the A300 series of salts, with emphasis on the A300 2L67-22 - 1C and A300 2L67-26 - 1C salts. We compare the salts at $T =$ 550 K, which is T_s for both salts.

The mean squared displacement (msd) provides insight into the particle dynamics and is calculated as[119]

$$\langle \Delta \mathbf{r}(t)^2 \rangle = \langle |\mathbf{r}(t) - \mathbf{r}(0)|^2 \rangle, \tag{4.1}$$

where $\mathbf{r}(t)$ is the particle position at time t, and the angular brackets denote an ensemble average. A log-log plot of the msd of both ions in the A300 series of salts at 550 K is shown in Fig. 4.8. The Einstein relation[119] is used to calculate the diffusion coefficients D from the msd as $D = \lim_{t\to\infty} \langle |\mathbf{r}(t) - \mathbf{r}(0)|^2 \rangle / 6t$.

For each of the A300 salts, the smaller anions have a higher msd than the larger cations, as expected. All of the salts are solids at $T = 550$ K, and the majority of the ions show no net translational motion. The deviations begin with $d = 14$, where there is a small increase in the anion msd over 0.5 - 1.0 ns time scales. For the A300 salts with $d = 18$ and 22, the anions show linear (diffusive) behaviour whereas the cations do not. For these two salts, the anions move through a cation lattice with diffusion coefficients of $D_- = 1.548\ (\pm\ 0.108)\ \times 10^{-10}$ m^2/s at $T = 550$ K for $d = 18$, and $D_- = 6.719\ (\pm\ 0.286)\ \times 10^{-10}$ m^2/s for $d = 22$.

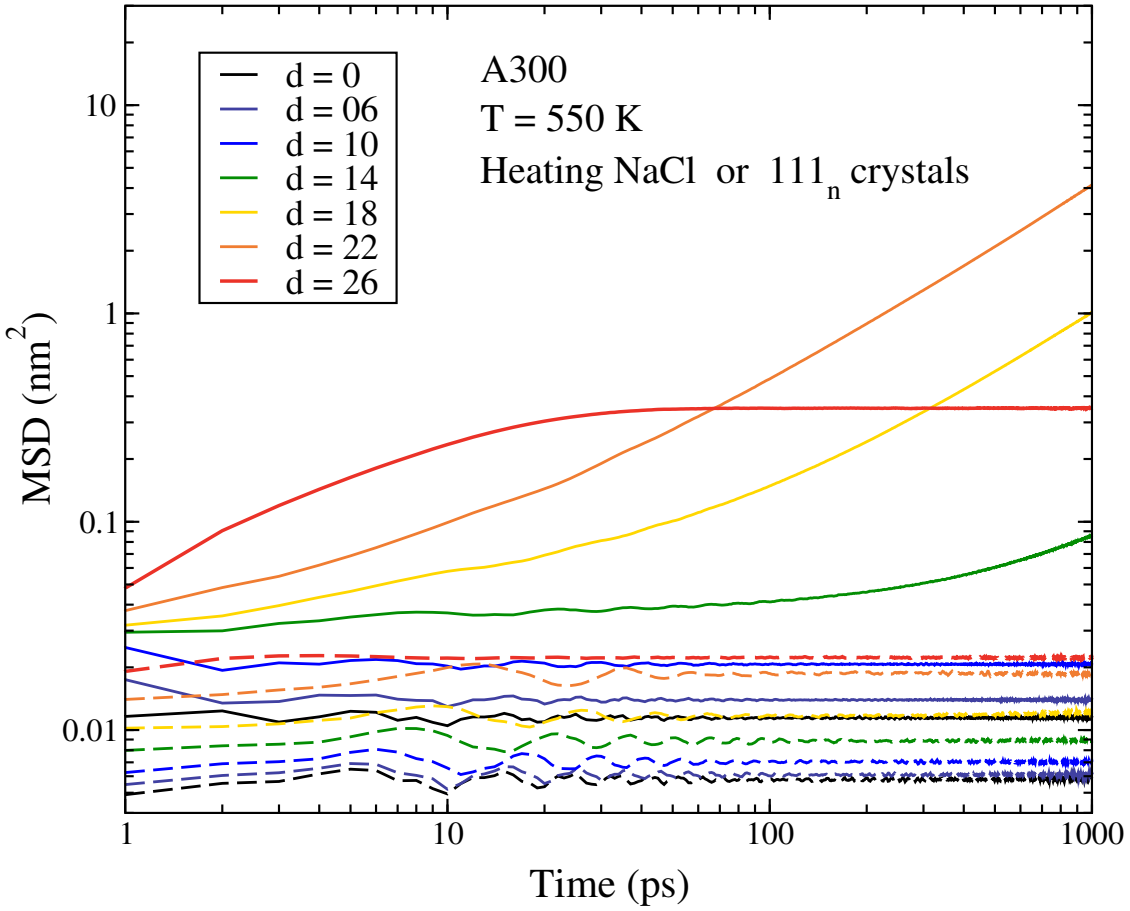

Figure 4.8: The mean square displacements for the Set A salts with a 3:1 size ratio at $T = 550$ K. Cation msd are marked with dashed lines and anions with solid lines. The A300 salts with $d \leq 10$ are crystalline, and the msd plots are from heating NaCl crystals. For the $d \geq 14$ salts, we show the msd from heating the 111_n structure. For the salts with $d = 18$ and 22, the anions show diffusive motion while the cations do not. The msd of the ions in the $d = 26$ salt shows no net translational motion, but the anion msd is an order of magnitude larger than that of the cation. This salt exists in a plastic crystal phase at $T = 550$ K.

We have not attempted to determine the premelting transition temperature accurately here because we are interested in the *s*-*l* transition. We approximate the onset of the fast ion conductor phase as the lowest temperature where we see an increase in the average potential energy and an anion diffusion coefficient above an arbitrary threshold of 1×10^{-10} m^2/s during the heating of the crystals. An estimation using the Nernst-Einstein relation puts the ion conductivities in the range of 0.01 S/cm, a generally accepted threshold for superionic conductor behaviour.[122]

For comparison, the α-phase of AgI, which is stable between $T = 420$ K and 831 K, is a common example of a superionic conductor. The iodide ions form a bcc lattice and the silver ions move through it. From molecular dynamics simulations at 560 K, the diffusion coefficient of the more mobile Ag ions has been reported as 3.5×10^{-9} m^2/s.[123] The ion diameters used in the study were 0.063 nm for silver and 0.22 nm for iodide, giving a large:small ion size ratio of 3.49.[123]

In the A300 2L67-26 - 1C salt, which has the largest size ratio and charge displacement considered here, the anion and cation both have diffusion coefficients of zero, but the msd of the anions is an order of magnitude larger than that of the cations (0.351 nm^2 vs 0.0223 nm^2) at $T = 550$ K. Here, the salt forms a plastic crystal phase where the ions rotate as pairs; the larger cations vibrate and reorient about lattice positions. As the cation reorients, the anion traces a path on the cation surface and follows the movements of the off-center charge site. The anion traces out a larger path than the cation, which explains why the msd of the anion is an order of magnitude larger.

The approximate onset temperature of the plastic crystal phase, as with the fast ion conductor phase, is determined by an increase in the average potential energy during the heating of the crystal, and where the msd of the anion reaches

(a) A300 1C - 1C salt

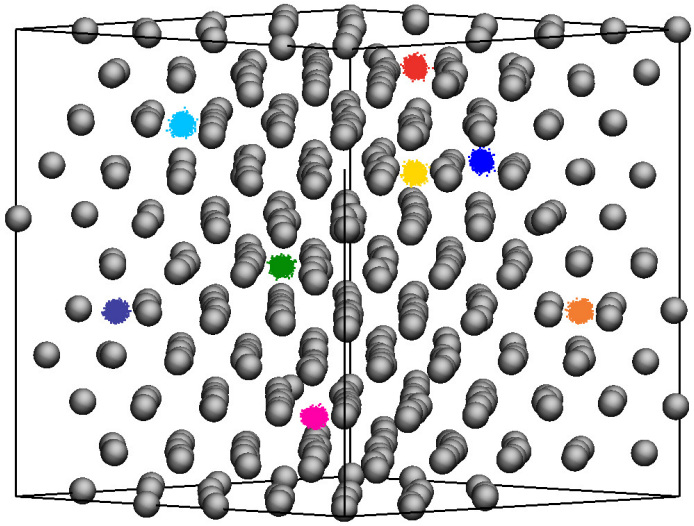

(b) A300 2L67-22 - 1C salt

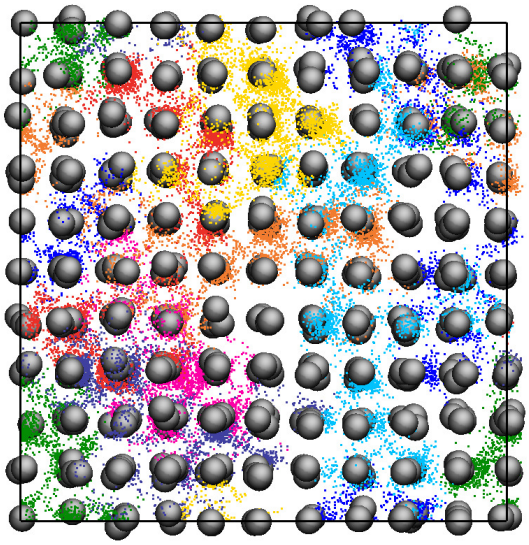

(c) A300 2L67-26 - 1C salt

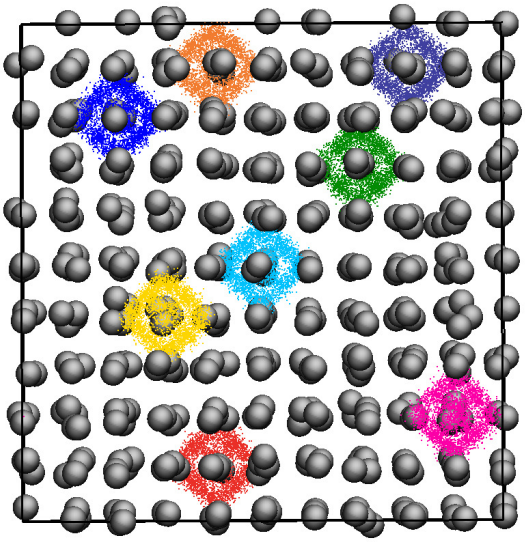

Figure 4.9: Anion motion in three salts with a size ratio of 3:1. The grey spheres (cation centers) and simulation box boundaries are shown for one instant in the trajectory. The sets of coloured points mark the positions of eight different anions on 1.0 ps intervals over the 4.0 ns trajectory. Each of these configurations are at 550 K, which is T_s for the salts shown in (b) and (c).

a constant value within about 100 ps and is significantly larger than that of the cation.

The different ion dynamics between the crystalline phase, fast ion conductor phase, and plastic crystal phase for three A300 salts are shown in Fig. 4.9. The pictures show traces of the coordinates of eight anions over the 4.0 ns simulations at $T = 550$ K. For all three salts, the fcc lattice of cation centers (grey spheres) and the simulation cell boundaries are drawn at one instant in the trajectory. The positions of eight anions are shown as points in different colours over the entire 4.0 ns trajectory, and capture the anion paths through the solid. We have not shown the off-center cation sites in (b) and (c) for simplicity. The figures were generated from heating prepared crystals (a) NaCl, (b) 111_n, and (c) 111_n, where the cations in (b) and (c) have rearranged into an fcc lattice.

At 550 K, the A300 1C - 1C salt is well below its melting temperature (T_s = 1100 K) and is a NaCl solid. Over the course of the simulation trajectory, the anions vibrate around their lattice positions, as shown in Fig. 4.9(a). The simulation cell is shown on an angle otherwise the anion positions would be obscured by the cations. The salts shown in (b) and (c) show very different types of anion motion and premelting behaviour. The cations only differ by the charge displacement distance, and T_s for both salts is 550 K. In Fig. 4.9(b), the A300 2L67-22 - 1C salt, the anions are moving through the cation lattice and are not localized. In contrast to Fig. 4.9(b), the A300 2L67-26 - 1C salt in (c) shows that the anions do not travel through the cation lattice; instead, they remain localized around a single cation. The intermediate phase between the solid and liquid for this salt is characterized by rotating ion pairs (plastic crystals).

The A267 and A300 series of salts are insulators when d is small (crystalline) and very large (plastic crystals). The salts with large size ratios and d that are not bound tightly enough to become plastic crystals become fast ion conductors.

The radial distribution functions (rdfs) for the A300 series of salts at $T =$ 550 K are shown in Fig. 4.10. The fcc cation lattice is maintained for all of the salts, as shown in the CM - CM rdfs in Fig. 4.10(b). The peaks become broader and shift to the right as d increases because the salts are closer to their melting points. The sets of rdfs involving the anion center, AM, transform from solid-like to liquid-like as d increases. The first peaks in the CM - AM and CC - AM rdf series shift to shorter distances as d increases, which is consistent with development of directional ion pairs, as noted earlier in Chapter 3. For the fast ion conductors ($d = 18$ and 22), the first peaks at short distances in the CC - AM rdfs [Fig. 4.10(d)] indicate that on average, the anions are paired with cations. However, the time-averaged rdfs do not provide any insights into the longevity/lifetime of any particular cation-anion pair. Likewise, at $d = 26$, the rdfs offer no insight that the same cation-anion pairs are left intact for the entire simulation and are rotating as ion pairs. The ion dynamics in the fast ion conductor and plastic crystal phases are an area worthy of further study.

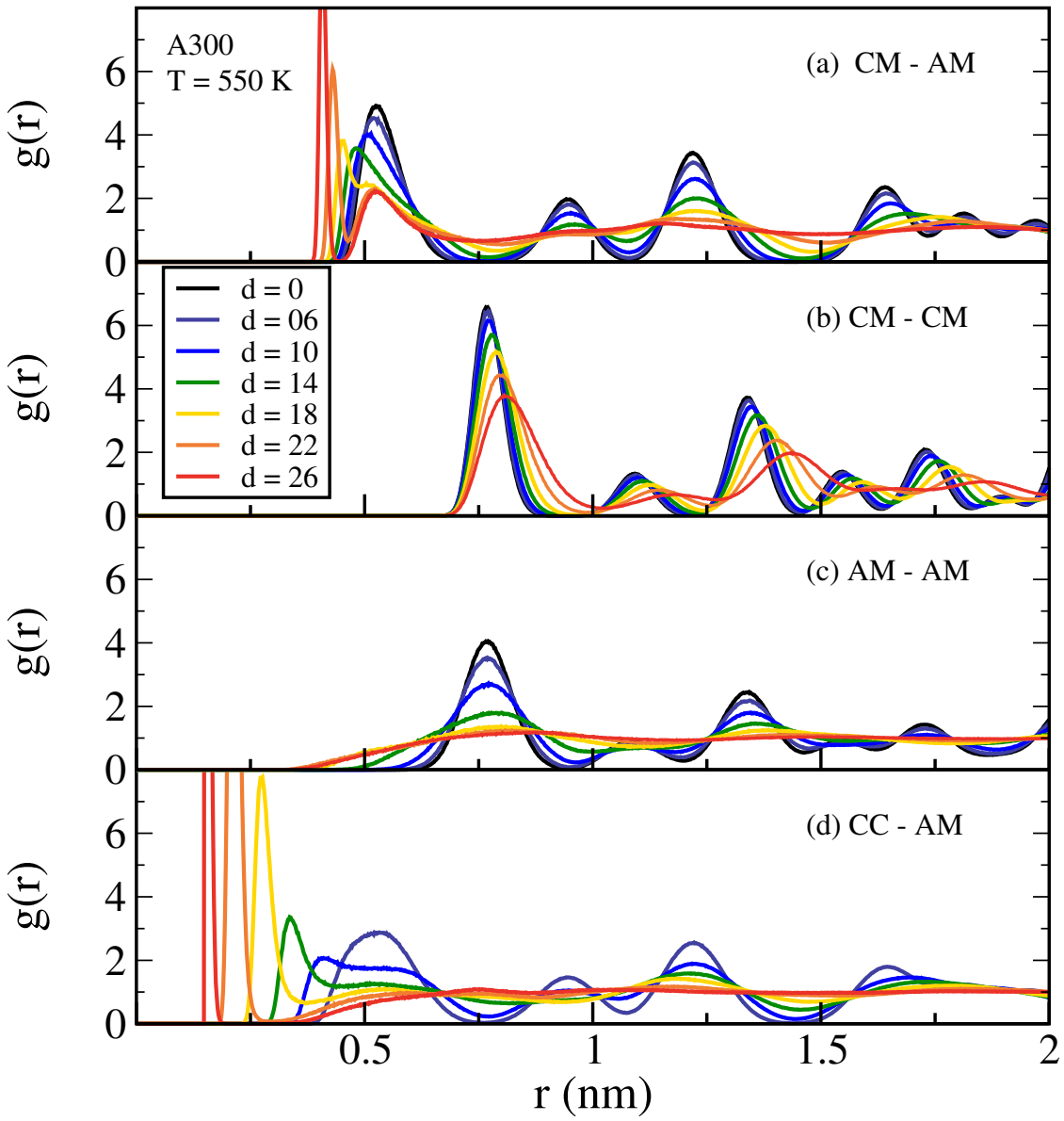

Figure 4.10: Radial distribution functions for the A300 series of salts. In (a-c), the rdfs for small d are for a NaCl structure. As d increases, the rdfs involving the anion center (AM) flatten while the cation centers remain on the fcc lattice. In (d), the first CC - AM peak shifts to shorter distances and becomes more intense as d increases. For $d = 22$ and 26, the time-average structural properties cannot reveal that the ion dynamics in these two salts are very different.

4.5 Chapter Summary

We have established the melting point trends of a large set of coarse grain model salts considering the effects of the ion size ratio, absolute ion sizes, and cation charge distribution. When the $\sigma_{\pm}$ distance is constrained (Set A) and d is small, the melting point trends reflect changes in the crystal structures. At large d, the melting points are nearly constant and show little influence from crystal structure or size ratio. When σ_{-} is fixed and σ_{+} increases (Set B), the melting point trends of the 1C - 1C salts decrease monotonically. The trends across the 2L67 - 1C salts in Set B highlight the conversion between the two influences we consider, the ion sizes and directional ion pairing.

In addition to identifying melting point trends, we find rich solid-phase behaviours that applies for both sets of salts. Across all size ratios, cations with small d are able to reorient with ease in the crystal. At low size ratios and small cation charge displacements, the salts freeze as CsCl solids. At low size ratios with 2/3 of the cation charge far enough off-center, the salts become trapped in glassy states when cooled and we find that the underlying crystal structure is orientationally ordered. As we increase the size ratio, the salts freeze as NaCl solids. At large size ratios and large d, the salts display two types of premelting transitions. The salts with large d melt from fast ion conductor phases where the smaller anions move through an fcc cation lattice, and the salts with the largest d considered here melt from a plastic crystal phases composed of ion pairs rotating on an fcc lattice.

Although the solid types are consistent across Set A and B, the melting point trends are not. The simple models are sensitive to the different length scales and produce different melting point trends.

Chapter 5

Cation Charge Geometry: Size Symmetric 3s - 1C Salts

5.1 Overview

The salts considered in this chapter are an elaboration on the 2L - 1C salts studied in Chapter 3. We redistribute the cation charge over three interaction sites instead of two, while the anion remains a 1C ion. The three site ion geometries are defined in Chapter 2.1. In the first set, we consider cations with the unit charge distributed evenly over the three interaction sites (3s33 ion geometry). In the second set, the cations have an uneven charge distribution (3s67 ion geometry) where one off-center charge site (CC1) carries 2/3 of the charge and the other off-center charge site (CC2) carries the remaining 1/3 of the charge. We only consider $d = 18$ for these salts because we are interested in isolating the influence of θ, the angle formed by the three interaction sites, CC1-CM-CC2, rather than focusing on the displacement distance.

5.2 Melting Point Results

The 3s33 - 1C salts have the cation charge evenly distributed over three interaction sites. All of the 3s33 - 1C salts spontaneously crystallize during the hysteresis cycle. One salt, the 3s(60)33 - 1C salt, becomes trapped in a "glassy" state upon cooling, but spontaneously crystallizes during the heating part of the hysteresis cycle. The 3s33 - 1C salts all crystallize as CsCl crystals where the cations are orientationally disordered.

The hysteresis plots of six 3s - 1C salts are shown in Fig. 5.1. The first column includes the hysteresis plots of three 3s33 - 1C salts with $\theta = 90°$, 135°, and 180°. Increasing θ does not influence the shape of the 3s33 - 1C hysteresis loops as much as varying d did in the 2L - 1C salt series. The value of $\Delta_{\text{fus}}\bar{U}$ increases slightly and the thermal bounds on the hysteresis (T_- to T_+) are consistently separated by about 450 K to 500 K. The change in melting temperature ranges (T_s to T_l) increases by about 350 K as θ increases for the 3s33 - 1C salts, from $T_s = 800$ K for the $\theta = 0°$ (2L67-18 - 1C) salt to $T_s = 1150$ K for the $\theta = 150°$ salt.

The 3s67 - 1C salts, with an uneven charge distribution on the cation, show more pronounced changes with increasing θ. The second column of hysteresis plots in Fig. 5.1 are for the 3s67 - 1C salts. Of the seven 3s67 - 1C salts, three of them (with $\theta \geq 135°$) spontaneously crystallize into CsCl structures upon cooling. The other four of the 3s67 - 1C salts (with $\theta \leq 120°$) become trapped in "glassy" states upon cooling. Two of those four salts, with $\theta = 105°$ and 120°, crystallize upon heating.

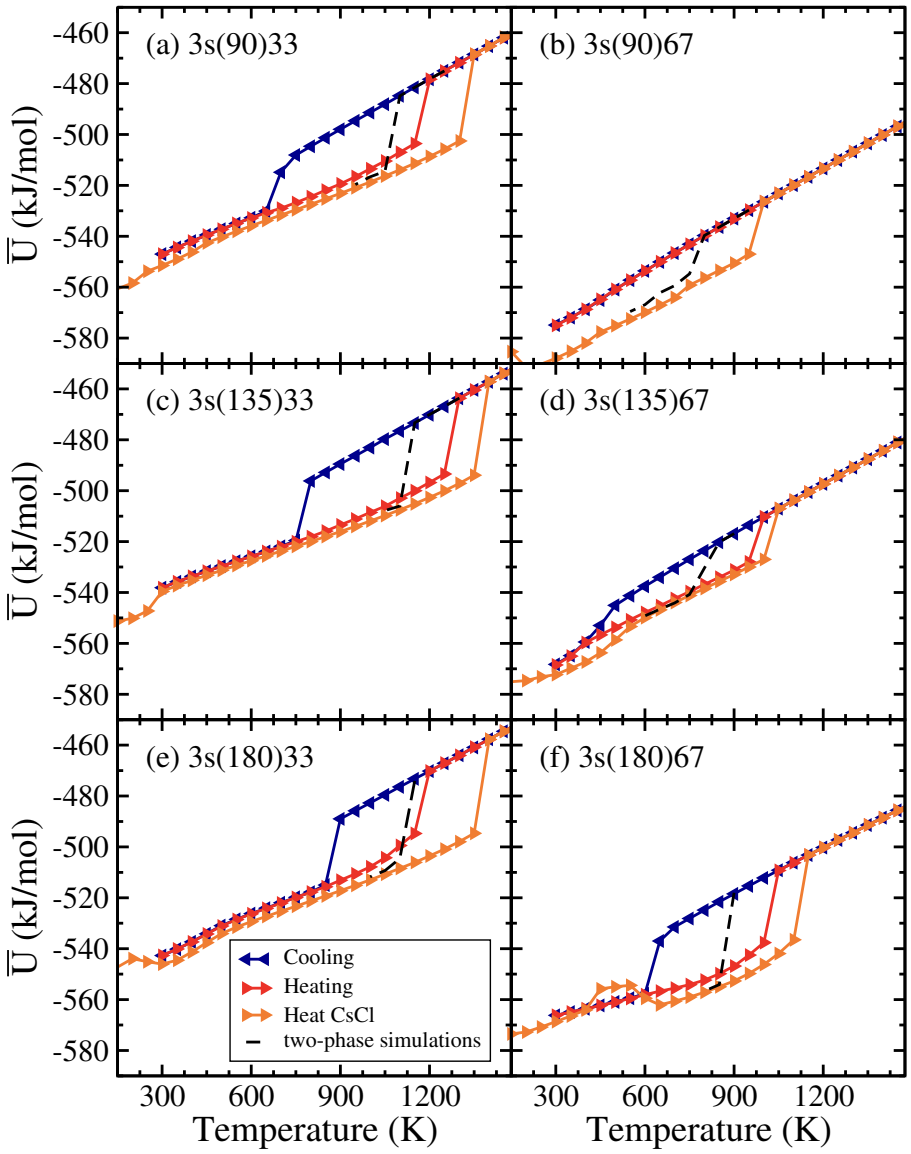

Figure 5.1: The hysteresis loops of six 3s - 1C salts. All of the salts shown crystallize as CsCl solids except the 3s(90)67-18 - 1C salt shown in (b) which vitrifies upon cooling.

Across the rows in Fig. 5.1, the θ values are constant. In the hysteresis plots with constant θ, the redistribution of 1/3 of the charge on the cation decreases average potential energies of both phases and the melting temperatures by about 300 K. The magnitude of the T_s decrease is consistent with the work in Chapter 3, where the 2L33-18 - 1C has $T_s = 1100$ K and the 2L67-18 - 1C salt has $T_s = 800$ K.

For all of the 3s - 1C salts, we prepared and heated a CsCl crystal until it melted. The CsCl structure is likely the most stable solid for these size-symmetric salts when the cations are free to reorient, a condition that is most likely satisfied near the melting transition. At lower temperatures, the CsCl structure might not be the most stable, especially for the 3s67 - 1C salts with $\theta \leq 135°$. For the 2L - 1C salts studied in Chapters 3 and 4, when we heated crystal structures that were not the most stable, the plots of the average potential energies against temperature were not smooth until the crystal rearranged or the cations gained enough thermal energy to reorient. We see similar behaviour for $\bar{U}_{\mathrm{CsCl}}(T)$ at low temperatures for the 3s67 - 1C salts with $\theta \leq 135°$. In Fig. 5.1(d), the cations in the CsCl crystal undergo rotational relaxations between 300 K and 550 K, after which $\bar{U}_{\mathrm{CsCl}}(T)$ stabilizes. The fluctuations in $\bar{U}_{\mathrm{CsCl}}(T)$ at low temperature suggests that the CsCl structure may be metastable when the cations lack the thermal energy to reorient.

The 2L100-18 - 1C salt studied in Chapter 3 would correspond to 3s(0)67-18 - 1C, and melts directly from the orientationally ordered 111_n crystal structure. It is reasonable to expect, then, that some of the salts with small θ would also have orientationally ordered crystal structure(s). However, we have not explored the crystal structure possibilities as rigorously as we did with the 2L - 1C salts.

The properties of the 3s - 1C salts are presented in Table 5.1. We observe similar trends in the salt properties of both sets. As θ increases, the solid densities are largely unaffected whereas the densities of the liquids generally decrease. Also as θ increases, T_s, $\bar{U}_s(T_s)$, and $\Delta_{\text{fus}}\bar{H}$ generally increase. The 3s(180)67-18 - 1C salt is an exception to the $\bar{U}_s(T_s)$ and $\Delta_{\text{fus}}\bar{H}$ trends. The linear charge arrangement permits both off-center cation sites to interact favourably with anion neighbours, stabilizing the orientationally ordered crystal.

Table 5.1: Properties of the 3s - 1C salts. The cation geometry is specified by the charge distribution and angle formed by the interaction sites, CC1-CM-CC2. The definitions of the rest of the properties are consistent with Tables 3.1, 4.1, and 4.2.

Cation Type	θ (degrees)	T_s (K)	$\bar{\rho}^*(s)$ —	$\bar{\rho}^*(l)$ —	$\bar{U}_s$ kJ/mol	$\Delta_{\text{fus}}\bar{H}$ (kJ/mol)
3s33-18	60	950	1.115	0.909	-526	23
	90	1050	1.102	0.872	-516	28
	105	1050	1.104	0.870	-514	29
	120	1100	1.093	0.851	-509	31
	135	1100	1.095	0.850	-507	31
	150	1150	1.086	0.831	-505	33
	180	1100	1.103	0.851	-508	32
3s67-18	60	600	1.177	1.044	-581	12
	90	750	1.145	0.978	-559	16
	105	800	1.099	0.957	-547	14
	120	800	1.130	0.956	-544	17
	135	800	1.106	0.955	-538	15
	150	850	1.093	0.935	-536	18
	180	850	1.112	0.929	-555	33

A summary of the five transition-related temperatures for both sets of 3s - 1C salts is given in Fig. 5.2. We have included the 2L67-18 - 1C and 2L100-18 - 1C salts as the $\theta = 0°$ cases. In both sets, the influence of θ on the melting point is small when $\theta \geq 105°$. When $\theta \leq 90°$, the localization of charge on one side of the cation affects the solid-liquid transition. When θ is small, the cation can form a directional ion pair with one anion, much like the 2L - 1C salts studied earlier.

Both $\theta = 0$ cases, the 2L67-18 - 1C and 2L100-18 - 1C salts, vitrify. The 3s(60)33-18 - 1C salt spontaneously crystallizes, whereas the 3s(60)67-18 - 1C salt vitrifies. The melting point range of the $\theta = 0$ case (2L100-18 - 1C salt) is for the 111_n structure. The melting point of the 3s(60)67-18 - 1C salt in a CsCl structure is 200 K lower, which may be because the salt has an orientationally ordered crystal structure with a slightly higher melting point.

The 3s67-18 - 1C salts vitrify when $\theta \leq 90°$. When $\theta \geq 105°$, the cations are more likely to have favourable interactions with multiple anions at once. The cation interacting favourably with more than one anion is likely one reason why the 3s67-18 - 1C salts with $\theta \geq 105$ spontaneously crystallize.

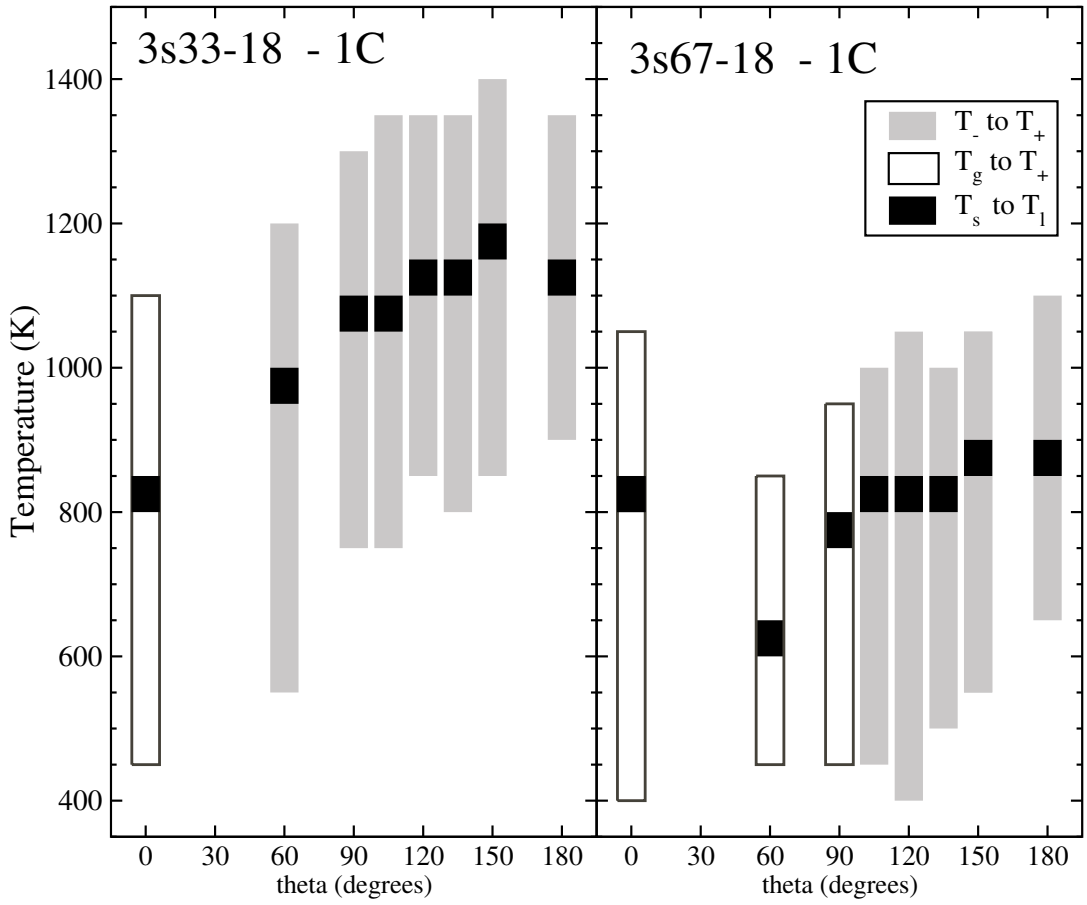

Figure 5.2: The five transition-related temperatures for the 3s - 1C salts. The salts with uneven cation charge distribution (3s67 - 1C) have lower melting points than those with even cation charge distribution (3s33 - 1C). Within each set, the melting points of the 3s - 1C salts with $\theta \leq 90°$ vary more than the salts with $\theta \geq 105°$. Once $\theta \geq 105°$, the melting points increase slightly as the angle between the off-center charge sites increases.

5.3 Chapter Summary

We have shown that introducing a third interaction site on the cation that bears 1/3 of the unit charge has the greatest influence on the melting temperature when the other 2/3 of the charge is off-center and the CC1-CM-CC2 angle, θ, is less than 90°. Once $\theta \geq 105°$, varying θ has a minor influence on the melting point. At large θ, the off-center cation sites can interact favourably with multiple anions which reduces the tendency to form discrete ion pairs.

As with the 2L - 1C salts, the crystal structures of the 3s - 1C salts is strongly dependent on whether the cations are able to reorient. Most of the 3s - 1C salts crystallize as CsCl solids. The cations of the 3s33 - 1C salts are able to reorient and the CsCl structure is orientationally disordered. The cations of the 3s67 - 1C salts show a "transition" of sorts. Cations with small angles ($\theta \leq 90°$) vitrify, likely with an underlying orientationally ordered crystal structure, whereas cations with large angles ($\theta \geq 105°$) crystallize as CsCl solids. The cations with a linear arrangement of interaction sites form an orientationally ordered CsCl crystal.

Chapter 6

Conclusion

6.1 Analysis Summary

The work presented in this thesis is a systematic investigation into how the physical attributes of model salts affect the melting temperature at $P = 1$ bar. We consider how the solid and liquid phases are affected by the ion charge distributions, the ion size ratios, the ion sizes, and the ion symmetries by studying the salt properties using a series of NPT molecular dynamics simulations. The simulation approach minimizes the hysteretic effects around the phase transition. The melting point ranges (T_s to T_l) of each salt are limited to 50 K, which is sufficiently accurate for our aim of establishing melting point trends over large sets of simple model salts.

In Chapter 3, we determine how distributed cation charge reduces the melting points of 2L - 1C salts. Redistributing the cation charge can reduce the melting point by over 50%, compared to the charge-centered case. Kobrak and Sandalow's notion of the charge arm[62] is a useful descriptor for correlating the melting points of the

model salts (Fig. 3.9). Moving a fraction of the cation charge off-center reduces the enthalpy of the liquid more than that of the solid, resulting in lower melting points. At large charge arms, the ions form strong, directional ion pairs and the liquids tend to vitrify. A crystal structure that accommodates ion pairs, the orientationally ordered 111_n structure shown in Fig. 3.3), has a lower enthalpy than the vitreous states.

In Chapter 4, the ion size ratios and absolute ion sizes are varied for the 2L - 1C salts. The size ratios are varied between 1:1 and 3:1 in two ways. In the first set, Set A, the distance between the cation and anion centers is fixed ($\sigma_{\pm} = 0.50$ nm, Set A), while the relative sizes of the ions is varied. The melting points do not vary much for the Set A 1C - 1C salts, dropping by 150 K between a 1:1 and 3:1 size ratio, although changes in the melting point trends do contain signatures of the stable crystal structure changing from CsCl to NaCl. Once part of the cation charge is moved off-center, the melting point decreases (as in Chapter 3). The melting point trends of the Set A 2L - 1C salts also show signs of the underlying crystal structure changing with size ratio. At large cation charge displacements ($d = 26$), the melting points of the salts show almost no variation between size ratios of 1.33:1 and 3:1. Only the A200 2L67-26 - 1C salt has a slightly higher (50 K) melting point range.

In the second set, Set B, the size ratios are varied by keeping the anion size fixed while increasing the size of the cation ($\sigma_{-} = 0.50$ nm). This case is more practical for representing real ionic liquids. In Set B, the charge-centered salts show a larger decrease in the melting point trends due to weaker electrostatic interactions. Unlike the Set A 1C - 1C series, the Set B 1C - 1C salt series does not show signs of different crystal structures affecting the melting point. Including the cation charge displacement in Set B reveals the subtle interplay between directional

ion pairs (due to cation charge displacement) and ion sizes on the melting point. The charge-centered salts in Set B provide an upper bound on the melting points, which decreases monotonically with increasing size ratio. Once part of the cation charge is moved off-center, the melting point trends change (no longer monotonic), revealing some signs of crystal structure dependence akin to the trends established in Set A. The salts with the largest d considered in each size ratio up to 2:1 have consistent melting point ranges, between 550 K and 600 K, as in Set A. As in Set A, the salts with large size ratios and large d show premelting transitions. Of all the salts considered in this thesis, the B300 2L67-50 - 1C and B300 2L67-58 - 1C salts have the lowest melting point ranges, both between 450 and 500 K, with the salts showing premelting transitions near 350 K and 300 K, respectively.

The compounding effects of size ratio and charge displacement also change the ion dynamics in the solids. The salts with size ratios of 2.67:1 and 3:1 show premelting transitions for salts with large d. The A267 and A300 salts with the largest d cations become plastic crystals before melting, where ion pairs rotate about fcc lattice positions. The salts with slightly smaller cation charge displacements become fast ion conductors, where the smaller anions move through fcc lattices of cations. Unlike typical fast ion conductors, the phase found here is not induced by ion size differences alone, but by the combination of disparate ion sizes and cation charge displacement.

In Chapter 5, the cation charge is distributed over three sites instead of two, and find that θ, the angle made by the CC1-CM-CC2 interaction sites on the cation, is a minor influence on the melting point. Two different cation charge distributions are considered. The unit charge is evenly distributed in the series of 3s33 cations, where each interaction site carries 1/3 of the unit charge. In the 3s67 cations, the

charge is distributed unevenly; the two off-center sites carry 2/3 and 1/3 of the unit charge and the cation center is uncharged. For both sets of 3s - 1C salts, the largest melting point reduction occurs when $\theta \leq 90°$. In the 3s33 - 1C series of salts, the melting point of the 3s(60)33-18 - 1C salt is 150 K lower than the 3s(180)33-18 - 1C salt. In the 3s67 - 1C series of salts, the melting point of the 3s(60)67-18 - 1C salt is 250 K lower than the 3s(180)67-18 - 1C salt. In both sets of 3s - 1C salts, once $\theta \geq 105°$, the melting points increase only slightly as θ approaches 180°.

This work is a broad survey of coarse grain model salts and their melting point trends.

6.2 Connection with Experimental Work

While we are interested in isolating the impact on the melting point trends of coarse grain model salts, it is insightful to see how well our results compare with experimentally observed melting point trends. We compare our salts to a set of alkyl-substituted ammonium bromide salts.

We take NH_4Br as the reference salt, which has a normal melting point of 725 K and is somewhat analogous to the A100 1C - 1C salt. The NH_4^+ and Br^- ions have centered (or symmetrically distributed) charges, similar sizes, and are spherical (or nearly so). The series of tetraalkylammonium bromide salts are cast into the place of the 1C - 1C salts in size Set B (in Chapter 4), where the anion is fixed (Br^-) and the cation increases in size. The length of the alkyl chain functions analogously to the size ratio in size Set B, where the cation size increases as the length of R_2 increases. We are assuming that three R_2 alkyl tails keep the cation shape nearly spherical, which is a reasonable assumption for chain lengths of four or

fewer carbons because there is little flexibility in the alkyl conformations.[124] Longer alkyl chains are unable to maintain a sphere-like ion shape due to the multitude of conformations available and the elongation of the ion shape.

To vary the charge distribution of the cation, we consider the homologous series of $R_1(R_2)_3NBr$ salts, where R_1 and R_2 are either hydrogen atoms or *n*-alkyl chains. The length of R_1 is varied and functions somewhat analogously to varying *d*. When R_1 and R_2 are the same length, the $d = 0$. When R_1 is shorter than R_2, *d* increases (the nitrogen atom is closer to the ion surface in one direction).

The melting points of the alkyl-substituted ammonium bromide salts are given in Table 6.1 and plotted against the length of R_2 in Fig. 6.1.

Table 6.1: Normal melting points of substituted ammonium bromide salts. The series of $R_1(R_2)_3NBr$ salts include size effects and charge asymmetry. The bromide salts where the cation has *n*-butyl chains or shorter are comparable to the size Set B salts from Chapter 4. The size ratios were calculated from ionic radii.[125,126] The melting points that are listed as sourced from Material Safety Data Sheets (MSDS) are from Sigma Aldrich.

Cation		Melting Point	Cation:Br^-	Source
R_1	R_2	(K)	Size Ratio	
H	H	725	0.93	MSDS
C_2H_5	H	434		[127]
n-C_3H_7	H	456		[127]
n-C_7H_{15}	H	490		[127]
CH_3	CH_3	573	1.77	MSDS
C_2H_5	CH_3	603		[53]
n-C_3H_7	CH_3	513		[53]
n-C_4H_9	CH_3	468		[53]
n-C_7H_{15}	CH_3	455		[55]
CH_3	C_2H_5	573		[53]

Continued on next page...

Table 6.1: (Continued)

Cation		Melting Point	Cation:Br^-	Source
R_1	R_2	(K)	Size Ratio	
C_2H_5	C_2H_5	558	2.12	MSDS
n-C_4H_9	C_2H_5	486		[55]
n-C_5H_{11}	C_2H_5	419		[53]
n-C_7H_{15}	C_2H_5	393		[53]
n-C_3H_7	n-C_3H_7	543	2.53	MSDS
n-C_4H_9	n-C_3H_7	494		MSDS
CH_3	n-C_4H_9	393		[53]
n-C_4H_9	n-C_4H_9	393	2.75	[53]

The melting points of the tetraalkylammonium bromide salts, shown in Fig. 6.1 with black borders, decrease monotonically with increasing alkyl chain length, which is similar to the trends observed for the series of 1C - 1C salts in Set B of Chapter 4. The cation:anion size ratios span the same region explored in Chapter 4 where ammonium bromide and tetrabutylammonium bromide have approximate size ratios of 0.93 and 2.75, respectively.

For the cations where $R_1 \neq R_2$, the ion size, shape, mass, mass distribution, and charge distribution change with respect to the tetraalkyl substituted cation. The normal melting points of ethylammonium bromide (T_m = 434 K) and n-propylammonium bromide (T_m = 456 K) are lower than that of ammonium bromide (T_m = 725 K) by 250-300 K. The changes in ion size, shape, and charge distribution lower the melting point relative to ammonium bromide. Following the R_1=ethyl (green blocks), propyl (yellow blocks), and butyl (red blocks) across in-

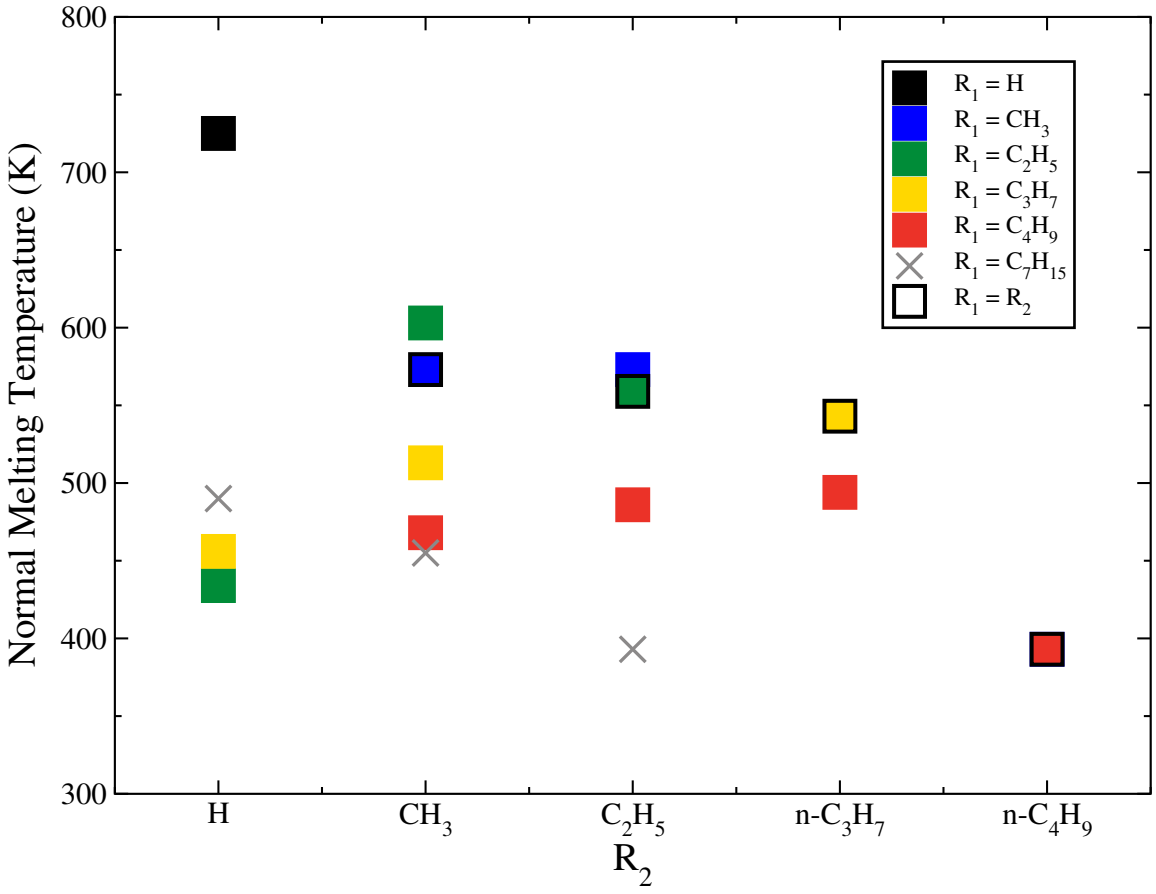

Figure 6.1: Plot of the normal melting points of $R_1(R_2)_3NBr$ substituted ammonium bromide salts. The melting points are plotted as a function of the trialkyl substituents on the cation. The cation sizes increase from left to right.

creasing R_2 length in Fig. 6.1 gives a generally increasing melting point trend until the tetraalkylammonium bromide salts are reached. The melting points of the salts with R_1=butyl cations decrease from R_2=*n*-propyl to the tetrabutylammonium bromide salt, likely due to size effects.

Three points are included in Fig. 6.1 for R_1=*n*-heptyl, which are marked with grey crosses. The trends for these salts do not follow the trends from Chapter 4, because the ion shapes are far from spherical and the ion sizes/size ratios are outside the region studied.

The melting point trends of the coarse grain model salts studied in this thesis can be connected to those of a series of real salts, shown here for example alkyl substituted ammonium bromide salts. The connection demonstrates the value of studying coarse grain salts and that the general insights are transferable to real salts, even though the coarse grain cations are much simpler than the ammonium cations and the coarse grain anions are much larger than bromide ions.

6.3 Future Work

This project has fostered some ideas for new research questions that are adjacent to the current project. The work in Chapter 3 raises interesting questions about the rest of the phase diagram of these simple model salts. For example, how do the triple points and critical points vary with cation charge displacement? Ganzenmüller and Camp have identified the critical points of similar simple model salts.[57] Additionally, it would be interesting to determine where the *s*-*s* transitions between the ordered and disordered solids occur.

In earlier work,[92] the dynamical properties of molten model salts under NVT

conditions at $T = 1200$ K were studied. It would be interesting to establish trends for dynamic properties like diffusion, viscosity, and electrical conductivity, at a consistent temperature like 100 K above each salt's melting point. A detailed profile of the directional ion pairing (formation/degradation rates, longevity of ion pairs) at or just above the melting point would also be insightful. The work done on these simple models[60,61,92,128] has reinforced the importance of directional ion pairing on the dynamic and thermodynamic properties.

The work discussed in Chapter 4 generated some interesting questions. It would be of interest to explore the fast ion conductor phases of the ions with large size ratios and large cation charge displacements. One could characterize the premelting solid phase using MD simulations (with more frequent output) to calculate the current-current correlation functions and the electrical conductivities. It would also be interesting to consider a series of A300 salts with smaller d increments to refine the location of the transition from a fast-ion conductor premelting phase to a plastic crystal premelting phase across salt models. Studying these properties might give some further insight into features of molecular ionic salts that make them attractive as solid state electrolytes.[80]

Also from Chapter 4, the transition from a fast-ion conductor phase to a plastic crystal phase might offer some interesting insights into the heterogeneous dynamics found in the liquid phase of ionic liquids. We have demonstrated that the anion dynamics in the solids are sensitive to a change of 0.04 nm in the cation charge distribution. If a cation with conformational flexibility could sample molecular configurations with charge displacements between these two cases [A300 salts with $d = 22$ (fast ion conductor) and $d = 26$ (plastic crystal)], then the salt would have a mix of paired (localized) and unpaired (delocalized) ions, and might show dynamic

heterogeneity in the solid. And if, (and this is a big if) similar behaviour is observed in the liquid, then dynamic heterogeneities would be expected, and would act as a signature of the anions responding to different cation conformations. It would be interesting to study the liquid dynamics of neat molten salts just above the melting point, and to contrast the dynamics with cases where the single cation type was replaced with a binary or ternary mixture of closely-related cation types to emulate a distribution of cation conformations.

The MD method used to establish the melting points was sufficient for establishing the melting point trends across a set of salts, but lacks precision due to a dependence on the barostat in the two-phase simulations. There are two related topics that would merit further investigation. It might be useful to calculate the melting point of the 1C - 1C salts in this work using a more rigorous free energy method. Making a comparison with an "exact" method might give insight into how to better select barostat parameters. A second, related project would aim to quantify, minimize, or eliminate the melting point sensitivity to the barostat parameters, which would likely involve larger system sizes.

The coarse grain models employed here reproduce some interesting aspects of ILs. There are many possible ways to make the simple salts more realistic, and also other ways to explore theoretically interesting model salts. In order to make the ion models more realistic, one could

- explore different ion shapes,
- use a polarizable model,
- consider ions with internal flexibility (multiple conformations), or
- create cation-anion pairs using ion topologies that resemble well-studied ILs.

The exploration of different ion shapes is a natural extension of this work. Crystal structure determination of particles with various shapes has been taken up by Dijkstra and coworkers.[114,129–134] Research on the *s*-*l* transitions of ions shaped as fused spheres, prolate/oblate ellipsoids, and discs and the properties of such shapes when paired with a spherical counterion would be particularly insightful. It would also be interesting to add (flexible) chains of LJ spheres to the ions studied here to mimic alkyl tails of various lengths. In the present work, many different solidification behaviours are observed, from crystallization as "regular" crystals, crystals where the cation reoriented within the solid, plastic crystals, and fast ion conductors, to vitrification. Liquid crystal phases are notably absent, but the ions studied here are not aspherical enough to form liquid crystal phases. A similar approach could be used to categorize and characterize simple models for liquid crystal ionic liquids.

In terms of adapting the models for theoretical purposes, one could

- systematically reduce the charge magnitudes on the ions from ± 1 e to about ± 0.6 e. Reducing the magnitude of the ion charge (charge scaling) has been explored as a way of reconciling dynamical property differences between simulations and experiments,[12,58,65,135]
- vary the LJ interaction strength ε in two ways, (a) vary the magnitude and (b) explore ions with different size ratios keeping ε per volume or surface area constant,
- vary the ion topologies by adding more interaction sites.

A practical project could look at the mapping between the trends found here and homologous series of ILs, or making comparisons with experimental work.

Bibliography

[1] H. Weingärtner, Angew. Chem., Int. Ed. **47**, 654 (2008).

[2] S. Jayaraman and E. J. Maginn, J. Chem. Phys. **127**, 214504 (2007).

[3] N. V. Plechkova and K. R. Seddon, Chem. Soc. Rev. **37**, 123 (2008).

[4] R. Hayes, S. Imberti, G. G. Warr, and R. Atkin, Phys. Chem. Chem. Phys. **13**, 3237 (2011).

[5] A. R. Katritzky, R. Jain, A. Lomaka, R. Petrukhin, M. Karelson, A. E. Visser, and R. D. Rogers, J. Chem. Inf. Comput. Sci. **42**, 225 (2002).

[6] E. W. Castner and J. F. Wishart, J. Chem. Phys. **132**, 120901 (2010).

[7] I. Krossing, J. M. Slattery, C. Daguenet, P. J. Dyson, A. Oleinikova, and H. Weingärtner, J. Am. Chem. Soc. **128**, 13427 (2006).

[8] B. L. Bhargava, S. Balasubramanian, and M. L. Klein, Chem. Commun. **29**, 3339 (2008).

[9] E. J. Maginn, J. Phys.: Condens. Matter **21**, 373101 (2009).

[10] U. Preiss, S. Bulut, and I. Krossing, J. Phys. Chem. B **114**, 11133 (2010).

[11] S. Tsuzuki, H. Tokuda, K. Hayamizu, and M. Watanabe, J. Phys. Chem. B **109**, 16474 (2005).

[12] Y. Wang, W. Jiang, T. Yan, and G. A. Voth, Acc. Chem. Res. **40**, 1193 (2007).

[13] A. R. Katritzky, A. Lomaka, R. Petrukhin, R. Jain, M. Karelson, A. E. Visser, and R. D. Rogers, J. Chem. Inf. Comput. Sci. **42**, 71 (2002).

[14] J. F. Brennecke and E. J. Maginn, AIChE J. **47**, 2384 (2001).

[15] M. N. Kobrak, Adv. Chem. Phys. **139**, 85 (2008).

[16] E. A. Turner, C. C. Pye, and R. D. Singer, J. Phys. Chem. A **107**, 2277 (2003).

[17] K. Marsh, J. Boxall, and R. Lichtenthaler, Fluid Phase Equilib. **219**, 93 (2004).

[18] R. D. Rogers and K. R. Seddon, Science **302**, 792 (2003).

[19] M. J. Earle, S. P. Katdare, and K. R. Seddon, Org. Lett. **6**, 707 (2004).

[20] C. Chiappe and D. Pieraccini, J. Phys. Org. Chem. **18**, 275 (2005).

[21] M. J. Marczewski, B. Stanje, I. Hanzu, M. Wilkening, and P. Johansson, Phys. Chem. Chem. Phys. **16**, 12341 (2014).

[22] C. P. Fredlake, J. M. Crosthwaite, D. G. Hert, S. N. V. K. Aki, and J. F. Brennecke, J. Chem. Eng. Data **49**, 954 (2004).

[23] M. E. Valkenburg, R. L. Vaughn, M. Williams, and J. S. Wilkes, Thermochimica Acta **425**, 181 (2005).

[24] A. S. Arico, P. Bruce, B. Scrosati, J.-M. Tarascon, and W. van Schalkwijk, Nat. Mater. **4** (2005).

[25] J. F. Wishart, Energy Environ. Sci. **2**, 956 (2009).

[26] S. Aparicio, M. Atilhan, and F. Karadas, Ind. Eng. Chem. Res. **49**, 9580 (2010).

[27] P. Brown, C. Butts, R. Dyer, J. Eastoe, I. Grillo, F. Guittard, S. Rogers, and R. Heenan, Langmuir **27**, 4563 (2011).

[28] P. Brown, C. P. Butts, J. Eastoe, I. Grillo, C. James, and A. Khan, J. Colloid Interface Sci. **395**, 185 (2013).

[29] C. Ye, W. Liu, Y. Chen, and L. Yu, Chem. Commun. **21**, 2244 (2001).

[30] C.-M. Jin, C. Ye, B. S. Phillips, J. S. Zabinski, X. Liu, W. Liu, and J. M. Shreeve, J. Mater. Chem. **16**, 1529 (2006).

[31] M. Palacio and B. Bhushan, Tribology Letters **40**, 247 (2010).

[32] X. Zhang, X. Zhang, H. Dong, Z. Zhao, S. Zhang, and Y. Huang, Energy Environ. Sci. **5**, 6668 (2012).

[33] T. M. Chang, L. X. Dang, R. Devanathan, and M. Dupuis, J. Phys. Chem. A **114**, 12764 (2010).

[34] F. Karadas, M. Atilhan, and S. Aparicio, Energy Fuels **24**, 5817 (2010).

[35] M. Hasib-ur Rahman, M. Siaj, and F. Larachi, Chem. Eng. Process. Process Intensif. **49**, 313 (2010).

[36] C. Wang, H. Luo, D.-e. Jiang, H. Li, and S. Dai, Angew. Chem. **122**, 6114 (2010).

[37] J. G. Huddleston and R. D. Rogers, Chem. Commun. **16**, 1765 (1998).

[38] A. E. Visser, R. P. Swatloski, W. M. Reichert, R. Mayton, S. Sheff, A. Wierzbicki, J. H. Davis, Jr., and R. D. Rogers, Chem. Commun. **1**, 135 (2001).

[39] A. E. Visser, R. P. Swatloski, S. T. Griffin, D. H. Hartman, and R. D. Rogers, Sep. Sci. Technol. **36**, 785 (2001).

[40] R. Sheldon, Chem. Commun. **23**, 2399 (2001).

[41] C. M. Gordon, Applied Catalysis A: General **222**, 101 (2001), Celebration Issue.

[42] T. Welton, Coord. Chem. Rev. **248**, 2459 (2004), Vignettes of Homogeneous Catalysis.

[43] V. I. Pârvulescu and C. Hardacre, Chem. Rev. **107**, 2615 (2007).

[44] H. Olivier-Bourbigou, L. Magna, and D. Morvan, Applied Catalysis A: General **373**, 1 (2010).

[45] M. Malvaldi and C. Chiappe, J. Phys.: Condens. Matter **20**, 035108 (2008).

[46] A.-P. Hynninen and A. Z. Panagiotopoulos, Mol. Phys. **106**, 2039 (2008).

[47] A. A. H. Pádua, M. F. Costa Gomes, and J. N. A. Canongia Lopes, Acc. Chem. Res. **40**, 1087 (2007).

[48] W. Xu, E. I. Cooper, and C. A. Angell, J. Phys. Chem. B **107**, 6170 (2003).

[49] G. Raabe and J. Köhler, J. Chem. Phys. **128**, (2008).

[50] K. Wendler, F. Dommert, Y. Y. Zhao, R. Berger, C. Holm, and L. Delle Site, Faraday Discuss. **154**, 111 (2012).

[51] A. R. Katritzky, R. Jain, A. Lomaka, R. Petrukhin, U. Maran, and M. Karelson, Cryst. Growth Des. **1**, 261 (2001).

[52] S. Trohalaki, R. Pachter, G. W. Drake, and T. Hawkins, Energy Fuels **19**, 279 (2005).

[53] D. M. Eike, J. F. Brennecke, and E. J. Maginn, Green Chem. **5**, 323 (2003).

[54] I. López-Martin, E. Burello, P. N. Davey, K. R. Seddon, and G. Rothenberg, ChemPhysChem **8**, 690 (2007).

[55] A. Varnek, N. Kireeva, I. V. Tetko, I. I. Baskin, and V. P. Solov'ev, J. Chem. Inf. Model. **47**, 1111 (2007).

[56] S. Alavi and D. L. Thompson, J. Chem. Phys. **122**, (2005).

[57] G. C. Ganzenmüller and P. J. Camp, Condens. Matter Phys. **14**, 1 (2011), Available at http://arxiv.org/abs/1202.4279.

[58] D. Roy and M. Maroncelli, J. Phys. Chem. B **114**, 12629 (2010).

[59] D. Roy, N. Patel, S. Conte, and M. Maroncelli, J. Phys. Chem. B **114**, 8410 (2010).

[60] H. V. Spohr and G. N. Patey, J. Chem. Phys. **130**, 104506 (2009).

[61] H. V. Spohr and G. N. Patey, J. Chem. Phys. **132**, 154504 (2010).

[62] M. Kobrak and N. Sandalow, Molten Salts XIV, Electrochemical Society Pennington, NJ, 2006.

[63] S. M. Urahata and M. C. C. Ribeiro, J. Phys. Chem. Lett. **1**, 1738 (2010).

[64] O. Patsahan and A. Ciach, Phys. Rev. E **86**, 031504 (2012).

[65] E. I. Izgorodina, Phys. Chem. Chem. Phys. **13**, 4189 (2011).

[66] M. G. Del Pópolo and G. A. Voth, J. Phys. Chem. B **108**, 1744 (2004).

[67] S. Zahn, J. Thar, and B. Kirchner, J. Chem. Phys. **132**, 124506 (2010).

[68] P. Wasserscheid and T. Welton, editors, *Ionic Liquids in Synthesis*, Wiley, 2006.

[69] H. Feng, J. Zhou, and Y. Qian, J. Chem. Phys. **135**, 144501 (2011).

[70] J. N. A. Canongia Lopes and A. A. H. Pádua, J. Phys. Chem. B **110**, 3330 (2006).

[71] S. Zahn, G. Bruns, J. Thar, and B. Kirchner, Phys. Chem. Chem. Phys. **10**, 6921 (2008).

[72] D. MacFarlane, P. Meakin, J. Sun, N. Amini, and M. Forsyth, J. Phys. Chem. B **103**, 4164 (1999).

[73] L. Jin, K. M. Nairn, C. M. Forsyth, A. J. Seeber, D. R. MacFarlane, P. C. Howlett, M. Forsyth, and J. M. Pringle, J. Am. Chem. Soc. **134**, 9688 (2012).

[74] D. Hwang, D. Kim, S. Jo, V. Armel, D. R. MacFarlane, D. Kim, and S.-Y. Jang, Sci. Rep. (2013).

[75] D. R. MacFarlane, J. Huang, and M. Forsyth, Nature **402**, 792 (1999).

[76] K. Matsumoto, R. Hagiwara, Z. Mazej, P. Benkič, and B. Žemva, Solid State Sciences **8**, 1250 (2006).

[77] E. W. Castner, C. J. Margulis, M. Maroncelli, and J. F. Wishart, Annu. Rev. Phys. Chem. **62**, 85 (2011).

[78] D. R. MacFarlane and M. Forsyth, Advanced Materials **13**, 957 (2001).

[79] J. M. Pringle, P. C. Howlett, D. R. MacFarlane, and M. Forsyth, J. Mater. Chem. **20**, 2056 (2010).

[80] F. Chen, S. W. de Leeuw, and M. Forsyth, J. Phys. Chem. Lett. **4**, 4085 (2013).

[81] H. A. Every, A. G. Bishop, D. R. MacFarlane, G. Oradd, and M. Forsyth, J. Mater. Chem. **11**, 3031 (2001).

[82] C. M. Gordon, J. D. Holbrey, A. R. Kennedy, and K. R. Seddon, J. Mater. Chem. **8**, 2627 (1998).

[83] J. D. Holbrey and K. R. Seddon, J. Chem. Soc., Dalton Trans. , 2133 (1999).

[84] J. D. Holbrey, W. M. Reichert, M. Nieuwenhuyzen, S. Johnson, K. R. Seddon, and R. D. Rogers, Chem. Commun. **14**, 1636 (2003).

[85] A. M. Scurto and W. Leitner, Chem. Commun. , 3681 (2006).

[86] Y. Shimizu, Y. Ohte, Y. Yamamura, K. Saito, and T. Atake, J. Phys. Chem. B **110**, 13970 (2006), PMID: 16836349.

[87] R. D. Chirico, V. Diky, J. W. Magee, M. Frenkel, and K. N. Marsh, Pure Appl. Chem. **81**, 791 (2009).

[88] L. Zheng, S.-N. Luo, and D. L. Thompson, J. Chem. Phys. **124**, 154504 (2006).

[89] Y. Zhang and E. J. Maginn, J. Chem. Phys. **136**, 144116 (2012).

[90] S. Wang, G. Zhang, H. Liu, and H. Song, J. Chem. Phys. **138**, 134101 (2013).

[91] S.-N. Luo, A. Strachan, and D. C. Swift, J. Chem. Phys. **120**, 11640 (2004).

[92] H. V. Spohr and G. N. Patey, J. Chem. Phys. **129**, 064517 (2008).

[93] Q. Yan and J. J. de Pablo, Phys. Rev. Lett. **88**, 095504 (2002).

[94] R. A. Kuharski and P. J. Rossky, J. Am. Chem. Soc. **106**, 5794 (1984).

[95] S.-N. Luo, T. J. Ahrens, T. Çağ ın, A. Strachan, W. A. Goddard, and D. C. Swift, Phys. Rev. B **68**, 134206 (2003).

[96] L. Zheng and D. L. Thompson, J. Chem. Phys. **125**, 084505 (2006).

[97] D. Van Der Spoel, E. Lindahl, B. Hess, G. Groenhof, A. E. Mark, and H. J. C. Berendsen, J. Comput. Chem. **26**, 1701 (2005).

[98] B. Hess, C. Kutzner, D. van der Spoel, and E. Lindahl, J. Chem. Theory Comput. **4**, 435 (2008).

[99] S. Pronk, S. Pll, R. Schulz, P. Larsson, P. Bjelkmar, R. Apostolov, M. R. Shirts, J. C. Smith, P. M. Kasson, D. van der Spoel, B. Hess, and E. Lindahl, Bioinformatics **29**, 845 (2013).

[100] S. Nosé, Mol. Phys. **52**, 255 (1984).

[101] S. Nosé, J. Chem. Phys. **81**, 511 (1984).

[102] W. G. Hoover, Phys. Rev. A **31**, 1695 (1985).

[103] M. Parrinello and A. Rahman, J. Appl. Phys. **52**, 7182 (1981).

[104] S. Nosé and M. Klein, Mol. Phys. **50**, 1055 (1983).

[105] U. Essmann, L. Perera, M. L. Berkowitz, T. Darden, H. Lee, and L. G. Pedersen, J. Chem. Phys. **103**, 8577 (1995).

[106] B. Hess, H. Bekker, H. J. C. Berendsen, and J. G. E. M. Fraaije, J. Comput. Chem. **18**, 1463 (1997).

[107] E. G. Noya, C. Vega, and E. de Miguel, J. Chem. Phys. **128**, 154507 (2008).

[108] C. Hardacre, J. D. Holbrey, M. Nieuwenhuyzen, and T. G. A. Youngs, Acc. Chem. Res. **40**, 1146 (2007).

[109] C. Vega, J. L. F. Abascal, C. McBride, and F. Bresme, J. Chem. Phys. **119**, 964 (2003).

[110] G. C. McNeil-Watson and N. B. Wilding, J. Chem. Phys. **124**, 064504 (2006).

[111] A. Criado, M. Jiménez-Ruiz, C. Cabrillo, F. J. Bermejo, R. Fernández-Perea, H. E. Fischer, and F. R. Trouw, Phys. Rev. B **61**, 12082 (2000).

[112] R. Rey, J. Phys. Chem. B **112**, 344 (2008).

[113] H. T. Stokes and D. M. Hatch, J. Appl. Crystallogr. **38**, 237 (2005).

[114] L. Filion and M. Dijkstra, Phys. Rev. E **79**, 046714 (2009).

[115] S. Yamanaka, T. Yasunaga, K. Yamaguchi, and M. Tagawa, J. Mater. Chem. **19**, 2573 (2009).

[116] S. Yamanaka, K. Umemoto, Z. Zheng, Y. Suzuki, H. Matsui, N. Toyota, and K. Inumaru, J. Mater. Chem. **22**, 10752 (2012).

[117] M. Bykov, E. Bykova, S. van Smaalen, L. Dubrovinsky, C. McCammon, V. Prakapenka, and H.-P. Liermann, Phys. Rev. B **88**, 014110 (2013).

[118] J. Hansen and I. McDonald, *Theory of Simple Liquids: with Applications to Soft Matter*, Elsevier Science, 2013.

[119] M. P. Allen and D. J. Tildesley, *Computer Simulation of Liquids*, Clarendon press Oxford, 1987.

[120] D. Frenkel and B. Smit, *Understanding Molecular Simulation: From Algorithms to Applications*, Computational Science Series, Elsevier Science, 2001.

[121] M. Zuriaga, M. Carignano, and P. Serra, J. Chem. Phys. **135**, 044504 (2011).

[122] D. A. Keen, J. Phys.: Condens. Matter **14**, R819 (2002).

[123] A. Fukumoto, A. Ueda, and Y. Hiwatari, J. Phys. Soc. Jpn. **51**, 3966 (1982).

[124] H. Jin, B. O'Hare, J. Dong, S. Arzhantsev, G. A. Baker, J. F. Wishart, A. J. Benesi, and M. Maroncelli, J. Phys. Chem. B **112**, 81 (2008), PMID: 18069817.

[125] D. H. Aue, H. M. Webb, and M. T. Bowers, J. Am. Chem. Soc. **98**, 318 (1976).

[126] B. Trend, D. Knoll, M. Ueno, D. Evans, and V. Bloomfield, Biophys. J. **57**, 829 (1990).

[127] J. Tsau and D. Gilson, J. Phys. Chem. **72**, 4082 (1968).

[128] E. K. Lindenberg and G. N. Patey, J. Chem. Phys. **140**, (2014).

[129] A.-P. Hynninen and M. Dijkstra, Phys. Rev. Lett. **94**, 138303 (2005).

[130] M. E. Leunissen, C. G. Christova, A.-P. Hynninen, C. P. Royall, A. I. Campbell, A. Imhof, M. Dijkstra, R. van Roij, and A. van Blaaderen, Nature **437**, 235 (2005).

[131] A. P. Gantapara, J. de Graaf, R. van Roij, and M. Dijkstra, Phys. Rev. Lett. **111**, 015501 (2013).

[132] K. Milinković, M. Dennison, and M. Dijkstra, Phys. Rev. E **87**, 032128 (2013).

[133] M. Marechal, A. Patti, M. Dennison, and M. Dijkstra, Phys. Rev. Lett. **108**, 206101 (2012).

[134] M. Dennison, K. Milinković, and M. Dijkstra, J. Chem. Phys. **137**, (2012).

[135] M. Klähn, A. Seduraman, and P. Wu, J. Phys. Chem. B **112**, 10989 (2008).

[136] D. M. Heyes, Phys. Rev. B **49**, 755 (1994).

[137] N. Galamba, C. A. Nieto de Castro, and J. F. Ely, J. Phys. Chem. B **108**, 3658 (2004).

[138] H. Lee and W. Cai, Ewald summation for Coulomb interactions in a periodic supercell, 2009, micro.stanford.edu/mediawiki/images/4/46/Ewald_notes.pdf.

[139] I. Souza and J. Martins, Phys. Rev. B **55**, 8733 (1997).

[140] S. Forrest, Science **261**, 872 (1993).

[141] D. M. Deaven and K. M. Ho, Phys. Rev. Lett. **75**, 288 (1995).

[142] D. Deaven, N. Tit, J. Morris, and K. Ho, Chem. Phys. Lett. **256**, 195 (1996).

[143] C. W. Glass, A. R. Oganov, and N. Hansen, Comput. Phys. Commun. **175**, 713 (2006).

[144] J. Niesse and H. R. Mayne, Chem. Phys. Lett. **261**, 576 (1996).

[145] J. A. Niesse and H. R. Mayne, J. Chem. Phys. **105**, 4700 (1996).

[146] A. R. Oganov and C. W. Glass, J. Chem. Phys. **124**, (2006).

[147] A. R. Oganov and C. W. Glass, J. Phys.: Condens. Matter **20**, 064210 (2008).

[148] D. C. Lonie and E. Zurek, Comput. Phys. Commun. **182**, 372 (2011).

[149] T. A. Weber and F. H. Stillinger, Phys. Rev. B **32**, 5402 (1985).

[150] W. Kob and H. C. Andersen, Phys. Rev. E **51**, 4626 (1995).

[151] J. R. Fernández and P. Harrowell, Phys. Rev. E **67**, 011403 (2003).

Appendix A

Configurational Calculations

There are elements that both programs written for this project, a molecular dynamics (MD) program and a genetic algorithm (GA), have in common. General overviews of the program structures are shown in Fig. A.1. The calculations that apply for both the GA and MD programs are described in this appendix. Specifically, the parameters and representations of the container, the details of the particle representations, and finally the techniques used to calculate the energies, forces and pressures for a single configuration are presented. These elements are consistent across both programs written for this project and are discussed together here, and are shown in purple boxes near the center of Fig. A.1.

For both programs written for this project, the energy evaluation routines used Cartesian coordinates for the particles, whereas the propagation routines (through configuration space and time) were carried out using fractional coordinates.

Details specific to the MD program are presented in Appendix B. Some of the methods used in the MD code produced for this project as well as the techniques

implemented with the Gromacs software package are noted.

Appendix C presents the specifics of the genetic algorithm and includes details about the initialization, propagation, and termination of the simulation.

A.1 Simulation Cell

The simulation cell is a parallelepiped, with the size and shape defined by three lengths and three angles. The lengths of the cell sides are a, b, c, and the three angles are α, β, and γ, which are the angles between b and c, a and c, and a and b, respectively. In a Cartesian setting, the cell boundaries are usually defined by three vectors, $\boldsymbol{a}$, $\boldsymbol{b}$, and $\boldsymbol{c}$, that are represented in a 3×3 matrix, $\boldsymbol{h}$. The nine elements in the matrix can always be reduced to 6 non-zero elements; the matrix includes redundant information. The conventional Cartesian setting of the cell is that $\boldsymbol{a}$ coincides with the positive x axis, $\boldsymbol{b}$ lies in the xy plane, and $\boldsymbol{c}$ has some component in the positive z direction,

$$\boldsymbol{h} = \begin{bmatrix} a_x & a_y & a_z \\ b_x & b_y & b_z \\ c_x & c_y & c_z \end{bmatrix} = \begin{bmatrix} a_x & 0 & 0 \\ b_x & b_y & 0 \\ c_x & c_y & c_z \end{bmatrix} = \begin{bmatrix} |\boldsymbol{a}| & 0 & 0 \\ |\boldsymbol{b}| \cos\gamma & |\boldsymbol{b}| \sin\gamma & 0 \\ |\boldsymbol{c}| \cos\beta & \frac{|\boldsymbol{c}|(\cos\alpha - \cos\beta\cos\gamma)}{\sin\gamma} & \frac{V}{|\boldsymbol{a}|\,|\boldsymbol{b}|\,\sin\gamma} \end{bmatrix} \tag{A.1}$$

where V is the cell volume.

Another approach to reduce the 9 matrix elements to 6 and eliminate the orientational dependence of the vectors is to use the metric tensor, whose elements are defined as

$$\boldsymbol{g} \equiv \boldsymbol{h}^{\mathsf{T}} \boldsymbol{h}. \tag{A.2}$$

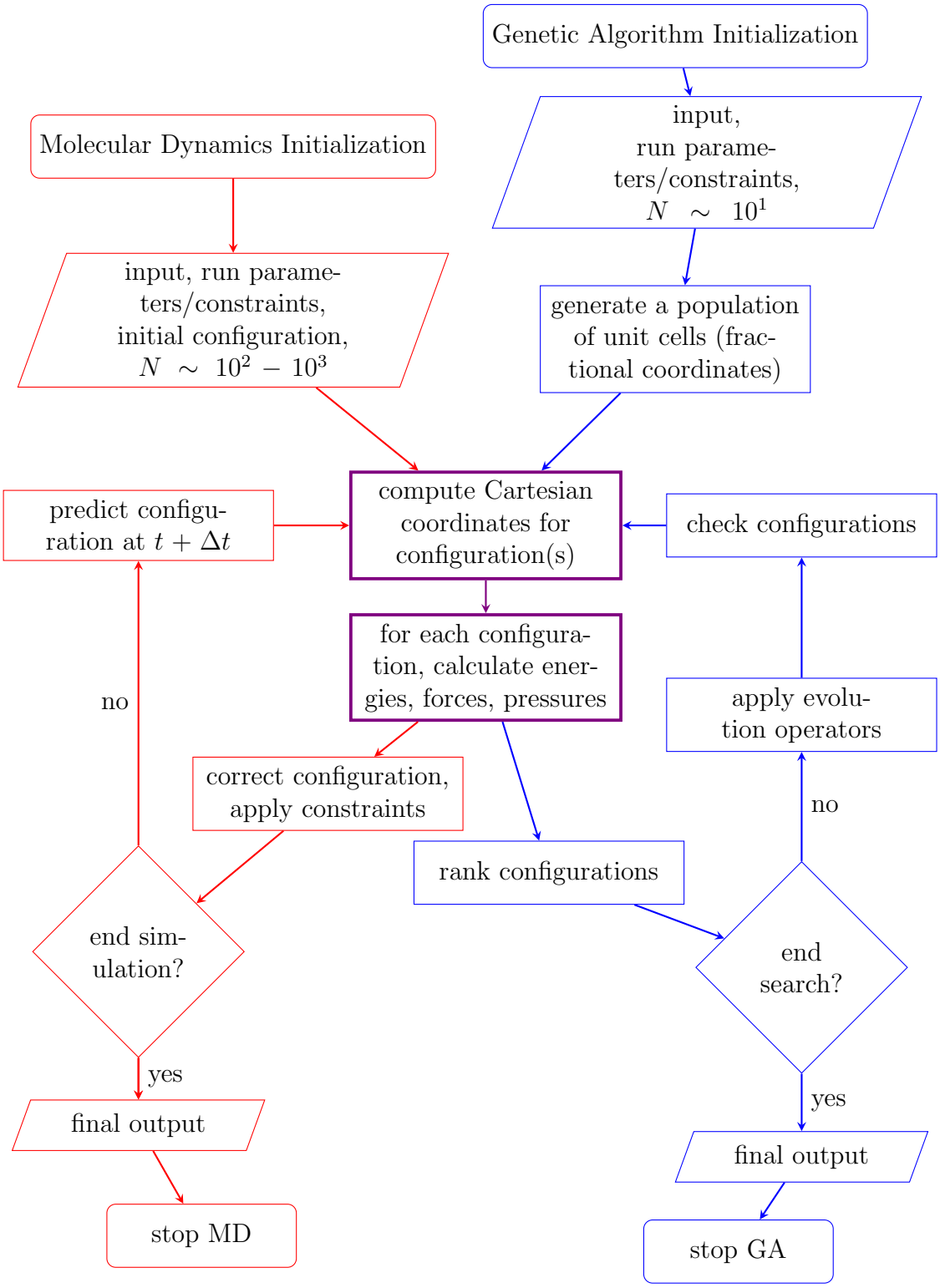

Figure A.1: MD (red) and GA (blue) Program Structures. The purple boxes are the aspects that are common to both programs.

The metric tensor is symmetric, with the diagonal elements containing information about the cell lengths and the off-diagonal elements relaying information about the angles formed between those vectors. To reduce the metric tensor to the conventional Cartesian representation mentioned above, the transformation is

$$\boldsymbol{h} = \begin{bmatrix} \sqrt{g_{11}} & 0 & 0 \\ \frac{g_{11}}{h_{11}} & \sqrt{g_{22} - h_{21}^2} & 0 \\ \frac{g_{13}}{h_{11}} & \frac{(g_{23} - h_{21}\, h_{31})}{h_{22}} & \sqrt{g_{33} - h_{31}^2 - h_{32}^2} \end{bmatrix}. \tag{A.3}$$

The volume of the cell can be calculated using $\boldsymbol{h}$ or $\boldsymbol{g}$, as

$$V = \det \boldsymbol{h} = \sqrt{\det \boldsymbol{g}}. \tag{A.4}$$

A.2 Particle Representations

The position of the center of mass of each particle in a configuration is stored as a fractional value of the simulation cell axes. Fractional coordinates are denoted with a superscript F, any other coordinates are Cartesian. A column vector of particle i's center of mass fractional coordinates, $\boldsymbol{r}_i^F$, is easily converted into the global Cartesian coordinates, $\boldsymbol{r}_i$, using the cell matrix, $\boldsymbol{h}^\mathsf{T}$ as

$$\boldsymbol{r}_i = \boldsymbol{h}^\mathsf{T} \boldsymbol{r}_i^F \,. \tag{A.5}$$

The center of mass representation is all that is required for the 1C ions. For the ions with more than one interaction site, the location of the off-center interaction sites must be specified. Each particle is treated as a rigid collection of interaction sites. Each interaction site within each particle has an amount of charge and particular LJ attributes assigned to it, as established in Chapter 2. The particles are rigid entities, meaning the lengths and angles between interaction sites are fixed and the interactions between sites on the same particle are ignored. For each particle type, the location of each interaction site is defined in a particle coordinate system (See Fig. 2.3 as examples).

In a configuration of many particles, the coordinates of each interaction site are specified by the particle's fixed geometry (based on particle type), the position coordinates of the particle's center of mass, and an orientation vector. The orientation vector gives the particle's orientation in the global coordinate system relative to the orientation defined in the particle's fixed geometry particle. The orientations are represented using quaternions,[119] which are vectors with four elements used to describe an orientation with three degrees of freedom. The redundancy avoids singularities that would be encountered if Euler angles were used. With the built in redundancy of the fourth element, quaternions must be normalized in order to uniquely specify an orientation. The orientation vector has four elements, $\boldsymbol{Q} = (q_1, q_2, q_3, q_4)$, where $|\boldsymbol{Q}| = 1$.

In the global configuration, each particle has a center of mass coordinate and orientation vector associated with it. A pair of rotation matrices are used to convert between the particle coordinate system and the global coordinate system. The rotation matrix, $\boldsymbol{A}$, transforms the fixed particle coordinates into the global coordinate system. The inverse of $\boldsymbol{A}$ transforms the global coordinates into the

local particle coordinates,[119]

$$\boldsymbol{A} = \begin{bmatrix} q_1^2 + q_2^2 - q_3^2 - q_4^2 & 2(q_2q_3 + q_4q_1) & 2(q_2q_4 - q_1q_3) \\ 2(q_2q_3 - q_1q_4) & q_1^2 - q_2^2 + q_3^2 - q_4^2 & 2(q_3q_4 + q_2q_1) \\ 2(q_2q_4 + q_3q_1) & 2(q_3q_4 - q_2q_1) & q_1^2 - q_2^2 - q_3^2 + q_4^2 \end{bmatrix} . \tag{A.6}$$

The coordinates of the interaction site α on ion i in the global configuration, $\boldsymbol{r}_{i\alpha}$, are calculated from the center of mass coordinates $\boldsymbol{r}_i$, the rotation matrix $\boldsymbol{A}_i$, and the reference geometry of the particle type as

$$\boldsymbol{r}_{i\alpha} = \boldsymbol{r}_i + \boldsymbol{A}_i \boldsymbol{s}_\alpha \, , \tag{A.7}$$

where $\boldsymbol{s}_\alpha$ is a column vector from the center of mass of particle i to the interaction site α in the fixed particle coordinate frame.

A.3 Interaction Potentials, Forces, Pressure

To approximate the bulk properties of the salts without dramatically increasing the necessary computational resources, the simulation cell is repeated (tiled) in all directions. Applying periodic boundary conditions (PBCs) prevents surface interactions.[119] The cell boundaries do not exert forces on the particles or disrupt the motions of the particles. When a particle moves through one side of the simulation cell, the particle coordinates are translated by the length of the cell so that it appears to re-enter the simulation cell from the opposite side. A snapshot with PBCs is shown in Fig. 2.6 for a two-phase simulation.

Interaction Potentials

The interaction potential and the definitions of terms within it was introduced in Chapter 2.2. The total potential energy is calculated for the configuration with the known coordinates of each interaction site. The two types of interaction potentials employed here are the Lennard-Jones (LJ) potential and electrostatic potential. The LJ potential is usually implemented in shifted and truncated form,

$$u_{LJ}(r_{ij}) = \begin{cases} 4\varepsilon_{ij}\left[\left(\frac{\sigma_{ij}}{r_{ij}}\right)^{12} - \left(\frac{\sigma_{ij}}{r_{ij}}\right)^{6}\right] - u_{LJ}(R_{cut}), & \text{if } r_{ij} \leq R_{cut} \\ 0, & \text{if } r_{ij} > R_{cut}, \end{cases} \tag{A.8}$$

where $r_{ij} = |\boldsymbol{r}_{ij}| = |\boldsymbol{r}_i - \boldsymbol{r}_j|$, and R_{cut} is set as a parameter. The entire LJ potential is shifted up by $u_{LJ}(R_{cut})$ and truncated at $r_{ij} = R_{cut}$. The shift eliminates the discontinuity in the potential and any unphysical changes in the forces resulting from a particle moving across the R_{cut} threshold. For a collection of particles interacting through a LJ potential, the total potential energy is calculated as

$$U_{LJ} = \frac{1}{2}\sum_{i}^{N}\sum_{j\neq i}^{N} u_{LJ}(r_{ij}) \tag{A.9}$$

where the factor of 1/2 eliminates the double counting that occurs by summing over two particle indices i and j.

The shifted and truncated LJ potential, as written in Eq. (A.8), neglects the interactions at distances greater than R_{cut}. In order to get accurate energies and pressures in a simulation, a long-range correction term is added to the energy and pressure terms that accounts for the shifted and truncated potential. The correction term takes the form of an integral from R_{cut} to infinity, and assumes a uniform

density of LJ particles. The equation for the long-range correction of the potential is given in Eq. (A.10), and the calculated quantity is added to U_{LJ} from Eq. (A.9). The correction is calculated for the entire system of N particles in volume V,

$$U_{LJ}^{tail\,corr} = \frac{8\pi N^2}{3V}\varepsilon_{ij}\sigma_{ij}^3\left[\frac{1}{3}\left(\frac{\sigma_{ij}}{R_{cut}}\right)^9 - \left(\frac{\sigma_{ij}}{R_{cut}}\right)^3\right]. \tag{A.10}$$

The long-range correction to the pressure is calculated as

$$P_{LJ}^{tail\,corr} = \frac{16\pi N^3}{3V^2}\varepsilon_{ij}\sigma_{ij}^3\left[\frac{2}{3}\left(\frac{\sigma_{ij}}{R_{cut}}\right)^9 - \left(\frac{\sigma_{ij}}{R_{cut}}\right)^3\right], \tag{A.11}$$

which is added to each diagonal element of the stress tensor. In both the MD code written for this project and the Gromacs runs, long-range corrections are applied to the potential energies and pressures.

The electrostatic potential is long-ranged and truncating the interactions beyond the LJ potential cutoff distance, R_{cut}, would introduce spurious errors into the potential and the force. The contributions to the potential energy are non-negligible and must be included in the calculation of the total potential and forces. The total electrostatic potential energy of point charges in a simulation cell with PBCs applied is

$$U_{ES} = \frac{1}{2}\sum_{i,j=1}^{N}{\sum_{\boldsymbol{n}}}' \frac{q_i q_j}{|\boldsymbol{r}_{ij} + \boldsymbol{n}h|}, \tag{A.12}$$

where $\boldsymbol{n}$ is a row vector of integers giving the translational directions of the image cells. In both programs, the maximum of each element of $\boldsymbol{n}$ is calculated as $\max(\boldsymbol{n}_\psi) = |R_{cut}/h_{\psi\psi}|$, rounded up to the nearest integer, where $\psi = 1$, 2, or 3. The range for each element spans from $-\max(\boldsymbol{n}_\psi)$ to $\max(\boldsymbol{n}_\psi)$. The prime on the $\boldsymbol{n}$ sum indicates that the $i = j$ term of the $\boldsymbol{n} = (0, 0, 0)$ sum is omitted to prevent

calculating self-interactions. The prefactor of 1/2 is to remove the double counting that occurs with the separate sums over i and j.

The electrostatic potential is inversely proportional to the distance between point charges, and so the potential varies greatly at short distances and slowly at large distances. In order to account for these long-range, slowly varying interactions, the electrostatic potential is calculated using the Ewald sum, where the $1/r$ part of the potential is modified by dividing it into short- and long-range parts,[119,136–138]

$$\frac{1}{r} = \frac{f(r)}{r} + \frac{1 - f(r)}{r}. \tag{A.13}$$

The modification, adding and subtracting a function $f(r)$ to the potential, is designed to reduce the short-range contributions to negligible amounts at the truncation limit (R_{cut}). A common, but by no means exclusive, choice for the function $f(r)$ is the complementary error function,

$$\mathrm{erfc}(x) = \frac{2}{\sqrt{\pi}} \int_x^\infty \exp(-\Omega^2) d\Omega, \tag{A.14}$$

where the error function is

$$\mathrm{erf}(x) = 1 - \mathrm{erfc}(x) = \frac{2}{\sqrt{\pi}} \int_0^x \exp(-\Omega^2) d\Omega. \tag{A.15}$$

The pair of functions is naturally substituted into the expression for $1/r$ where Ω is replaced with κr, where κ is a parameter that set to ensure both parts of the sum converge rapidly,

$$\frac{1}{r} = \frac{\mathrm{erfc}(\kappa r)}{r} + \frac{\mathrm{erf}(\kappa r)}{r}. \tag{A.16}$$

The first term on the right in Eq. (A.16) is the short-range part of the Ewald

summation. The function $\mathrm{erfc}(\kappa r)/r$ decays exponentially as $r \to \infty$ and has a singularity at $r = 0$. The short-range contribution is calculated in real space and is truncated for computational efficiency. The second term on the right of Eq. (A.16) has a long-range, slowly decaying tail. The long-range part is solved by taking the Fourier transform of the modified function and summing over reciprocal space vectors. Because of the sum over reciprocal space cell vectors, a self-correction term is applied that removes the contributions from a charge interacting with itself. For molecules with multiple interaction sites, a molecular correction is applied to remove the intramolecular self-energy. The Ewald sum is conditionally convergent.[120] It is important to ensure that the simulation box is exactly neutral and that the contributions from enough wave vectors are calculated in the reciprocal space sum to verify that the total energy has converged. The contributions to the Ewald sum that take into consideration PBCs and non-cubic simulation cells are given in Eq. (A.17) to Eq. (A.20).

$$U_{ES}^{\text{real space}} = \frac{1}{8\pi\epsilon_0} \sum_{i,j=1}^{N} {\sum_{\boldsymbol{n}}}' q_i q_j \frac{\mathrm{erfc}(\kappa|\boldsymbol{r}_{ij} + \boldsymbol{nh}|)}{|\boldsymbol{r}_{ij} + \boldsymbol{nh}|} \tag{A.17}$$

$$U_{ES}^{\text{reciprocal space}} = \frac{1}{2\pi V} {\sum_{\boldsymbol{k}}}' \frac{\exp\left(-\pi^2|\boldsymbol{r}_{\boldsymbol{k}}^2|/\kappa^2\right)}{|\boldsymbol{r}_{\boldsymbol{k}}^2|} \cdot \tag{A.18}$$

$$\sum_{i=1}^{N} \sum_{\alpha} \left(\left[\frac{q_{i\alpha}}{\sqrt{4\pi\epsilon_0}} \sin(2\pi \boldsymbol{r}_{\boldsymbol{k}} \cdot \boldsymbol{r}_{i\alpha}) \right]^2 + \left[\frac{q_{i\alpha}}{\sqrt{4\pi\epsilon_0}} \cos(2\pi \boldsymbol{r}_{\boldsymbol{k}} \cdot \boldsymbol{r}_{i\alpha}) \right]^2 \right)$$

$$U_{ES}^{\text{self}} = \frac{-1}{4\pi\epsilon_0} \frac{\kappa}{\sqrt{\pi}} \sum_{i} \sum_{\alpha} q_{i\alpha}^2 \tag{A.19}$$

$$U_{ES}^{\text{molecular correction}} = \frac{-1}{8\pi\epsilon_0} \frac{\kappa}{\sqrt{\pi}} \sum_{\alpha} q_\alpha \sum_{\beta} q_\beta \frac{\mathrm{erf}(\kappa|\boldsymbol{s}|)}{|\boldsymbol{s}|} \tag{A.20}$$

In Eq. (A.18), $\boldsymbol{k}$ is a row vector of integers, spanning the reciprocal lattice vectors in an analogous manner to $\boldsymbol{n}$ spanning real space lattice vectors. The vector

$\boldsymbol{r_k}$ is calculated as $\boldsymbol{r_k} = \boldsymbol{k}\boldsymbol{h}^{-1}$ where $\boldsymbol{h}^{-1}$ is the inverse of the cell matrix. The variables $\boldsymbol{r}_{i\alpha}$ and $q_{\imath\alpha}$ are the Cartesian coordinates and charge of site α on particle i.

The number of $\boldsymbol{k}$ vectors retained must be sufficient for the reciprocal space part to converge, but keeping excess of $\boldsymbol{k}$ vectors increases computational cost. The parameter κ controls the distribution of charge between the real space and reciprocal space part. It is advantageous to use a value of κ that keeps the distribution even, to improve computational efficiency and to keep the relative error in both parts of the sum approximately equal. The parameter κ is usually optimized first by keeping a large number of $\boldsymbol{k}$ vectors. Once κ is optimized, the number of $\boldsymbol{k}$ is reduced until reducing it further affects the convergence of the reciprocal space sum (within a desired tolerance). The implementation of the Ewald sum can be checked by computing the Madelung constants for different crystal lattices to a desired tolerance.

Typically, another correction term is required to account for the surface effects of building up the central simulation cell as a sphere in a medium with a relative permittivity, ϵ_s. If that medium is a vacuum ($\epsilon_s = 0$), the correction must be applied to the potential.[119] However, the appropriate boundary conditions for the ionic systems we consider here are the so-called tinfoil boundary conditions, where $\epsilon_s \to \infty$ and the correction term is zero.

In Gromacs, the electrostatic interactions were calculated using the particle-mesh Ewald technique. The short-range interactions are calculated in the same manner as the typical Ewald sum. The treatment of the long-range interactions is slightly different. The reciprocal space charge density is mapped on to a mesh with a certain grid spacing. The potential is calculated using a Fast Fourier Transform.

Forces and Pressure

The forces on each particle are used to propagate MD simulations through time, the details are presented further below in Section B.1. The force is the negative gradient of the potential, $\boldsymbol{f} = -\nabla u$, and is calculated in the evaluation routine of both the GA and MD programs. For the LJ pair potential, the force expression is[136–138]

$$\boldsymbol{f}_{LJ}(r_{ij}) = 24\varepsilon_{ij}\left[2\left(\frac{\sigma_{ij}}{r_{ij}}\right)^{12} - \left(\frac{\sigma_{ij}}{r_{ij}}\right)^{6}\right]\frac{\boldsymbol{r}_{ij}}{|r_{ij}^2|}. \tag{A.21}$$

For the Ewald sum, the force contributions from the real space and the reciprocal space terms are

$$\begin{aligned}\boldsymbol{f}_i^{\text{real space}} &= \frac{q_i}{4\pi\epsilon_0}\sum_{j=1,j\neq i}^{N} q_j \sum_{\boldsymbol{n}}\left[\frac{2\,\kappa}{\sqrt{\pi}}\exp(\kappa|\boldsymbol{r}_{ij}+\boldsymbol{nh}|^2)+\right.\\ &\left.\frac{\operatorname{erfc}(\kappa|\boldsymbol{r}_{ij}+\boldsymbol{nh}|)}{|\boldsymbol{r}_{ij}+\boldsymbol{nh}|}\right]\frac{\boldsymbol{r}_{ij}+\boldsymbol{nh}}{|\boldsymbol{r}_{ij}+\boldsymbol{nh}|^2}\end{aligned} \tag{A.22}$$

$$\begin{aligned}\boldsymbol{f}_i^{\text{reciprocal space}} &= \frac{1}{8\pi^2\epsilon_0 V}\sum_{\boldsymbol{k}\neq 0}\exp\left(\frac{-\pi^2\boldsymbol{r}_k^2}{\kappa^2}\right)\cdot\\ &\left[q_i\sin(\boldsymbol{r}_k\cdot\boldsymbol{r}_i)\left(\sum_{j=1}^{N} q_j\cos(\boldsymbol{r}_k\cdot\boldsymbol{r}_j)\right)-\right.\\ &\left.q_i\cos(\boldsymbol{r}_k\cdot\boldsymbol{r}_i)\left(\sum_{j=1}^{N} q_j\sin(\boldsymbol{r}_k\cdot\boldsymbol{r}_j)\right)\right]\frac{\boldsymbol{r}_k}{|r_k^2|}.\end{aligned} \tag{A.23}$$

The self-term and the molecular correction in the Ewald sum will not contribute to the force, as they are independent of position. The total force on particle i is then used to advance its position in the MD program.

For a particle with interaction site(s) off-center, the forces can result in a torque. It is convenient to advance the equations of motion in the particle's local

coordinate frame (denoted with a superscript l) rather than the global coordinate system (denoted with a superscript g). The torque on a particle's center in the local coordinate frame, $\boldsymbol{\tau}_i^l$, is calculated as

$$\boldsymbol{\tau}_i^l = \boldsymbol{A}_i \sum_\alpha \boldsymbol{s}_\alpha^g \times \boldsymbol{f}_\alpha^g \tag{A.24}$$

where $\boldsymbol{A}_i$ is the rotation matrix from Eq. (A.6) to convert from the global to local particle coordinates, $\boldsymbol{s}_\alpha^g$ is the position vector from the ion center to site α in the global coordinate frame, and $\boldsymbol{f}_\alpha^g$ is the force on site α in the global coordinate frame. The torque in the local frame is used in the equations of motion for the MD program described in Appendix B.

The virial theorem is used to calculate the instantaneous pressure tensor as

$$P_{\psi\nu} = \frac{1}{V}\left(\sum_{i=1}^{N} m_i v_{i\psi} v_{i\nu} + \sum_{i=1}^{N} r_{i\psi} f_{i\nu}\right), \tag{A.25}$$

where m_i, $\boldsymbol{v}_i$, and $\boldsymbol{f}_i$ are the mass, velocity, and force on particle i. The second term on the right in Eq. (A.25) with the product $\boldsymbol{r}_i \boldsymbol{f}_i$ must be calculated with care for charged particles under periodic boundary conditions in non-cubic cells.[136–139] The hydrostatic (bulk) pressure is calculated as the average of the diagonal elements of the pressure tensor.

Appendix B

Molecular Dynamics

B.1 Time Evolution

MD simulations are propagated through time by integrating the equations of motion over small time steps. Two common methods of integrating time are the leap-frog algorithm[119,120] and the Gear Predictor-Corrector scheme.[119] The simulations reported in this thesis were done using the leap-frog algorithm in Gromacs. In the leap-frog algorithm, the particle velocities and coordinates are advanced half of a time step out of sync,

$$\boldsymbol{v}_i\left(t+\frac{\Delta t}{2}\right) = \boldsymbol{v}_i\left(t-\frac{\Delta t}{2}\right)+\frac{\boldsymbol{f}_i(t)}{m_i}\,\Delta t \tag{B.1}$$

$$\boldsymbol{r}_i\left(t+\Delta t\right) = \boldsymbol{r}_i(t)+\boldsymbol{v}_i\left(t+\frac{\Delta t}{2}\right)\,\Delta\,. \tag{B.2}$$

The particle velocities at time t, are calculated as the average of $\boldsymbol{v}_i\left(t-\frac{\Delta t}{2}\right)$ and $\boldsymbol{v}_i\left(t+\frac{\Delta t}{2}\right)$.

A fifth-order Gear Predictor-Corrector scheme[119] was used to propagate through time in the MD code produced for this project. The predictor-corrector scheme is described here using a stand-in variable $\boldsymbol{Z}$. To propagate $\boldsymbol{Z}$ through time, $\boldsymbol{Z}$, and its first four derivatives at time t, are advanced to predicted values at time $t + \Delta t$ using a Taylor series expansion. The superscript P on $\boldsymbol{Z}$ denotes a predicted value,

$$\boldsymbol{Z}^P(t+\delta t) = \boldsymbol{Z}(t) + \left(\frac{d\boldsymbol{Z}}{dt}\right)\delta t + \frac{1}{2}\left(\frac{d^2\boldsymbol{Z}}{dt^2}\right)\delta t^2 + \frac{1}{6}\left(\frac{d^3\boldsymbol{Z}}{dt^3}\right)\Delta t^3 + \frac{1}{24}\left(\frac{d^4\boldsymbol{Z}}{dt^4}\right)\delta t^4. \tag{B.3}$$

In the Gear Predictor-Corrector scheme, the Taylor series expansion is also applied to the time derivatives of $\boldsymbol{Z}$. The set of prediction equations in matrix form is

$$\begin{bmatrix} \boldsymbol{Z}_0^P(t+\Delta t) \\ \boldsymbol{Z}_1^P(t+\Delta t) \\ \boldsymbol{Z}_2^P(t+\Delta t) \\ \boldsymbol{Z}_3^P(t+\Delta t) \\ \boldsymbol{Z}_4^P(t+\Delta t) \end{bmatrix} = \begin{bmatrix} 1 & \Delta t & \frac{1}{2}\Delta t^2 & \frac{1}{6}\Delta t^3 & \frac{1}{24}\Delta t^4 \\ 0 & 1 & \Delta t & \frac{1}{2}\Delta t^2 & \frac{1}{6}\Delta t^3 \\ 0 & 0 & 1 & \Delta t & \frac{1}{2}\Delta t^2 \\ 0 & 0 & 0 & 1 & \Delta t \\ 0 & 0 & 0 & 0 & 1 \end{bmatrix} \begin{bmatrix} \boldsymbol{Z}_0^P(t) \\ \boldsymbol{Z}_1(t) \\ \boldsymbol{Z}_2(t) \\ \boldsymbol{Z}_3(t) \\ \boldsymbol{Z}_4(t) \end{bmatrix} \tag{B.4}$$

where the subscript indicates the n^{th} time derivative of $\boldsymbol{Z}$. The predicted configuration (using $\boldsymbol{Z}^P(t+\Delta t)$) is evaluated and then corrected using equations of motion. In an example Newtonian system, the forces are evaluated at $t + \Delta t$ using the positions and interaction potential(s), and then the positions and their time derivatives are corrected using

$$\ddot{\boldsymbol{r}}_i = \boldsymbol{f}_i / m_i. \tag{B.5}$$

For particles with more than one interaction site, the orientational equations of

motions are corrected in the local coordinate frame as[119]

$$\dot{\boldsymbol{\omega}}_{\psi}^{l,C} = \left(\boldsymbol{\tau}_{\psi}^{l} + \boldsymbol{\omega}_{\nu}^{l,P}\boldsymbol{\omega}_{\phi}^{l,P}\left(I_{\nu\nu} - I_{\phi\phi}\right)\right)/I_{\psi\psi}, \tag{B.6}$$

where $\dot{\boldsymbol{\omega}}_{\psi}^{l,C}$ is the corrected time derivative of the angular velocity in local coordinates and $\boldsymbol{I}$ is the principle moment of inertia matrix. The indices ψ, ν, and ϕ are axes labels x, y, or z in the local coordinate system.

The updated angular velocities are used to correct the orientation vector as

$$\begin{bmatrix} \dot{q}_1^C \\ \dot{q}_2^C \\ \dot{q}_3^C \\ \dot{q}_4^C \end{bmatrix} = \frac{1}{2}\begin{bmatrix} q_1 & -q_2 & -q_3 & -q_4 \\ q_2 & q_1 & -q_4 & q_3 \\ q_3 & q_4 & q_1 & -q_2 \\ q_4 & -q_3 & q_2 & q_1 \end{bmatrix}\begin{bmatrix} 0 \\ \omega_x^l \\ \omega_y^l \\ \omega_z^l \end{bmatrix}. \tag{B.7}$$

The difference between the predicted and corrected quantities, $\Delta\boldsymbol{Z}$, is then used to correct the other time derivatives as

$$\begin{bmatrix} \boldsymbol{Z}_0^C \\ \boldsymbol{Z}_1^C \\ \boldsymbol{Z}_2^C \\ \boldsymbol{Z}_3^C \\ \boldsymbol{Z}_4^C \end{bmatrix} = \begin{bmatrix} \boldsymbol{Z}_0^P \\ \boldsymbol{Z}_1^P \\ \boldsymbol{Z}_2^P \\ \boldsymbol{Z}_3^P \\ \boldsymbol{Z}_4^P \end{bmatrix} + \begin{bmatrix} C_0 \\ C_1 \\ C_2 \\ C_3 \\ C_4 \end{bmatrix}\Delta\boldsymbol{Z} \tag{B.8}$$

where $\Delta\boldsymbol{Z} = \boldsymbol{Z}^C - \boldsymbol{Z}^P$ is the difference between the predicted and calculated value of $\boldsymbol{Z}$ from the evaluation routine, and the C matrix contains a set of numerical coefficients (discussed further below). In the Newtonian example, $\Delta\boldsymbol{Z} = \boldsymbol{f}/m - \boldsymbol{a}$,

and applying the correction to the positions and their time derivatives is what maintains the Newtonian mechanics of the system.

The matrix of numerical coefficients, C, are determined by the order of the differential equation of motion.[119] The positions are governed by a second order differential equation, whereas the angular velocities and orientations are governed by a first order differential equation. The values of the non-zero coefficients were established by Gear.[119]

Table B.1: Numerical coefficients used in the Gear Predictor-Corrector algorithm.[119]

Coefficient	1st order DE	2nd order DE
C_0	251/720	19/120 or 19/90
C_1	1	3/4
C_2	11/12	1
C_3	1/3	1/2
C_4	1/24	1/12

The Gear predictor-corrector algorithm was used to advance the positions, orientations, Nosé-Hoover thermostat, and the cell dynamics in the MD program written for this project.

B.2 Simulation Constraints

B.2.1 Temperature — Particle Motion

A Nosé-Hoover thermostat[100–102] regulates the temperature of an ensemble of particles by adding a correction term to the equations of motion. The particle

accelerations are propagated through time as

$$\boldsymbol{a}_i = \frac{\boldsymbol{f}_i}{m_i} - \xi \boldsymbol{v}_i, \tag{B.9}$$

where ξ is a friction coefficient that couples the ensemble of particles to the desired temperature, T_{set}. The friction coefficient, ξ, propagates through time as

$$\frac{d\xi}{dt} = \frac{1}{Q}\left[\sum_i^N m_i \left|\boldsymbol{v}_i\right|^2 - 3Nk_B T_{set}\right], \tag{B.10}$$

where k_B is the Boltzmann constant. The term in brackets measures the difference between the instantaneous temperature in the simulation and the target temperature. The temperature is regulated through ξ, which increases or decreases the particle motion when there is a difference between the desired and actual temperature. A similar modification is made to Eq. (B.6) to thermostat the rotational motion, where a separate friction coefficient times the angular velocity is subtracted from the right hand side.

The response time of the thermostat is determined by the "heat bath mass," Q, which is a parameter that must be chosen with care. A small Q gives a faster response time and has a larger influence on the particle dynamics. A loose thermal coupling (large Q) will have a slow response time, meaning that on one hand, an out-of-equilibrium system may take a long time to reach equilibrium but, on the other hand, the perturbations of the particle dynamics are not as large. For the MD code produced for this project, $Q = 5$ is an appropriate value. In Gromacs, the strength of the thermal coupling for all thermostats is set in terms of a relaxation time, τ_T. For the Nosé-Hoover thermostat, $\tau_T \propto Q^{1/2}$. In the Gromacs simulations done here, the relaxation time was 0.1 ps, with separate coupling groups for the

cations and anions.

B.2.2 Pressure — Simulation Cell

The simulation cell size and shape are both allowed to fluctuate in our NPT molecular dynamics simulations. The desired pressure, P_{set} was maintained using the Parrinello-Rahman barostat[103,104] in the Gromacs simulations. The equations of motion use fractional coordinates, $\boldsymbol{r_i^F} = (\boldsymbol{h}^{-1})^{\mathsf{T}} \boldsymbol{r_i}$,

$$\ddot{\boldsymbol{r}}_i^F = \frac{(\boldsymbol{h}^{-1})^{\mathsf{T}} \boldsymbol{f}_i}{m_i} - \boldsymbol{g}^{-1} \dot{\boldsymbol{g}} \dot{\boldsymbol{r}}_i^F \tag{B.11}$$

$$\ddot{\boldsymbol{h}}^{\mathsf{T}} = \frac{1}{W} (\boldsymbol{P} - \boldsymbol{I} P_{set}) V \boldsymbol{h}^{-1}, \tag{B.12}$$

where the single and double dots over variables represent the first- and second-derivatives with respect to time, and $\boldsymbol{I}$ represents the 3×3 identity matrix. Here, we see the dependencies on the simulation cell vectors ($\boldsymbol{h}$), the metric tensor $\boldsymbol{g}$, and the instantaneous pressure tensor, $\boldsymbol{P}$. The effective cell mass, W, determines the responsiveness of the cell dynamics. A slow response (large W) means the size and shape of the container will fluctuate slowly, whereas, a small W will lead to a more dynamic container. The relaxation parameter W of the barostat is analogous to the relaxation parameter Q of the thermostat.

In the code produced for this project, the size and shape fluctuations were implemented using Souza and Martin's metric tensor approach.[139] In this approach, the equations of motion for the particle dynamics are the same as Eq. (B.11). The particle dynamics are governed by the same equation for both the metric tensor barostat and Parrinello-Rahman barostat, but trajectories from identical initial configurations would produce different particle motions. The dynamics of the cell affect

the particle trajectories through $\dot{\boldsymbol{g}}$ in Eq. (B.11), and in the metric tensor approach, the cell dynamics are not governed by Eq. (B.12), but by

$$\begin{aligned} \ddot{g}_{\gamma\delta} &= \frac{1}{2W\sqrt{\det g}}\left(\frac{P_{\gamma\delta}}{\sqrt{\det g}} - P_{set}g_{\gamma\delta}\right) + \\ &\left(\dot{g}_{\gamma\zeta}g^{\zeta\eta}\dot{g}_{\eta\delta} - g^{\zeta\eta}\dot{g}_{\zeta\eta}\dot{g}_{\gamma\delta}\right) + \frac{1}{2}\left(\dot{g}_{\zeta\eta}g^{\eta\lambda}\dot{g}_{\lambda\nu}g^{\nu\zeta}\right)g_{\gamma\delta}, \end{aligned} \tag{B.13}$$

where the Einstein notation has been used to signify summation over repeated Greek indices. Details for the implementation can be found in the paper by Souza and Martins.[139]

Appendix C

Genetic Algorithm

Genetic algorithms optimize multi-parameter problems using concepts borrowed from evolutionary biology such as survival of the fittest.[140] The algorithm starts by taking a collection of possible solutions, called a population, and repeats a cycle of evaluation and evolution until the conditions for termination are satisfied. In each cycle, the possible solutions are ranked by set criteria and the algorithm is designed to optimize the candidate structures.

Genetic algorithms have been developed and used for finding crystal structures and cluster geometries.[114,141–148] In the present implementation, a candidate structure is a viable crystal unit cell and the GA is designed to minimize the potential energy.

An overview of the GA program is given as part of Fig. A.1. The generation of the initial set of candidate crystal structures, their evolution through applying a variety of mutation operators, and how the GA terminated are discussed in this

section.

C.1 Initialization

Each candidate crystal structure is specified by three unit cell vectors, $\boldsymbol{a}$, $\boldsymbol{b}$, $\boldsymbol{c}$, three angles between those vectors, α, β, γ, and the number, type, fractional coordinates, and orientation (if applicable) of each particle within the unit cell. The particle "type" specifies the particle label, the rigid geometry of the interaction sites, and the interaction parameters for each site within the particle. The number of particles and the ratio of particle types is set before the run to reduce the number of variables the GA has to optimize. To sample different unit cell possibilities, the number of particles within the unit cell is varied over separate runs of the GA. The GA is used for two types of systems here, salts and binary LJ mixtures. For the salts, charge neutrality limits the possible particle type ratios, whereas for the binary LJ mixtures, the ratio of particle types is varied as a run input.

The six unit cell parameters are initialized as cubes with the length of each side set to $V_i^{1/3}$ where V_i is an approximate desired volume of the unit cell (near a reduced density of 1.0). An option was included to keep all cell angles fixed at 90° for the entire GA run to exclusively sample orthorhombic configurations.

The initial particle labels (types) are assigned with the help of a pseudo-random number (PRN) generator. The range [0,1] is divided into the number of particle types present. A PRN on [0,1] is generated for each particle (in serial), and the particle label is assigned based on comparing the label ranges and the PRN. Counts of the assigned labels are kept to ensure the assigned particle types matched the input specifications. The fractional coordinates along each axes are assigned

using the PRN on [0,1] for each particle. Each particle is initialized with the same orientation.

C.2 Configuration Checks

Before each evaluation of the energies of the population of crystal structure candidates, the configurations are put through some "rational" checks. The candidates are checked for obvious signs that the crystal structure will yield a poor (high) energy or unphysical structure.

The first check screens the unit cells for lengths that are too short or too long and angles that are too acute or too obtuse. The cell length limits are computed from the particle type with the largest LJ diameter, σ_{max}, and the number of particles within the cell. The minimum cell length allowed is $N\sigma_{max}/6$ and the maximum length allowed is $N\sigma_{max}/2$. If the cell length falls outside of these bounds, a replacement cell length is generated using a PRN on $[N\sigma_{max}/6, N\sigma_{max}/2]$. Each angle has to be between 45° and 120°, otherwise the cell is reset.

The fractional coordinates of each particle must be between 0.0 and 1.0, and are translated by ± 1.0 as necessary. The fractional coordinates are also checked for overlaps. If the distance between two particles along all three axes are all below a threshold of 0.05 (in fractional units), then one particle's fractional coordinates are regenerated using the PRN generator, and the configuration is checked again.

After the entire population passes the checks, the energies are evaluated (as discussed in Appendix A.3). Before the mutation operators are applied, the candidate structures are ranked from best to worst by their potential energies.

C.3 Configuration Evolution

Aside from the elitism operator, which preserves the previous generations best candidates, each mutation operator is designed to change some attribute of the candidate crystal structure. A collection of 15 mutation operators that balance both drastic changes and minor tweaks have been implemented in order to effectively search for the best crystal structure.

The rates of application of each mutation operator are set as program parameters, and have been tested to ensure a robust collection of candidates are produced and that the GA is able to find, and converge to, the same crystal structure from multiple runs with different initializations of the PRN generator. The mutation operators are applied to candidates selected using the PRN with the best candidate excluded.

Elitism

The elitism operator creates a perfect copy of the best candidate crystal structures from the current generation and places them into the next generation. The sole function of this operator is to preserve the best candidates through generations. For a population of 50 candidate structures, the 6 best structures are preserved using the elitism operator (12%). Keeping the elitism operator near 10% maintains the diversity of the population long enough to explore a variety of crystal structures while still converging within a reasonable number of generations.

C.3.1 Diversity Operators

The operators described in this section are particularly successful at producing lower energy configurations in the early stages of a run, because the new configurations (offspring) are very different from the initial configurations (parents). Each of these operators is used to create 5 — 10% of the next generation.

Crossover

The crossover operator splices two candidate structures together to create two "offspring." The attributes of the first parent are copied to the first offspring until the crossover point is reached. After the crossover point, the attributes of the second parent are copied to the first offspring to complete the attribute set of the first offspring. The process is repeated to create a second offspring where the order of the parents is switched (the crossover point remains the same).

The cell lengths and angles are preserved from the dominant parent. The crossover point is determined by a PRN generated on [2,N-1]. The recombination is applied to the particles only. The particle labels, fractional coordinates, and the particle orientations are transferred from one parent before the crossover point and the other parent after.

Blend

The blend operator, like the crossover operator, creates two new candidate structures from two parents in the current generation. In this operator, the fractional coordinates of the two parent configurations are sorted and then paired (one from each parent) by closest distance. The offspring's fractional coordinates are then

generated by taking a weighted average of the positions. The average is weighted 2/3 to the dominant parent and 1/3 to the recessive parent. Switching the dominant/recessive roles of the parents produces a second offspring configuration. The particle labels and orientations in the offspring configurations are directly copied from the dominant parent. The cell lengths and angles are also subject to the weighted average.

Geometric Mean

The geometric mean operator produces one offspring from two parents. Each of the cell parameters and fractional coordinates are generated by combining the corresponding attributes of both parents in a geometric fashion. For example, the length of cell vector $\boldsymbol{a}$ is computed as $|a_{\text{child}}| = \sqrt{|a_{\text{Mom}}|\,|a_{\text{Dad}}|}$. The particle labels and orientations are all reassigned using the PRN generator.

Swap

The swap operator mutates a configuration by switching two fractional coordinates of two different particles. The two particles and which fractional coordinates are to be swapped are selected using the PRN. An example would be swapping the fractional coordinate along $\boldsymbol{b}$ on particle 3 with the fractional coordinate along $\boldsymbol{a}$ of particle 5.

Ripple

This operator is constructed from the description of the Ripple operator from the excellent work of D.C. Lonie and E. Zurek.[148] The ripple operator displaces the

coordinates in one direction based on the position of the other two coordinates and how many wavelengths are chosen to fit in the cell. The maximum wavelength is set to 2, and the magnitude of the ripple is set to 0.15 in this work. This operator copies the cell attributes, particle labels, and orientations directly from the parent configuration. Only the fractional coordinates of the particles change.

Strain

The strain operator also follows from the work of D.C. Lonie and E. Zurek.[148] The fractional coordinates, orientations, and labels of the particles of the parent configuration are copied exactly to the offspring. The parent's cell parameters are adjusted by applying a symmetric strain matrix that includes six PRNs that skew (or deskew) the cell vectors.

Swap Cell

The swap cell operator generates two offspring from two parents. The properties of the particles are transmitted from one parent to one offspring, but the unit cell parameters are taken from the other parent. There are no mutations of the attributes, but the two new combinations of attributes create offspring that are distinct from the parents (unless, of course, the cell parameters of the two parents are similar).

Replace Attributes

Two operators that simply replace part of the parent configuration with a new one that is generated pseudo-randomly. One operator replaces the three fractional

coordinates and orientations of a single particle in the parent configuration. Another operator replaces the orientations of all particles within a configuration. These replacement operators are applied least of the diversity operator set—they each create about 4% of the next generation.

C.3.2 Refinement Operators

The changes introduced by the refinement operators are typically small. Whereas the diversity operators discussed earlier are more successful at the beginning of a GA run, these refinement operators have more success at improving the configurations near the final stages of the GA run. Each of the following operators are used to generate less than 5% of the configurations for the next generation except for the adjust volume operator (which is closer to 10%).

Adjust Volume

The adjust volume operator scales the cell lengths by a maximum of 5%. Two PRNs are used in this operator. One determines the magnitude of the volume shift (generated on [0,1] and multiplied by the maximum volume adjustment permitted), and the second PRN (generated on [-1,1]) determines the sign of the volume fluctuation.

Reorient

The reorient operator changes the orientations of all of the particles from the parent configuration. The orientations are rotated by a maximum of 10° about one axis. Each particle is rotated by a different amount. The parent's cell parameters,

fractional coordinates, and particle labels are preserved.

Adjust Cell Angle

The adjust cell angle operator changes one cell angle by a maximum of 20°. The actual angle and the direction are generated using PRNs in a manner similar to the volume adjustment operator. The cell angle that is adjusted (α, β, or γ) is selected pseudo-randomly.

Adjust Cell Lengths

Three operators, in addition to the volume adjust operator described above, are used to manipulate the cell axes lengths. The first operator makes all three cell lengths equal by taking an average of the parent's cell lengths, which is useful for accessing cubic structures. The second operator scales a single axis (selected pseudo-randomly) by a maximum of 10%, in a manner similar to the volume adjust operator. The third operator contracts the longest cell axis by up to 15%.

C.4 Termination

The GA terminates after executing a predetermined number of generations (usually 200), regardless of how long the "best" crystal structure has been ranked #1. Another common termination scheme stops the run once the energy of the best crystal structure has not been improved upon for a set number of generations.

In order to be confident that the final configuration is one of the lowest energy crystal structures, the GA is run multiple times with different PRN initializations

and different parameters (particularly N, the number of particles in the unit cell).

C.5 GA Results

The program was tested on binary mixtures of LJ particles. The two particle types, A and B, have LJ length parameters $\sigma_{AA} = 1.0$, $\sigma_{AB} = 0.8$, and $\sigma_{BB} = 0.88$, while the LJ energy parameters are $\varepsilon_{AA} = 1.0$, $\varepsilon_{AB} = 1.5$, and $\varepsilon_{BB} = 0.5$. These parameters do not follow the Lorentz-Berthelot mixing rules[119] and are designed to favour the mixing of the two particle types. The parameters roughly correspond to the nickel phosphorus (Ni−P) system.[149,150] The $A_{80}B_{20}$ composition corresponds to a eutectic in the Ni−P system, which has not been reproduced in the LJ binary mixture.[151] The GA results (the structures, densities, and potential energies at $T = 0$ and $P = 0$) agree with those found in the literature.[151]

The GA was not used for the model salts studied here because the majority (about 84%) of the salts spontaneously crystallized upon cooling in MD simulations. An alternate approach to find crystal structure candidates (preparing and heating crystal structures in MD simulations) was used because it was convenient for the simple salts studied here.

Appendix D

Temperature Tables

Table D.1: The five characteristic melting-related temperatures for the size symmetric 2L - 1C salts that crystallize spontaneously. The T_m values are the estimates from the hysteresis loops [Eq. (2.5)]. The two-phase simulations give the bounding temperatures for the CsCl-solid to liquid transition. All temperatures are in kelvin.

Cation	Hysteresis Loops			Two-phase	
	T_-	T_+	T_m	T_s	T_l
1C	1050	1400	1238	1250	1300
2L33-06	1050	1400	1238	1250	1300
2L33-08	1050	1400	1238	1250	1300
2L33-10	1050	1300	1182	1200	1250
2L33-12	1050	1300	1182	1200	1250
2L33-14	1050	1250	1154	1150	1200
2L33-16	950	1300	1139	1150	1200
2L33-18	1000	1150	1078	1100	1150
2L33-20	900	1150	1032	1050	1100
2L33-22	850	1200	1040	1050	1100
2L33-24	800	1000	906	950	1000

Continued on next page...

Table D.1: (Continued)

Cation	Hysteresis Loops			Two-phase	
	T_-	T_+	T_m	T_s	T_l
2L50-06	1050	1250	1154	1250	1300
2L50-08	1000	1350	1188	1200	1250
2L50-10	1050	1250	1154	1200	1250
2L50-12	950	1300	1139	1150	1200
2L50-14	950	1350	1167	1100	1150
2L50-16	850	1150	1011	1050	1100
2L50-18	750	1000	884	950	1000
2L50-20	700	950	835	850	900
2L50-22	700	850	778	750	800
2L50-24	650	800	729	750	800
2L67-06	1000	1450	1246	1200	1250
2L67-08	1000	1350	1188	1200	1250
2L67-10	950	1300	1139	1150	1200
2L67-12	850	1150	1011	1100	1150
2L67-14	750	1100	942	1000	1050
2L67-16	700	900	806	850	900
2L67-18	550	850	716	800	850
2L67-20	550	850	716	750	800
2L100-06	950	1250	1110	1150	1200
2L100-08	900	1200	1060	1100	1150
2L100-10	700	1250	1015	1000	1050

Table D.2: The five characteristic melting-related temperatures for the 2L - 1C salts that vitrify. Here, T_- is the glass transition temperature, T_g, as defined earlier, and T_+ is for the melting of the 111_n crystal structure. The temperatures from the two-phase simulations are for the 111_n solid to liquid transition. All temperatures are in kelvin.

Cation	Hysteresis Loops			Two-phase	
	T_-	T_+	T_m	T_s	T_l
2L67-20	400	850	667	700	750
2L67-22	400	850	667	650	700
2L67-24	400	800	634	600	650
2L100-12	450	900	714	700	750
2L100-14	400	1000	768	750	800
2L100-16	400	1000	768	800	850
2L100-18	400	1000	768	800	850
2L100-20	400	950	734	600	650
2L100-22	400	800	634		
2L100-24	350	650	523		

Appendix E

Crystal Structures

E.1 111_n Structure

The 111_n structure was shown and described in Chapter 3 (Fig. 3.3).

```
Space Group 111  D2d-1     P-42m
Origin at    0.23450   0.24000   0.82550
Values of a,b,c,alpha,beta,gamma:
0.9420   0.9420   1.0123  90.000  90.000  90.000
Atomic positions in terms of a,b,c:
CM1 Wyckoff position n, x = -0.23513, z =  0.1775
CC1 Wyckoff position n, x = -0.23538, z =  0.3390
AM1 Wyckoff position n, x = -0.23550, z = -0.3725
```

Figure E.1: Selected output from running the Findsym program on the unit cell above. The tolerance was set to 0.03.

Table E.1: The contents of a 111_n unit cell from simulations of the 2L100-16 - 1C salt. The table gives the unit cell dimensions, site labels, and xyz coordinates. The coordinates and the unit cell dimensions are in nanometers.

unit cell lengths (a,b,c)	0.93929	0.94383	1.01230
unit cell angles (α, β, γ)	90.0	90.0	90.0
Site label	x	y	z
CM1	0.000	0.480	0.650
CC1	0.000	0.477	0.490
CM2	0.469	0.472	0.001
CC2	0.470	0.474	0.170
CM3	0.000	0.000	0.000
CC3	0.000	0.000	0.157
CM4	0.469	0.009	0.641
CC4	0.469	0.007	0.481
AM1	0.000	0.473	0.202
AM2	0.470	0.480	0.457
AM3	0.000	0.003	0.448
AM4	0.469	0.005	0.193

E.2 Var-CsCl Structure

The var-CsCl crystal structure was found as a result of the earlier work on the A100 2L67-24 - 1C salt, but was not fully investigated then. The structure is shown in Fig. E.2, and is an orientationally ordered variation on the CsCl crystal structure.

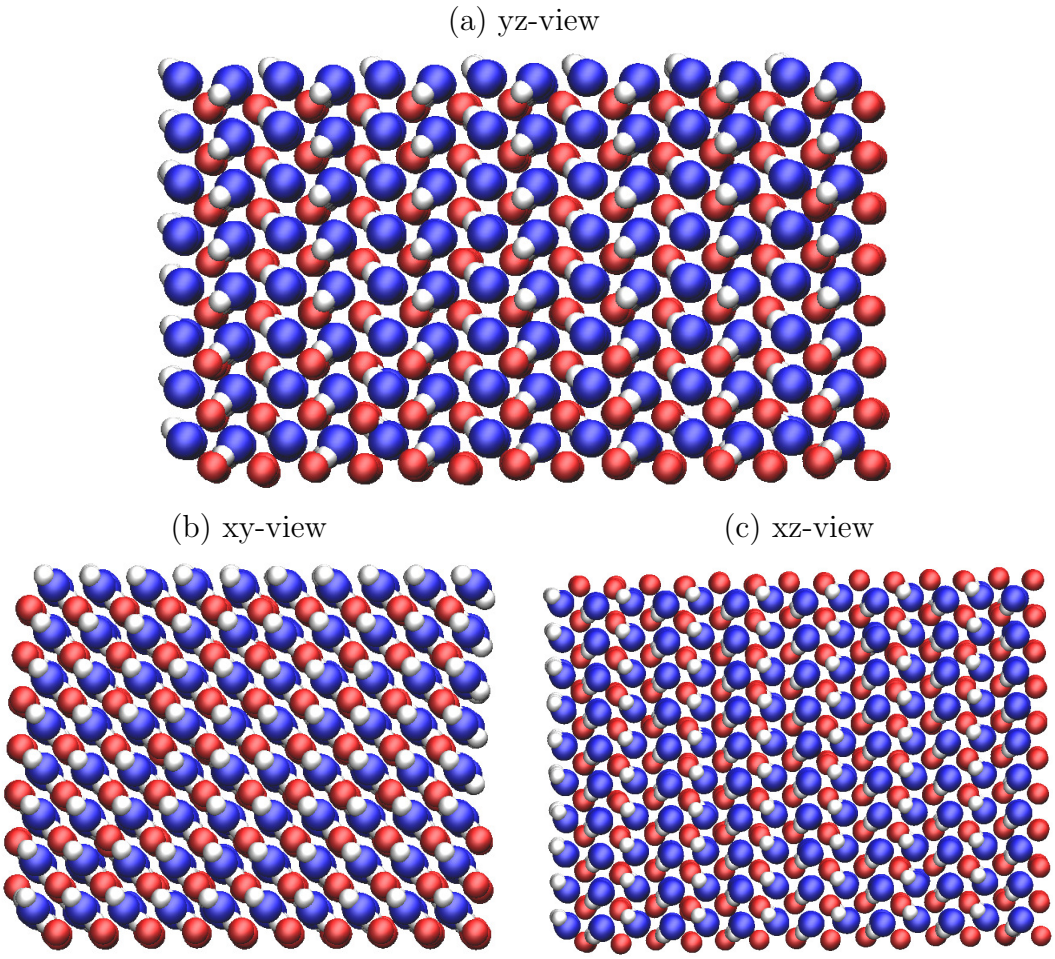

Figure E.2: Orientationally ordered crystal structure of the A100 2L67-22 - 1C salt. The cation centers, cation off-center sites, and anions are shown in blue, white, and red, respectively, and are not shown to scale.

E.3 Var-111_n Structure

The var-111_n structure is a variation of the 111_n crystal structure. The crystal structure adjusts to accommodate cations that are slightly larger than the anions. The B133 2L67-22 - 1C and B133 2L67-26 - 1C salts are the two that rearranged into the var-111_n structure.

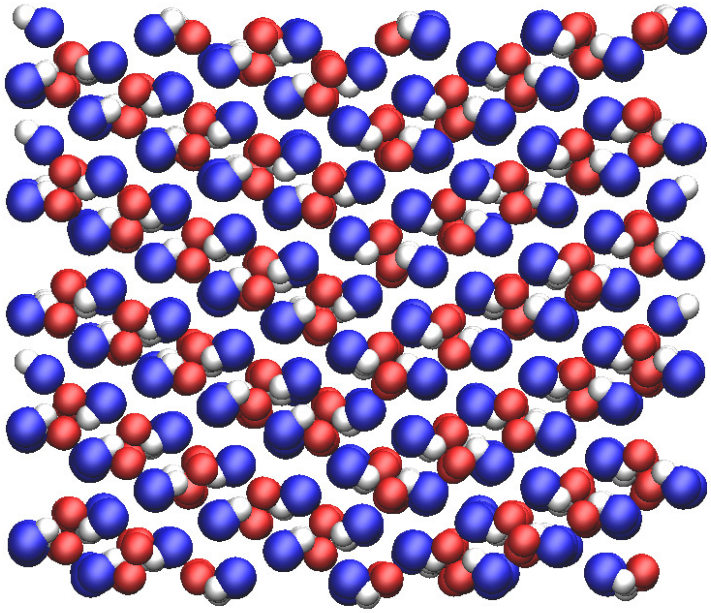

Figure E.3: The var-111_n crystal structure shown for the B133 2L67-22 - 1C salt. The cation centers, cation off-center sites, and anions are shown in blue, white, and red, respectively, and are not shown to scale.

Appendix F

Input Files

Example input files for heating the 111_n crystal of the A100 2L100-16 - 1C salt are included in this Appendix. The execution script (bash) is a *.pbs file designed for job submission on Orcinus and the example included here will heat an initial configuration from an initial temperature of 50 K up to 1200 K (or until the wall clock limit is reached, whichever is first). The *.pbs files were generated in sets (cooling, heating, and two-phase simulations) for each salt using a bash script.

The *.gro file is the initial configuration file that gives the particle labels, positions, and optionally, velocities, and the lengths that define the simulation cell. The initial *.gro files were crystal structures (either CsCl at a reduced density of 0.8 or a variety of crystal structures at a reduced density of 1.1, depending on the desired target phase) and were generated using a small program I wrote.

The *.top file specifies the topology and number of each type of particle in the system. (Note that the number of each particle type specified in the *.top file

and given in the *.gro file must match.) The *.top files vary for each salt and were generated using a bash script and were automatically modified before the simulation to ensure the numbers of particles matched the *.gro input file.

The *.mdp file specifies the run parameters for Gromacs. This particular *.mdp example file is for a 4.0 ns NPT run (with the barostat parameters used in the hysteresis loops) at a temperature of 600 K. I had folders of *.mdp files symbolically linked in each running folder for simulation type. The hysteresis loops required sets of *.mdp files for each cutoff distance. The two phase simulations required four sets of *.mdp files for each cutoff distance (energy minimization, NVT, anisotropic NPT, and isotropic NPT). The isotropic NPT .mdp files were not the same as the isotropic NPT .mdp files for the hysteresis loops; the barostat relaxation parameter was slower for the two-phase simulations. Within each folder, there was an *.mdp file for each simulation temperature.

```
#!/bin/bash
#PBS -S /bin/bash
#PBS -l procs=8
#PBS -l walltime=80:00:00
#PBS -r n
#PBS -N A100_2L100-16_1C_H___111n
#PBS -M <<email address>>
#PBS -m ea

cd $PBS_O_WORKDIR
echo "Current working directory is `pwd`"

module load gromacs/4.6.2

# *******
# ion specifics
# *******

# cation
geom=2L
geom1=100
cdi=16
cda=$(printf %02d $cdi)

# anion
geom2=1C

# ion sizes
Size_ratio=100

Cat_Size=050
Ani_Size=050

# *******
# run specifics
# *******

rcutoff=170

diri="H"
# diri is a letter to indicate the temperature direction, H = heat a prepared crystal structure from 50 K.

folder1= #source folder for .mdp folders
folder2= #destination folder for runs

# labels
salt=$geom$geom1"-"$geom2
label=$geom"-"$cda"_"$geom2
label2=$geom$geom1"-"$cda"_"$geom2
longlabel=$geom$geom1"-"$cda"_"${Cat_Size}"_"$geom2"_"${Ani_Size}

ln -s <<path to $folder1>>/npt_iso/npt_$rcutoff npt

temp1=1200
temp2=50

grofile="50.gro"

# "50.gro" is the name of the input .gro file for the run at the first temperature. For the heating runs
(diri="H"), it is a perfect crystal structure set at a reduced density of 1.1.
```

Figure F.1: Example .pbs file (page 1/3)

```
# *******
# Main temperature loop:
# *******

((temp = $temp2))

while ((temp<=temp1))

do

  if [ -s $grofile ]
  then

    ndxfile=$label2"_"$temp".ndx"

    echo -e "aCM\naCC\naAM\nq\n" | make_ndx_mpi_d -f $grofile -o $ndxfile

    nptfile="npt/npt"$temp".mdp"
    topfile=$longlabel".top"
    tprfile=$temp".tpr"

    # make sure .top and .gro molecule numbers match. Trust the .gro file.
    declare -i ntot=$(sed -n 2p $grofile)

    nmol=$(( ntot * 2 / 3 ))
    ncat=$(( ntot / 3 ))
    nani=$(( ntot / 3 ))

    localtop="local_top.top"

    head -n -2 $topfile > $localtop
    echo " CAT        "$ncat >> $localtop
    echo " ANI        "$nani >> $localtop

    mv $localtop $topfile

    # simulate system
    grompp_mpi_d -f $nptfile -c $grofile -p $topfile -o $tprfile
    mpirun -np 8 mdrun_mpi_d -s $tprfile

    if [ -s traj.trr ]
    then

      # rename output files to contain the run temperature
      mv confout.gro $temp"_out.gro"
      mv ener.edr $temp"_ener.edr"
      mv traj.trr $temp"_traj.trr"
      mv mdout.mdp $temp"_mdout.mdp"
      mv md.log $temp"md.log"
      mv state.cpt $temp"state.cpt"

      # analyze the trajectory

      echo -e "1 2 3 4 5 6 7 8 9 10 11 12 13 14 15 16 17 0" | g_energy_mpi_d -f $temp"_ener.edr" -nmol
$nmol -b 2000
      mv energy.xvg $temp"_energy.xvg"
```

Figure F.1 Continued: Example .pbs File (page 2/3)

```
      GRO=$temp"_out.gro"
      TRAJ=$temp"_traj.trr"

      RDF1=$temp"_rdf1_CM_CM.xvg"
      RDF2=$temp"_rdf2_CC_CC.xvg"
      RDF3=$temp"_rdf3_CM_AM.xvg"
      RDF5=$temp"_rdf5_AM_AM.xvg"
      RDF7=$temp"_rdf7_CC_AM.xvg"
      RDF8=$temp"_rdf8_CC_CM.xvg"

      echo -e "4\n4\n" | g_rdf_mpi_d -f $TRAJ -s $GRO -n $ndxfile -o $RDF1 -b 3000
      echo -e "5\n5\n" | g_rdf_mpi_d -f $TRAJ -s $GRO -n $ndxfile -o $RDF2 -b 3000 -cut 0.3
      echo -e "4\n6\n" | g_rdf_mpi_d -f $TRAJ -s $GRO -n $ndxfile -o $RDF3 -b 3000
      echo -e "6\n6\n" | g_rdf_mpi_d -f $TRAJ -s $GRO -n $ndxfile -o $RDF5 -b 3000
      echo -e "5\n6\n" | g_rdf_mpi_d -f $TRAJ -s $GRO -n $ndxfile -o $RDF7 -b 3000 -cut 0.15
      echo -e "5\n4\n" | g_rdf_mpi_d -f $TRAJ -s $GRO -n $ndxfile -o $RDF8 -b 3000 -cut 0.15

      echo -e "4" | g_msd_mpi_d -f $TRAJ -s $tprfile -n $ndxfile -ten -o $temp'_CM_msd.xvg'
      echo -e "6" | g_msd_mpi_d -f $TRAJ -s $tprfile -n $ndxfile -ten -o $temp'_AM_msd.xvg'

      echo -e "4" | g_velacc_mpi_d -f $TRAJ -s $tprfile -n $ndxfile -o $temp"_"$diri"_CM_VACF.xvg" -b 2000
      echo -e "5" | g_velacc_mpi_d -f $TRAJ -s $tprfile -n $ndxfile -o $temp"_"$diri"_CC_VACF.xvg" -b 2000
      echo -e "6" | g_velacc_mpi_d -f $TRAJ -s $tprfile -n $ndxfile -o $temp"_"$diri"_AM_VACF.xvg" -b 2000

      echo -e "2" | g_rotacf_mpi_d -f $TRAJ -s $tprfile -n $ndxfile -o $temp"_"$diri"_CAT_RotACF1.xvg" -P
1 -d -b 2000
      echo -e "2" | g_rotacf_mpi_d -f $TRAJ -s $tprfile -n $ndxfile -o $temp"_"$diri"_CAT_RotACF2.xvg" -P
2 -d -b 2000
      echo -e "3" | g_rotacf_mpi_d -f $TRAJ -s $tprfile -n $ndxfile -o $temp"_"$diri"_ANI_RotACF1.xvg" -P
1 -d -b 2000
      echo -e "3" | g_rotacf_mpi_d -f $TRAJ -s $tprfile -n $ndxfile -o $temp"_"$diri"_ANI_RotACF2.xvg" -P
2 -d -b 2000

    fi

    grofile=$temp"_out.gro"
  fi

# change the temp (note that grofile is set to the final configuration of the run at the last
temperature, so it is used as the initial configuration at the new temperature.)

 ((temp+=50))
done



# *******
# tidy the run folder
# *******

rm -f step*
mkdir gro
mkdir rdf
mkdir energies
mkdir ACF
mkdir msd
mkdir runstuff
mv *_out.gro gro/.
mv *rdf*.xvg rdf/.
mv *ener.edr energies/.
mv *energy.xvg energies/.
mv *VACF* ACF/.
mv *RotACF* ACF/.
mv *_msd.xvg msd/.
mv *.log runstuff/.
mv *.cpt runstuff/.
mv *.mdp runstuff/.
mv *.tpr runstuff/.
mv *.ndx runstuff/.
```

Figure F.1 Continued: Example .pbs file (page 3/3)

```
2L100-16_1C
 2592
    1CAT     CM    1   0.090   0.017   5.606
    1CAT     CC    2  -0.070   0.008   5.603
    2CAT     CM    3   0.448   0.489   0.008
    2CAT     CC    4   0.608   0.490   0.007
    3CAT     CM    5   0.452   0.018   0.495
    3CAT     CC    6   0.612   0.017   0.493
    4CAT     CM    7   0.101   0.455   0.427
    4CAT     CC    8  -0.059   0.458   0.427
    5CAT     CM    9   0.111   0.014   0.917
    5CAT     CC   10  -0.049   0.019   0.916
    6CAT     CM   11   0.478   0.497   0.965
    6CAT     CC   12   0.638   0.498   0.961
    7CAT     CM   13   0.481   0.030   1.439
    7CAT     CC   14   0.641   0.028   1.436
    8CAT     CM   15   0.129   0.519   1.401
    8CAT     CC   16  -0.031   0.521   1.405
    9CAT     CM   17   0.128   0.070   1.879
    9CAT     CC   18  -0.032   0.071   1.879
   10CAT     CM   19   0.485   0.490   1.903
   10CAT     CC   20   0.645   0.489   1.906
   11CAT     CM   21   0.492   0.017   2.380
   11CAT     CC   22   0.652   0.012   2.380
   12CAT     CM   23   0.132   0.531   2.346
   12CAT     CC   24  -0.028   0.531   2.349
.
.
.
  860CAT     CM 1719   5.077   5.247   4.213
  860CAT     CC 1720   4.917   5.248   4.215
  861CAT     CM 1721   5.082   4.766   4.717
  861CAT     CC 1722   4.922   4.765   4.716
  862CAT     CM 1723   5.420   5.230   4.691
  862CAT     CC 1724   5.580   5.229   4.692
  863CAT     CM 1725   5.440   4.716   5.193
  863CAT     CC 1726   5.599   4.719   5.191
  864CAT     CM 1727   5.083   5.216   5.167
  864CAT     CC 1728   4.923   5.215   5.171
  865ANI     AM 1729   0.650   0.497   0.484
  866ANI     AM 1730   0.625   0.004   0.013
  867ANI     AM 1731   5.866   0.514   5.619
  868ANI     AM 1732   5.879   5.649   0.432
  869ANI     AM 1733   0.681   0.494   1.436
  870ANI     AM 1734   0.661   0.022   0.964
  871ANI     AM 1735   5.889   0.482   0.909
  872ANI     AM 1736   5.896   0.056   1.398
.
.
.
 1717ANI     AM 2581   5.642   5.259   3.261
 1718ANI     AM 2582   5.644   4.797   2.825
 1719ANI     AM 2583   4.909   5.251   2.784
 1720ANI     AM 2584   4.896   4.761   3.311
 1721ANI     AM 2585   5.615   5.224   4.214
 1722ANI     AM 2586   5.634   4.799   3.761
 1723ANI     AM 2587   4.897   5.259   3.731
 1724ANI     AM 2588   4.889   4.779   4.248
 1725ANI     AM 2589   5.618   5.190   5.161
 1726ANI     AM 2590   5.616   4.755   4.710
 1727ANI     AM 2591   4.885   5.234   4.690
 1728ANI     AM 2592   4.897   4.747   5.192
   5.96489   5.66679   5.65433
```

Figure F.2: Truncated Example of a .gro file. Many particles (Cations 13-859 and Anions 873-1716) have been omitted for brevity.

```
[ defaults ]
; nbfunc  comb-rule gen-pairs fudgeLJ fudgeQQ
1   2   yes   1.0  1.0

[ atomtypes ]

;name  atnum  mass    charge   ptype   sigma    epsilon
CM     11    115.000  0.000      A    0.500000  3.613285
CC      1      5.000  0.000      A    0.000000  0.000000
AM     21    120.000  0.000      A    0.500000  3.613285

[ nonbond_params ]
;i     j  func    sigma   epsilon
CM     CM   1   0.500000  3.613285
CM     AM   1   0.500000  3.613285
AM     AM   1   0.500000  3.613285
CM     CC   1   0.000000  0.000000
CC     CC   1   0.000000  0.000000
AM     CC   1   0.000000  0.000000


[ moleculetype ]
;molname  nrexcl
CAT   2

[ atoms ]
;id at type res nr  residu name at name cg nr charge
1       CM    1          CAT      CM   2      0.000000000000000
2       CC    1          CAT      CC   2      1.000000000000000

[ constraints ]
; ai   aj funct        b0
  1     2     2     0.16000

[ exclusions ]

1 2
2 1

[ moleculetype ]
; molname  nrexcl
ANI   2

[ atoms ]
; id  at type res nr  residu name at name cg nr charge
1       AM    1          ANI      AM   2 -1.000000

[system ]
2L100-16_050_1C_050

[ molecules ]
 CAT        984
 ANI        984
```

Figure F.3: Example .top file

```
; Run parameters
integrator  = md      ; leap-frog integrator
nsteps      = 4000000 ; 4.0 ns
dt          = 0.001   ; 1 fs
comm_mode   = linear  ; remove center of mass motion
nstcomm     = 10
comm_grps   = system

; Output control
nstxout   = 1000    ; save coordinates every ps
nstvout   = 1000    ; save velocities every ps
nstenergy = 1000    ; save energies every ps
nstlog    = 1000    ; update log file every ps

; Bond parameters
continuation  = no    ; first dynamics run
constraint_algorithm = lincs  ; holonomic constraints
constraints = all-bonds ; all bonds (even heavy atom-H bonds) constrained
lincs_iter  = 1   ; accuracy of LINCS
lincs_order = 6   ; also related to accuracy
lincs_warnangle = 90.0 ; much larger than normal.

; Neighborsearching
ns_type   = grid  ; search neighboring grid cells
nstlist   = 5     ; update list
rlist     = 1.7   ; short-range neighborlist cutoff (in nm)
rcoulomb  = 1.7   ; short-range electrostatic cutoff (in nm)
rvdw      = 1.7   ; short-range van der Waals cutoff (in nm)

; Electrostatics
coulombtype    = PME   ; Particle Mesh Ewald for long-range electrostatics
pme_order      = 4     ; interpolation
fourierspacing = 0.2   ; grid spacing for FFT

; Temperature coupling is on
tcoupl  = nose-hoover   ; thermostat type
tc-grps = CAT ANI       ; two coupling groups - more accurate
tau_t   = 0.1 0.1       ; time constant, in ps
ref_t   = 600 600       ; reference temperature, one for each group, in K

; Pressure coupling is on
pcoupl      = Parrinello-Rahman
pcoupltype  = isotropic
tau_p       = 5.0
compressibility = 3e-5
ref_p           = 1.0

; Periodic boundary conditions
pbc   = xyz   ; 3-D PBC

; Dispersion correction
DispCorr  = EnerPres  ; account for cut-off vdW scheme

; Velocity generation
gen_vel   = no  ; assign velocities from Maxwell distribution
gen_temp  = 0   ; temperature for Maxwell distribution
gen_seed  = -1  ; generate a random seed
```

Figure F.4: Example .mdp file